Spatially Resolved Spectroscopy
on Carbon Nanotubes

Spatially Resolved Spectroscopy
on Carbon Nanotubes

Proefschrift

ter verkrijging van de graad van doctor
aan de Technische Universiteit Delft,
op gezag van de Rector Magnificus prof.ir. K.F. Wakker,
voorzitter van het College voor Promoties,
in het openbaar te verdedigen op vrijdag 14 december 2001 om 13.30 uur

door

Jorg Wilfred JANSSEN

natuurkundig ingenieur,
geboren te Wageningen.

Dit proefschrift is goedgekeurd door de promotoren:
Prof.dr. C. Dekker
Prof.dr.ir. L.P. Kouwenhoven

Samenstelling van de promotiecommissie:

Rector Magnificus,	voorzitter
Prof.dr.ir. L.P. Kouwenhoven,	Technische Universiteit Delft, promotor
Prof.dr. C. Dekker,	Technische Universiteit Delft, promotor
Prof.dr.ir. J.E. Mooij,	Technische Universiteit Delft
Prof.dr. J.M. van Ruitenbeek,	Universiteit Leiden
Dr.ir. T.H. Oosterkamp,	Universiteit Leiden
Prof.dr. Ph. Lambin,	Facultes Universitaires
	de Notre-Dame de la Paix, Namen, België
Prof.dr. C. Schönenberger,	Universität Basel, Zwitserland

Printed in the Netherlands

Voor mijn ouders en Marjolein

Mountain Jan

We are proud of Jan
We are proud of Jan
We named a mountain after you
somewhere in Antartica
Unclimable, no different from the nameless others

He spent a number of years at this project
And now he knows how an electron behaves

Voorwoord

In Mesoscopolis, zoals de vakgroep Quantum Transport (QT) ook wel wordt genoemd, en in de vakgroep Moleculaire Biofysica (MB) is onderzoek geen eenmanszaak. Veel mensen hebben, al dan niet indirect, bijgedragen aan de totstandkoming van dit proefschrift. Allereerst waren er al diegenen die in mijn tijd deel uitmaakten van QT en MB: studenten, promovendi, post-docs en (technische) staf. Zij zorgden voor de aanspraak en ontspanning tijdens werk en koffie of borrel. Dit heeft mij altijd gemotiveerd en hiervoor wil ik iedereen, ook allen die ik niet bij name noem, hartelijk bedanken!

Een aantal mensen was direct betrokken bij het hier beschreven onderzoek. Ik wil mijn promotoren Leo Kouwenhoven en Cees Dekker bedanken voor hun begeleiding. Leo, ik heb veel van je geleerd op vele vlakken. Cees, je extra betrokkenheid in mijn laatste jaar heb ik zeer gewaardeerd. Hans Mooij wil ik bedanken voor de mogelijkheid om deel uit te maken van de door hem opgebouwde groep toegewijde wetenschappers.

Het grondwerk gebeurde bij de drie STM opstellingen samen met postdocs (Jeroen Wildöer, Leonid Gurevich, Martin Upward, Alberto Morpurgo en Serge Lemay), promovendi (Liesbeth Venema en Michael Janus) en afstudeerders (Mark Buitelaar, Dionne Klein, Maarten Mooij en Michiel van den Hout). Jeroen, bedankt voor het overdragen van je technische kennis en je blijvende interesse. Leonid, 'in principle' had je voor alles een oplossing, wat me keer op keer verbaasde. Martin, thanks for the good times at the dilution fridge and for teaching me some English. Alberto, je ideeën en opinies zijn van grote waarde voor me geweest, nice and solid to you too. Serge, I learned a lot from your extremely thorough way of working. I really enjoyed the time we spent measuring and discussing, in the broad sense, together. Many thanks too for your critics on my writing. Michael, liedjes zullen nooit meer zo goed lopen als destijds, laat staan dat er nog eens een nanoscience dag wordt georganiseerd op de eerste zondag in april. Liesbeth en Mark, ik heb me met jullie goed vermaakt op de vrijdagavonden die we vrijhielden voor een mogelijk perfecte meting, ook als deze niet plaatsvond. Dionne, je onderzoek deed veel stof opwaaien. Ik kijk met

plezier terug op onze samenwerking en je enthousiasme en gezelligheid. Maarten en Michiel, met onze 'positive mindset' wisten we kabouter Prikkeprak kort te houden. Maarten, bedankt voor je nauwgezette manier van werken. Michiel, dankjewel voor je initiatief en je onnavolgbare humor.

Verder wil ik Kees Harmans, Herre van der Zant en Peter Hadley bedanken voor de gevoerde discussies en hun bijdrage aan de goede sfeer in de groep. De technische ondersteuning, en gezelligheid, van Bram van der Enden, Mascha van Oossanen, Leo Lander, Leo Dam en Raymond Schouten waren van grote waarde.

Ook de rebelse tijd wil ik hier niet onvermeld laten. Samen met Henk Postma en Wilfred van der Wiel slaagden we er dan toch in financiële gerechtigheid voor alle OiO's aan de TU Delft te krijgen. Laatstgenoemde was tevens kamergenoot in F027, waar ook Liesbeth, Alexander ter Haar en Adrian Lupascu voor een goede uitvalsbasis zorgden. Als laatste wil ik nog mede-promovendi Pieter Heij, Caspar van der Wal, Hannes Majer en Ronald Hanson bedanken voor de goede tijd.

Daarnaast waren er al diegenen die buiten QT en MB voor mijn ontspanning en motivatie hebben gezorgd. De afleiding die mij geboden werd door besturen, roeiers en medecoaches op de D.S.R. Proteus-Eretes en op trainingskampen en wedstrijden, heeft indirect veel bijgedragen aan dit proefschrift.

Tijdens mijn verdediging word ik ter zijde gestaan door Bert van Helvoirt en Annette van den Berg. Hen, maar ook mijn andere vrienden, wil ik nadrukkelijk bedanken voor de interesse in en het meeleven met mijn onderzoek in de afgelopen vier jaar.

Rest mij als laatste hen te bedanken die mij het naast staan. De interesse en het luisterend oor van zowel mijn ouders als 'schoon'ouders betekenen veel voor mij. Pa en Ria, jullie vertrouwen is voor mij een grote stimulans. Bedankt voor jullie relativerende kijk en het zijn van een goede thuishaven. Marjolein, dankjewel voor de hulp bij het vullen van de koelkasten; die oranje ballonnen kon ik niet alleen aan! Krista, bedankt voor je oeverloze commentaar maar vooral voor je vrolijkheid, je liefde en je steun.

<div style="text-align: right">

Jorg Janssen
's Gravenhage, 18 oktober 2001

</div>

Contents

Chapter 1

Introduction

1.1 Nanotechnology

Nowadays chip technology is based on defining structures in silicon, down to line-widths of 100 nm, using optical lithography. These structures make up components, like transistors, and the wires connecting them. Technically it should be possible to go down to widths of 50 nm with these optical methods, although this requires costly lenses to focus extreme UV light, needed because of the small wavelengths of 100 to 200 nm. With state of the art electron beam pattern generators, were electrons are used instead of light, length scales down to 10 nm are in reach but not (yet) on a commercial basis.

Defining structures at such small length scales is not only a technical challenge but also the physics can change fundamentally. At 1 to 10 nm, 10 to 100 times the size of an atom, quantum mechanics will start to play a dominant role. Electrons can no longer be treated as particles but have to be treated as waves. This leads to new, sometimes unexpected, physics. This interplay between classical and quantum physics, is called mesoscopic physics. Mesoscopic physics has made important contributions to the broader nanotechnology field.

Nanotechnology is the collective name for research efforts on nanometer sized system in physics, chemistry and biology. One of the main goals is to build electronics on a nanometer length scale, the next step after microtechnology. In particular scanning probe techniques, with their ability to probe effects on a 1 to 100 nm length scale, contribute a lot to our understanding in this fast developing field.

1.2   Scanning tunneling microscopy

With the invention of the scanning tunneling microscope (STM) in 1982, by later
Nobel prize winners Binnig and Rohrer, a completely new way of exploring very
small objects was found [1, 2]. This invention is often regarded as the starting
point for nanotechnology. By scanning a sharp needle over a conducting surface
while watching changes in the current, unprecedented spatial resolution could be
obtained. For the first time, the smallest particles of which matter is build up,
called atoms already by the Greek, could be made directly visible. The Si(111)
was the first surface on which atomic resolution was obtained, see Fig. 1.1.
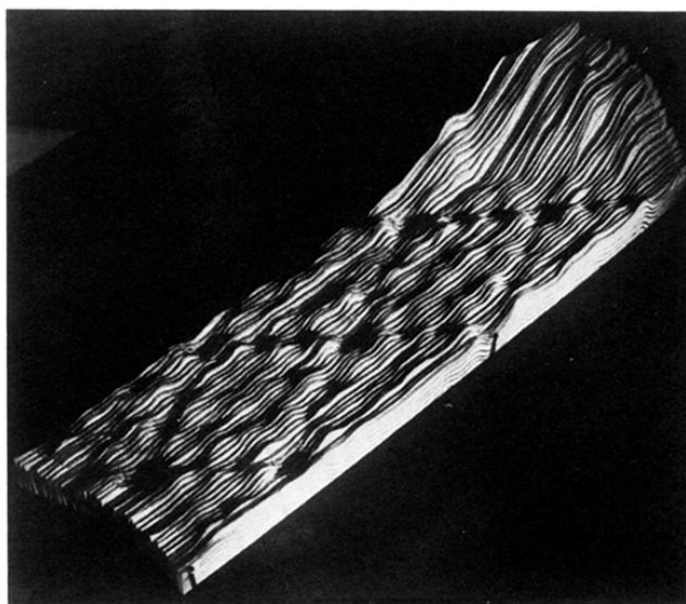
Figure 1.1: First real space image of atoms on a surface. Two 7x7 unit cells of the
Si(111) surface. Taken from Ref. [2].

The very high spatial resolution, combined with the possibility to study the
electronic structure locally, makes the STM such a powerful tool. Since 1982 the
scanning probe field has grown enormously. Based on the principles of STM,
an atomic force microscope was built [3]. More recently, other scanning probes
were developed like a scanning hall probe microscope, a scanning capacitance
microscope and a scanning electrochemical microscope [4]. All these scanning
probes have the ability to study the specific physical process position dependent
on a very small length scale. The STM, in particular, has contributed a lot to
get a better understanding of, for example, superconductivity and dopants in
semiconductors. In chapter 2 we give a few examples of recent results obtained
with STMs operated at low temperatures.

1.3 Fullerenes and nanowires

Besides studying surfaces, the STM also opened the possibility to study structures and objects with sizes down to 1 nm or less, such as molecules. Already in the 70's it was proposed that molecules could be used as future electronic devices [5]. The self assembling properties of specific molecules gave the promising perspective of nanoscale devices which were faster to make than by using time consuming lithography processes. The biggest challenge however was to find a conducting molecule, suitable to use as a nanowire and/or possible to turn into a device.

Carbon nanotubes, long cylindrical molecules made from carbon atoms, turned out to be such molecules. They belong to the same class of molecules as C_{60}, discovered in 1985 [6]. The discoverers, Kroto, Heath, Smalley and Curl, had to come up with a structure after detecting a peak in their mass spectrometer at 60*12 atomic mass units. They were inspired by the geodesic domes of architect Buckminster Fuller, like the one in Fig. 1.2. A spherical structure with the carbon atoms forming the corner points of 12 pentagons and 20 hexagons was stable and in agreement with the measurements on C_{60}. This structure is plotted in Fig. 1.2 on the right. Now the popular name for C_{60} is bucky ball and materials like C_{60} are called fullerenes, after the architect. For their discovery Kroto, Smalley and Curl received the Nobel prize for chemistry in 1997.
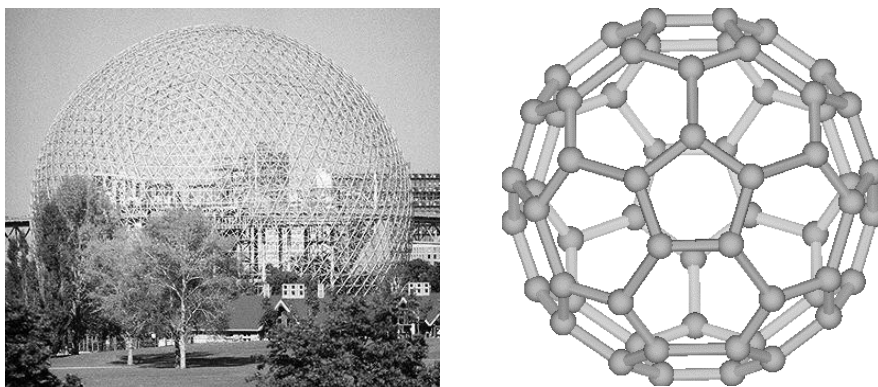
Figure 1.2: Dome structure by architect Buckminster Fuller, Montreal, Canada. On the right a ball and stick model of a C_{60} molecule.

Based on the hollow C_{60} molecule, theorists speculated on a wire-like molecule made up of carbon atoms. Hexagons could form a hollow cylinder as if a sheet of graphene is rolled up and closed at the ends by two halves of a bucky ball. In 1991 Iijama found these fullerene nanotubes in the analysis of transmission electron microscopy (TEM) images of the carbon soot, which is the result of fullerene growth [7]. In Fig. 1.3 such a TEM image is shown, next to a ball and

stick model of a possible structure of a carbon nanotube. They have a typical diameter of 1 to 10 nm and can be micrometers in length.
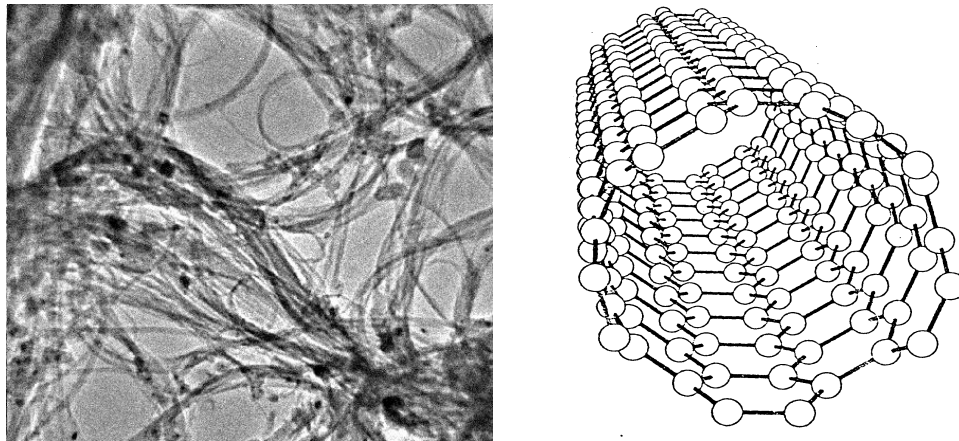
Figure 1.3: TEM image of raw soot of carbon nanotube material [8]. On the right, one of the possible structures of a carbon nanotube, in this case the armchair structure.

Compared to their weight, nanotubes are the strongest material known. Their Young modulus is 5 times that of steel [9]. A number of applications for constructions, such as fibers, have been proposed, but not yet realized. Here, we focus on the remarkable electronic properties. Directly after carbon nanotubes were discovered, theorists predicted that carbon nanotubes could be metallic since graphite is metallic [10].

Indeed, depending on the exact arrangement of carbon atoms in a tube, they show either metallic or semiconducting behaviour. In 1997 transport measurements showed that nanotubes can be good conductors and regarded as molecular wires [11]. Soon after, STM studies revealed that the two classes of tubes, semiconducting and metallic, exist [12]. Since then a number of electronic building blocks have been realized [13].

Recently, the first logic building blocks were built from single molecules [14]. An inverter, static random access memory and a ring oscillator were realized by connecting transistors made from a single carbon nanotube, which each had a gain of more than 1.

Not only with the prospect of molecular electronics in mind nanotubes are of interest, they also serve as a model system to study more fundamental physics. Carbon nanotubes are true one dimensional conductors, something which leads to new interesting physics, eg. the observation of Luttinger liquid behavior [15]. In the last two chapters of this thesis we show how we can use nanotubes as a model system for the well known 'particle in a box' problem.

1.4   Thesis outline

This thesis describes a number of experiments performed with low temperature scanning tunneling microscopes. In chapter 2 the physical mechanism and technical aspects of STM are explained. The design and testing of a milli Kelvin STM, on the superconductor $NbSe_2$, is discussed in chapter 3. The electronic properties of carbon nanotubes are described in chapter 4 followed by chapter 5, in which the first STM observations on these molecules are reviewed. More specific studies on carbon nanotube buckles and crossed carbon nanotubes are presented in chapters 6 and 7. The observation of a suppression in the differential conductance at zero bias on carbon nanotubes is the subject of chapter 8 and possible explanations for this suppression are discussed. Chapters 9 and 10 provide a nice illustration of using carbon nanotubes as a model system to study fundamental physics. The textbook problem of a 'particle in a box' is experimentally realized and the shape of the wave functions is measured.

References

[1] G. Binnig, H. Rohrer, Ch. Gerber and E. Weibel, Phys. Rev. Lett. **49**, 57 (1982).

[2] G. Binnig, H. Rohrer, Ch. Gerber and E. Weibel, Phys. Rev. Lett. **50**, 120 (1983).

[3] G. Binnig, C.F. Quate and Ch. Gerber, Phys. Rev. Lett. **56**, 930 (1986).

[4] R. Wiesendanger, *Scanning Probe Microscopy and Spectroscopy* (Cambridge University Press, 1994).

[5] C. Joachim, J.K. Gimzewski and A. Aviram, Nature **408**, 541 (2000), and references therein.

[6] H.W. Kroto, J.R. Heath, S.C. O'Brien, R.F. Curl and R.E. Smalley, Nature **318**, 162 (1985).

[7] S. Iijima, Nature **354**, 56 (1991).

[8] Taken from Richard Smalley's image gallery at *http://cnst.rice.edu/pics.html*.

[9] A. Krishnan, E. Dujardin, T.W. Ebbesen, P.N. Yianilos and M.M.J. Treacy, Phys. Rev. B **58**, 14013 (1998).

[10] J.W. Mintmire, B.I. Dunlap and C.T. White, Phys. Rev. Lett. **68**, 631 (1992).

[11] M. Bockrath, D.H. Cobden, P.L. McEuen, N.G. Chopra, A. Zettl, A. Thess and R.E. Smalley, Science **275**, 1922 (1997); S.J. Tans, M.H. Devoret, H. Dai, A. Thess, R.E. Smalley, L.J. Geerligs and C. Dekker, Nature **386**, 474 (1997).

[12] J.W.G. Wildoer, L.C. Venema, A.G. Rinzler, R.E. Smalley and C. Dekker, Nature **391**, 59 (1998); T. Odom, J.-L. Huang, P. Kim and C.M. Lieber, Nature **391**, 62 (1998).

[13] For a review see C. Dekker, Physics Today **52**, 22 (1999).

[14] V. Derycke, R. Martel, J. Appenzeller and Ph. Avouris, Nano Letters **1**, 453 (2001), published online 26 August 2001; A. Bachtold, P. Hadley, T. Nakanishi and C. Dekker, Science, 4 October 2001 (10.1126/science.1065824).

[15] J.M. Luttinger, Journal of Math. Physics **4**, 1154 (1963); M. Bockrath, D.H. Cobden, A.G. Rinzler, R.E. Smalley, L. Balents and P.L. McEuen, Nature **397**, 598 (1999).

Chapter 2

Scanning tunneling microscopy

In this second chapter we discuss the physics behind the operation of the scanning tunneling microscope (STM). After explaining the topography and spectroscopy modes of the STM, we focus on some of the technical difficulties associated with STM at low temperatures. Finally we present a few relevant experiments demonstrating the possibilities and strengths of STM.

2.1 Physical mechanism

One of the most intriguing aspects of quantum mechanics is the possibility for electrons to tunnel through an insulating barrier which is forbidden in classical physics. Tunneling stems directly from the fact that in quantum mechanics electrons are no longer treated as particles but as waves, described by a wave function. At the barrier between a metal and an insulator the wave function does not drop to zero instantly but 'leaks' into the insulator, such that there is a finite probability to find an electron inside the barrier. When two metals are brought close together, typically 1-2 nm, such that the tails of the wave function of electrons in either metal have a finite overlap (Fig. 2.1), an electron can tunnel through the barrier and a tunnel current can flow. The magnitude of this current is exponentially dependent on the distance between the two metals.

In an STM a sharp metallic tip is brought close to a flat conducting substrate and a voltage difference is applied between the two. At a typical distance of 1 nm a tunnel current can flow between tip and substrate. The exponential dependence of the current on the distance is what makes the STM so extremely sensitive.

Using Fermi's golden rule [1] we can calculate the tunnel current. With ρ_t the density of states (DOS) in the tip and ρ_s the density of states of the substrate
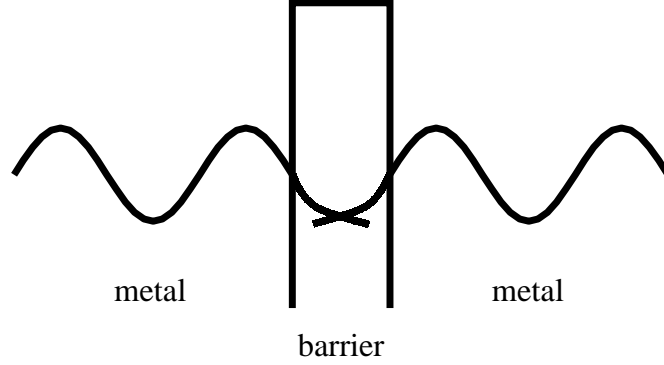
Figure 2.1: Two metals separated by a small insulating barrier. The electron wave functions of the metals decay into the barrier. The overlap of the two tails enables electrons to cross the barrier.

the tunnel current I at a voltage difference V is given by:

$$I(V) = \frac{4\pi e}{\hbar} \int\limits_{-\infty}^{\infty} \left[f(E_F - eV + \varepsilon) - f(E_F + \varepsilon) \right] \times \rho_s(E_F - eV + \varepsilon) \rho_t(E_F + \varepsilon) \left| M \right|^2 d\varepsilon$$

(2.1)

Here ε is the energy difference with respect to the Fermi energy E_F. For temperatures (much) lower than the preferred energy resolution δ ($3.5 k_B T < \delta$) the Fermi functions f can be approximated by step functions. The influence of temperature on the energy resolution is discussed later in this chapter.

The matrix element M, which describes the coupling between wave functions in tip and sample, Ψ_{tip} and Ψ_{sample}, can be written as $M \propto e^{-2\kappa W}$. W is the width of the barrier and κ is the decay constant. In a first approximation we treat κ as energy independent [2], this makes M independent of energy. An ideal tip has a featureless constant DOS (ρ_t) in the energy range of interest and then Eq. 2.1 reduces to:

$$I(V) \propto e^{-2\kappa W} \int\limits_{0}^{eV} \rho_s(E_F - eV + \varepsilon) d\varepsilon$$

(2.2)

In Eq. 2.2 we see the exponential dependence of the current on the distance between tip and sample. This exponential dependence makes the STM very sensitive to changes in either the substrate surface height or electronic properties. It is this sensitivity that makes the STM such a powerful tool and which is crucial in all the measurements that will be discussed in this thesis. A more detailed discussion on tunneling used in STM is found in Ref. [3].

2.1.1 Topography

In Fig. 2.2 we have schematically drawn the operation of the STM. The tip is kept at a distance W, the barrier width, above the surface by a piezo electric which moves the tip in the x, y and z direction. The feedback loop continually monitors the tunnel current and compares it with the set feedback current. Upon variations in the tunnel current the voltage on the piezo, which regulates the height z, is adjusted. The adjustments of the z-piezo voltage are recorded as a function of position to create topographic images.
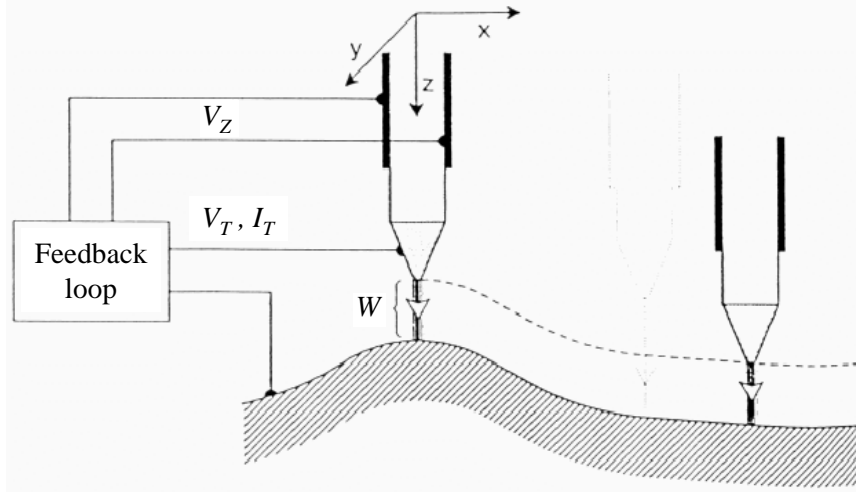
Figure 2.2: Operation principle of an STM. The tip is kept at a distance s above the surface by a piezo electric which moves the tip in the x, y and z direction. The feedback loop continually monitors the tunnel current and compares it with the set feedback current. Variations in the tunnel current are compensated by changing the voltage on the piezo which regulates the z. Taken from Ref. [3].

This operation mode is known as the constant current mode. Because the feedback loop is active, the height of the sharp tip will be adjusted for the corrugation of the surface. Another mode which is far less often used is the constant height mode. Here the current is monitored while the tip is scanned over the surface with a constant voltage on the z-piezo. A higher current corresponds to a rise in the surface and vice-versa. Obstacles which are higher than the distance between the surface and the tip, however, can not be avoided. The tip will hit such an obstacle and there is a high risk that the sharpness of the tip is affected. Most of the time this mode is not used for exploring surfaces. For atomic resolution in a small area this mode is sometimes useful. With the feedback turned off the tip can be scanned much faster over the area and the change in current then shows the atoms.

2.1.2   Spectroscopy

The tunnel current between tip and sample also allows for local, position dependent, (scanning tunneling) spectroscopy (STS) on a surface or on small objects on that surface. At a point of interest on the surface the feedback is turned off and by sweeping the voltage and measuring the current an $I-V$ curve is obtained. When this $I-V$ curve is numerically differentiated we obtain, using Eq. 2.2:

$$\frac{\partial I}{\partial V}(V) \propto \rho_s(E_F - eV + \varepsilon) \tag{2.3}$$

This $dI/dV(V)$ curve is a measure of the DOS in the sample, assuming an ideal tip with a flat DOS and an energy independent barrier (reflected in the assumption that M is independent of energy). If the tip DOS is not flat the $dI/dV(V)$ curve will be a convolution of the DOS in tip and sample. We therefore always check our tip at a spot on the surface where we know the $I-V$ should be linear. If this is the case we can expect the tip to have a constant DOS.

For large voltages (> 1 V) between tip and sample the barrier becomes effectively lower, causing the current to grow exponentially. In this case features at higher voltages are obscured by the increasing current. To enhance these features, dI/dV can be normalized by division with I/V, and it has been argued that this is a better measure for the DOS [4, 5]. Normalisation corrects for the shape of the barrier but assumes that M is independent of energy, which is usually not the case at higher energies. This method is therefore controversial. We will show the difference between normalized and direct spectroscopy curves in chapter 5.

A number of experiments described in this thesis combine topography and spectroscopy. With spectroscopy curves measured at equidistant positions along a line, good insight is obtained in the spatial dependence of spectroscopy data, $dI/dV(x, V)$. For example, linescans are used to study the change in spectroscopy along the length axis of carbon nanotubes. Another method is taking spectroscopy curves on a grid of points on a topography map. By taking slices out of the three dimensional $dI/dV(x, y, V)$ dataset, maps of the LDOS at specific energies are obtained. This technique allowed us to get to the results presented in chapters 3 and 10.

We can also describe the LDOS as a summation of discrete electronic wave functions, this can be useful for describing very small systems or interfering waves at step edges. Then the STS curves correspond to:

$$\frac{dI}{dV}(V, r) \propto \sum_{|eV - \varepsilon_j| < \delta} |\psi_j(r)|^2 \tag{2.4}$$

where δ is the experimental energy resolution. In the limit where δ is less than the energy level spacing $\varepsilon_{j+1} - \varepsilon_j$ the summation in Eq. 2.4 reduces to a single

term. Then a slice out of the three dimensional $dI/dV(x, y, V)$ dataset for fixed V corresponds to a spatial map of the individual wave function $|\psi_j|^2$. Chapters 9 and 10 show such measurements.

For good spectroscopy the mechanical stability of the STM has to be such that the tip-sample distance W stays constant while the voltage is swept. One order of magnitude change in the current is already caused by 0.1 nm change in W. With a typical value for W of less then 1 nm a stability of 10 pm is needed in order to have less then 1% noise in the current, and thus in $dI/dV(V)$. The technical aspects of realizing this mechanical stability are discussed in section 2.2.

In order to study mesoscopic phenomena using STS, an energy resolution of typically 1 meV (or better) is preferable. The energy resolution is limited by the thermal energy $3.5k_BT$. At liquid Helium temperatures, 4.2 Kelvin, the thermal broadening is of order 1 meV. Most experiments described in this thesis were performed with an STM cooled down to ~ 4.5 Kelvin. To study superconductors we need to get to temperatures (much) lower than their critical temperatures. With an STM attached to a dilution fridge we can reach temperatures down to 70 mK, corresponding to a energy resolution of ~ 25 μeV. In the next chapter the development of such an STM is discussed in detail and experiments demonstrating its capabilities are shown.

Temperature is not the only limiting factor for the energy resolution. Noise in the measurement apparatus often raises the effective temperature. Broadening of features is also possible by hybridization of wave functions of the surface with wave functions in the object of study [6]. This sets an intrinsic width of resonances, on our nanotubes on gold we find a typical broadening of 5 to 10 meV.

2.2 Technical aspects

Instead of differentiating an I/V curve, dI/dV can also be measured directly using a lock-in amplifier. While sweeping the voltage, the lock-in applies a small oscillating voltage δV (typically $\delta V_{peak-peak} = 5$ mV) on top of the gap voltage V with a frequency ω (order 1 kHz). Measuring the current change δI at this specific frequency directly yields a $dI/dV(V)$ curve. This method has the advantage that noise at other frequencies than ω is not measured, although it can still have an influence on for example the effective temperature. The frequency ω has to be higher than the response frequency of the feedback loop, otherwise the feedback loop tries to adjust for the oscillation voltage before turning of the feedback for

the start of the curve.

The distance W between tip and sample is typically 5 to 7 Å for a practical tunnel current of 10 to 100 pA. It is far from trivial to bring the tip with this precision to the surface, especially at temperatures of 4 Kelvin and lower. After aligning the tip above the sample under an optical microscope the tip-sample distance is typically less than 1 mm. The coarse movement, in our STMs based on slip-stick motion, moves the tip in small steps towards the surface until a tunnel current is detected. In Fig. 2.3 the principle of slip-stick motion is explained.
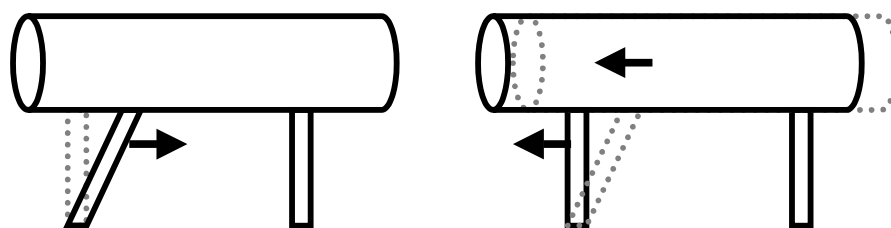
Figure 2.3: Slip-stick motion. A cylinder is supported by two springs. Moving one spring quickly to the right and slowly to the left moves the cylinder to the left.

The cylinder lies on two springs. The left spring is moved quickly to the right and slides under the cylinder. When it comes back slowly, the cylinder sticks to the spring and moves a small step to the left. The fast movement is in our case done by a piezo electric upon applying a voltage signal with a special waveform and moves the cylinder $\sim$100 nm per step. At low temperatures slip-stick motion is not 100% reliable. Parts can freeze together and the expansion of the piezo, for the same applied voltage, is less than at room temperature due to a smaller expansion coefficient [7], requiring higher voltages to get a similar stepsize.

Inside the cylinder another piezo electric moves the tip in x, y and z above the surface with sub-ångstrom precision. A typical scan size at room temperature is $4 \times 4 \ \mu m^2$ and $1 \times 1 \ \mu m^2$ at 4 Kelvin. The scan size is limited by the voltage that can be applied on the piezo. Typical voltages range up to 200 Volts. Using higher voltages can depolarize the piezo material and thus affect the calibration, which relates the applied voltage to the actual displacement. At 4 Kelvin the expansion coefficient is $\sim$4 times lower than at room temperature, therefore the scan sized is reduced.

Due to differences in thermal contraction of the different materials used for building the STM the sharp tip can crash into the sample surface. In order to minimize this risk materials that have similar expansion coefficients are used and all components and design are as much as possible cylindrically symmetric. For

high mechanical stability the tip-holder - sample-holder loop has to be as small as possible. This gives the highest resonance frequency and makes the STM less sensitive to vibrations. Coupling of vibrations of the building, with amplitudes of up to 100 nm at frequencies of 1 to 100 Hz. [8], into the STM is minimized by suspending the whole cryostate on the ceiling by bungy-cords or by installing the STM on a vibration isolation table with airleg suspension [9].

A usable tunnel current can only flow if the insulating barrier is not larger than 1 nm. Dirt (e.g. organic) on the sample surface can form larger barriers locally. In order to keep our samples as clean as possible all our measurements are performed in vacuum. As soon as the tip is positioned above the surface the STM is pumped out to a vacuum of 10^{-3} mbar or lower. Cooling down to 4 Kelvin results in condensation of any rest gasses on the walls of the vacuum chamber resulting in pressures of 10^{-9} mbar or lower.

The full design of our dilution fridge STM will be presented in the next chapter. A home built STM based on the so-called 'Nijmegen design' is used. A thorough description of this STM can be found in the Ph.D. thesis by Jeroen Wildöer [10]. Further measurements described in chapter 5, 7 and 9 are done with a home built system based on the 'Nijmegen design' but connected to a 4.2 Kelvin dipstick. This has the advantage of faster cooling down procedures and still excellent mechanical stability.

The measurements in chapters 6 and 10 are done in a commercially bought Omicron Low Temperature STM which usually is operated at 4.6 Kelvin [11]. Chapter 8 is based on measurements done in both STMs. The advantage of the Omicron system is that a number of samples and tips can be put into the vacuum chamber. Tip and/or sample can be changed with the system at low temperatures, yielding a cleaner environment. This STM also has a x-y-table allowing coarse movement in this plane. If an area of 1×1 μm^2 has been searched the tip can be moved towards a new spot. Without this coarse movements the tip would have to be positioned on a new spot on the sample manually, requiring warming up and venting the vacuum chamber. More on the design and operation of this STM can be found on the Omicron website [11].

2.3 Recent STM results at low temperatures

To illustrate the context of this thesis three recent results will be given that clearly demonstrate the combination of the high spatial and energy resolution of an STM.

Already in the late 80's the group of Hess mounted an STM on a dilution

fridge [12]. The technical difficulties of moving the tip close to the surface at low temperatures, compensating for thermal expansion and the time consuming cooling down procedures were the reason that only in recent years a number of other groups started to develop STMs capable of working at temperatures of 4 K and lower.

First, Eigler and co-workers showed that it was possible to move atoms on a surface, resulting in the famous IBM logo written with Xenon atoms [13]. This technique was used to built so called quantum corrals. In these confined structures the wave nature of electrons is made visible as can be seen in Fig. 2.4, where an ellipsoid mirror is built with Cobalt (Co) atoms on a Copper surface. In one focus of the ellipsoid a Co atom is placed. Due to the magnetic moment of Co a Kondo resonance is present caused by screening of this magnetic moment by surrounding electrons [14]. At the other (empty) focus a similar but attenuated resonance was found [15]. Analogous to the acoustics of an ellipsoid room, where you whisper in one focus and are heard in the other focus, this experiment nicely demonstrates the wave nature of electrons.
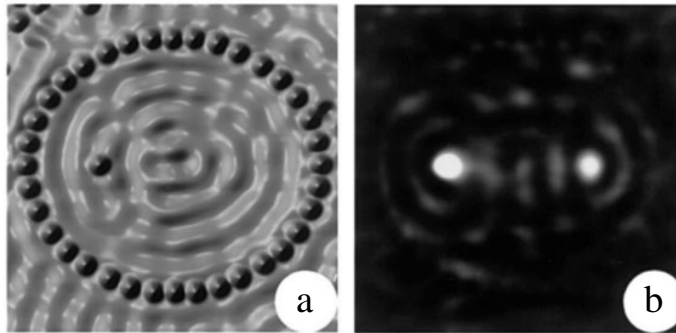
Figure 2.4: a) Topography image of an ellipse made of Co atoms on a Cu surface with a Co atom in the left focus. b) The Kondo resonance induced by the single Co atom is visible in the dI/dV map at the left focal point. In the right focal point its 'mirage' is seen although there is no Co atom present there. Reproduced from Ref. [15].

A second example is the study of superconductors. Hess used his dilution fridge STM to study the electronic states in a superconductor and was able to image the vortices in $NbSe_2$ [12]. Recently Pan *et al.* measured the effect of a Zn atom replacing a Cu atom in the CuO_2 plane (Fig. 2.5a) of a high temperature superconductor (BSCCO) [16]. The Zn atom locally interferes with the mechanism for superconductivity in the CuO_2 plane, creating an impurity state. The superconducting energy gap is anisotropic and it becomes zero along the diagonals of the square CuO_2 lattice (Fig. 2.5b). Along these diagonals the impurity state can most easily 'leak out'. The cross shaped interference pattern
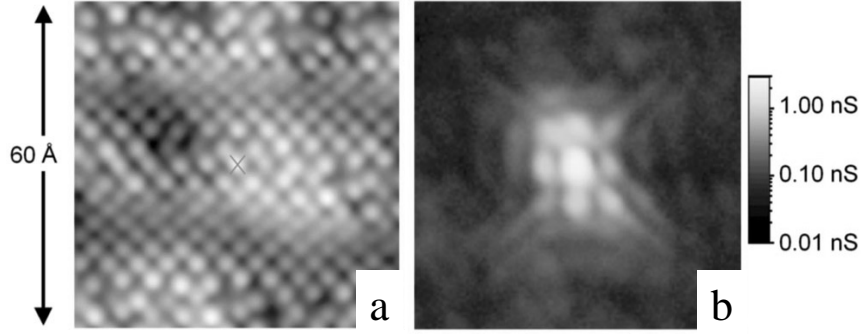
Figure 2.5: a) 60 × 60 Å image of Bi atoms on the surface of the BSCCO high T_c superconductor, whose positions relates to the position of Cu atoms in the CuO_2 plane. At the × the Zn impurity atom is present. b) Simultaneously acquired image of the conductance or DOS around the Zn impurity atom showing the cross shaped interference pattern. Reproduced from Ref. [16].

formed by the impurity state serves for a better understanding of the mechanism of high T_c superconductivity, which is not yet fully understood.
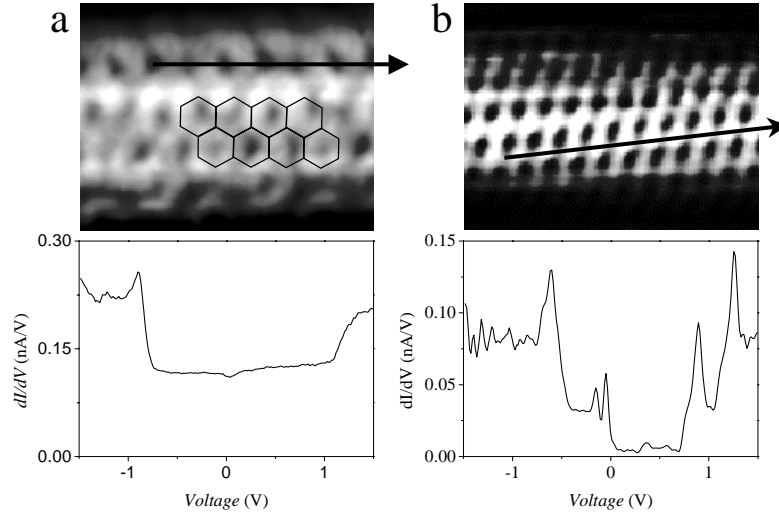
Figure 2.6: Atomic structure of two carbon nanotubes and their DOS. a) An armchair tube showing metallic behaviour. b) A chiral tube showing semiconducting behaviour.

The third example reveals the link between the atomic structure of carbon nanotubes and their electronic properties. These long cylindrical molecules are deposited on a gold substrate and imaged down to the atomic scale by STM. The electronic properties of these molecules depend on the angle with which the atoms spiral along the tube axis. In Fig. 2.6a the atoms lie in rows parallel to

the tube axis. These kind of tubes show metallic behavior, as can be seen in the lower panel. In Fig. 2.6b the atomic rows lie under a small angle with the tube axis and in this case the tube behaves like a semiconductor, the small 0.6 V semiconducting gap is clearly visible in the spectroscopy. This was the first experiment that demonstrated the relation between the atomic structure and the electronic properties of carbon nanotubes [17, 18]. It is the strength of STM to combine topography with local spectroscopy which is essential in this experiment. In chapter 5 these first experiments are discussed in detail.

Since the invention of the STM in 1982 the field has grown enormously. Numerous other examples can be given illustrating the strength of STM. These measurements, including the ones discussed in this thesis, are challenging. Very high mechanical stability is required. For example, in the results presented in the next chapter spectroscopy curves of 20 minutes each make up the figures. During this time the feedback is off and the tip-sample distance should stay constant to within tenths of an ångstrom. Measurements presented in chapter 10 are typically the result of overnight measurement runs and require negligible drift in the x-y-plane.

References

[1] L.I. Schiff, *Quantum Mechanics* (McGraw-Hill, New York, 1968).

[2] C.J. Chen, *Introduction to Scanning Tunneling Microscopy* (Oxford University Press, 1993).

[3] R. Wiesendanger, *Scanning Probe Microscopy and Spectroscopy* (Cambridge University Press, 1994).

[4] J.A. Stroscio, R.M. Feenstra and A.P. Fein, Phys. Rev. Lett. **57**, 2579 (1986).

[5] N.B. Lang, Phys. Rev. B **34**, 5947 (1986).

[6] J.W. Gadzuk, Phys. Rev. B **1**, 2110 (1970).

[7] PZT5H piezoelectric tubes supplied by Morgan Matroc Inc.

[8] M. Okano, K. Kajimura, S. Wakiyama, F. Sakai, W. Mizutani and M. Ono, Journal of Vac. Science & Techn. A **5**, 3313 (1987).

[9] Vibration isolation table with airleg supsension supplied by Melles Griot Inc., also available from Newport Inc.

[10] J.W.G. Wildöer, Ph.D. thesis KU Nijmegen and TU Delft (1997) and J.W.G. Wildöer, A.J.A. van Roij, H. van Kempen and C.J.P.M. Harmans, Rev. Sci. Instrum. **65**, 2849 (1994).

[11] Low Temperature STM, Omicron Vakuumphysik Gmbh, Taunusstein, Germany, *http://www.omicron.de.*

[12] H.F. Hess, R. B. Robinson and J.V. Waszczak, Phys. Rev. Lett. **64**, 2711 (1990).

[13] D.M. Eigler and E.K. Schweizer, Nature **344**, 524 (1990).

[14] V. Madhavan, W. Chen, T. Jamneala, M.F. Crommie and N.S. Wingreen, Science **280** 567-569 (1998).

[15] H.C. Manoharan, C.P. Lutz and D.M. Eigler, Nature **403**, 512 (2000).

[16] S.H. Pan, E.W. Hudson, K.M. Lang, H. Eisaki, S. Uchida and J.C. Davis, Nature **403**, 746 (2000).

[17] J.W.G. Wildöer, L.C. Venema, A. Rinzler, R.E. Smalley and C. Dekker, Nature **391**, 59 (1998).

[18] T. Odom, J.-L. Huang, P. Kim and C.M. Lieber, Nature **391**, 62 (1998).

Chapter 3

An ultra-low temperature scanning tunneling microscope

M.D. Upward, J.W. Janssen,
L. Gurevich, A.F. Morpurgo and L.P. Kouwenhoven

We have developed a home built ultra-low temperature scanning tunneling microscope (STM) capable of continuous operation down to 70 mK, and in a magnetic field of up to 12 T. Extensive testing has shown that the STM is capable of very stable operation, including atomic resolution and spectroscopy with a high energy resolution. To test the microscope we have investigated the structural and electronic properties of the type-II superconductor $NbSe_2$.

3.1 Introduction

The STM, since its development in 1982 [1, 2], has been adapted for operation in a wide variety of conditions, for instance ultra-high vacuum, high temperatures and very low temperatures. Microscopes that operate at very low temperatures, particularly in the millikelvin regime, have been the subject of a great deal of recent interest. Such instruments enable phenomena that have critical temperatures below 1 K to be investigated with the inherently high spatial resolution of STM. Operation at these temperatures can also provide high energy resolution, which ideally is just limited by thermal broadening. STM is also unique in its ability to measure the spatial variation of the local density of states (LDOS) with atomic resolution. To date, there have been relatively few reports of STMs capable of operating at temperatures below 1 K [3, 4, 5] and even fewer capable of less than 100 mK [6, 7]. This is primarily due to the technical difficulties associated with combining the two techniques. In this paper we present the design and

testing of an STM attached to a dilution refrigerator that is capable of operating at 70 mK. The system is also equipped with a 12 T superconducting magnet. This combination of low temperatures and magnetic field is useful for the study of low-T_c superconductors and any material where spin plays an important role.

3.2 Design

Our design is based upon a modified Oxford Instruments Kelvinox 100 dilution refrigerator. The STM head is home-built and its design has been reported previously [8].
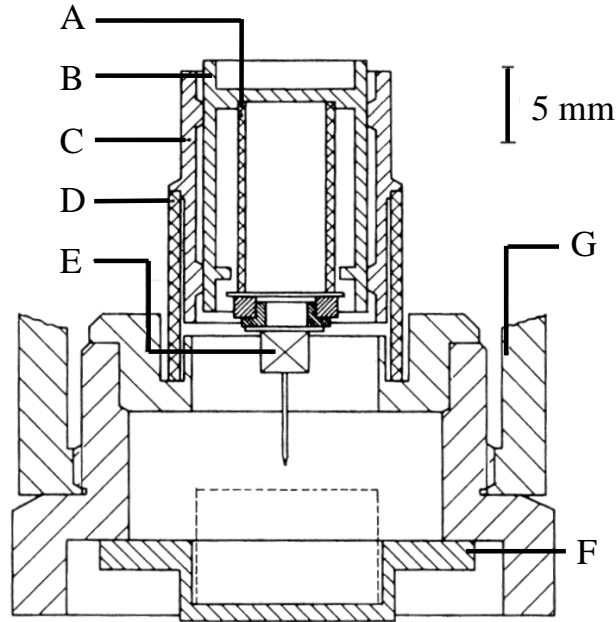
Figure 3.1: Design of the STM head: (A) scan piezo tube, (B) plunger, (C) leaf spring, (D) outer coarse approach piezo, (E) tip holder, (F) sample holder, (G) STM body.

Figure 3.1 is a schematic diagram of the head illustrating the principal features. Briefly, the scanning piezo tube [9] (Fig. 3.1 A) is mounted inside a polished cylinder (Fig. 3.1 B), referred to from now on as the plunger, that is coated with a hard ceramic layer. This can slide vertically inside a second cylinder (Fig. 3.1 C) that has been cut to produce two leaf springs, which grip the plunger. This whole assembly is glued to a large piezo tube [9] (Fig. 3.1 D) using epoxy [10]. When high-voltage pulses of a carefully chosen shape are applied to this piezo the plunger moves up or down with a slip-stick motion. This scan tube

gives a maximum scan area of 1×1 μm^2 at low temperatures. We are able to remove this plunger and replace it with a different one incorporating a longer tube if larger scan areas are required. We do not have the capability of controlled x or y coarse motion. However, we have found that we can move to a random new area by retracting a large number of steps and then reapproaching. We believe that this is due to a small rotation of the plunger while moving.

The design of the STM head is very compact, a cylinder 30 mm in diameter and 58 mm high. This small size is required so that the STM can fit inside the bore of our superconducting magnet. The STM screws onto the bottom of the cold finger attached to the mixing chamber of the dilution refrigerator. The body of the STM is made of copper to provide efficient cooling, and has a large contact area with the cold finger. A calibrated ruthenium oxide resistor attached to the bottom of the mixing chamber is used to measure the temperature. The entire STM is unscrewed and removed to aid sample and tip changing. We operate the STM using control electronics and software supplied by RHK Technology Inc. (SPM 100), a home built $I - V$ converter and an EG+G pre-amplifier. All of the wires entering the cryostat are RF filtered at room temperature.

The sensitivity of an STM to vibrations requires that the head and insert are made as mechanically stiff as possible. Vibration isolation is provided by suspension of the dewar and insert from elastic ropes that are attached to the ceiling. All the pumps for the system are located in the basement below and are electrically isolated and vibrationally decoupled by using flexible pipes. In addition, the circulation pumping lines are also fed through a heavy sand-filled box for further isolation. When a magnetic field is used the magnet is preferentially operated in persistent current mode so that the heavy current leads can be disconnected, as they are a possible source of vibrations. The stability of our measurements, including atomic resolution (see Fig. 3.2), show that these vibration isolation measures are very successful.

To remove the need to disconnect all the wiring and pipes each time the insert needs to be removed from the dewar, we have a system whereby the insert is attached to a frame and the dewar is lowered through the floor. This also speeds up the time that it takes to cool down the insert, as the circulation pipes remain pumped at all times. After raising the dewar and filling with liquid helium it takes approximately 1 hour for the insert to cool down to 4.2 K. The inner vacuum chamber is then pumped to remove the exchange gas before the circulation is started. The whole procedure to go from base temperature to room temperature, changing the tip and sample and returning to base temperature can be done in less than 24 hours.

3.3   Experimental results

The initial experiments to obtain atomic resolution were performed at room temperature using highly oriented pyrolytic graphite. After their successful conclusion we moved on to testing at low temperature. We chose 2H-NbSe$_2$ to provide a means of testing the imaging and spectroscopic capabilities of the STM. This material has been extensively studied in the past [11]. It has a charge density wave and is a superconductor with a T_c of 7.2 K. NbSe$_2$ is a type-II superconductor, so upon application of a sufficiently large magnetic field an Abrikosov vortex lattice is produced. This allows us to test the magnet in the system. In addition, NbSe$_2$ is inert and is easy to cleave to produce large flat areas. For these experiments the samples were cleaved at room temperature and in air just prior to mounting in the STM.
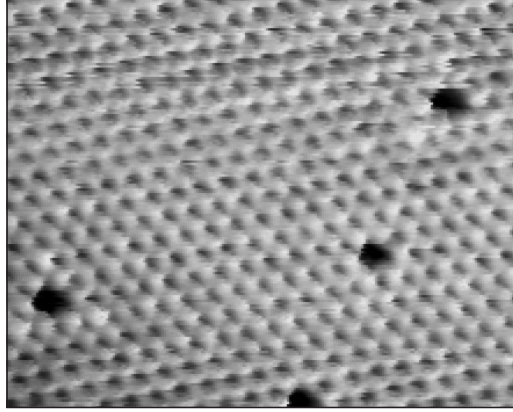
Figure 3.2: Unfiltered 7×5.6 nm^2 atomically resolved constant current image of NbSe$_2$ acquired at 190 mK.

Figure 3.2 is an atomically resolved image of NbSe$_2$ at 190 mK. This image was acquired in constant current mode and is shown here with no filtering. The four black circles are missing single surface atoms. This image demonstrates the low level of vibrational noise in the system. One of the main reasons for operating at low temperatures is the possibility for a high energy resolution. To test these spectroscopic capabilities we measured the differential conductance spectra of NbSe$_2$ using a standard lock-in technique. The a.c. signal applied during these measurements was typically 14 μV_{rms}. We have also been able to measure spectra using a 7 μV_{rms} modulation.

Figure 3.3a shows the differential conductance spectrum measured on NbSe$_2$ with a sample temperature of 210 mK. Ideally we would like to use this spectrum, which has clear peaks and an energy gap characteristic of BCS superconductors,
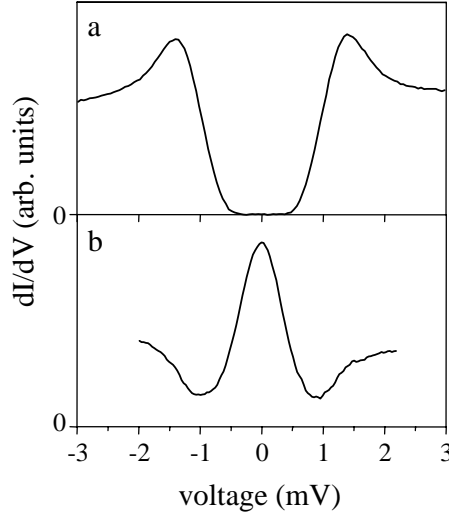
Figure 3.3: a) Differential conductance spectrum of superconducting NbSe$_2$ acquired after stabilizing the feedback at 40 pA and +4 mV at a temperature of 210 mK and zero magnetic field. b) Differential conductance spectrum acquired in the center of a vortex after stabilizing the feedback at 50 pA and +3.5 mV at a magnetic field of 0.2 T and a temperature of 110 mK. (The curves are an average of 128 individual curves.)

to calculate the effective electron temperature, T_{eff}, of the microscope. However, NbSe$_2$ has an anisotropic superconducting energy gap, Δ, varying between 0.7 and 1.4 mV depending on the crystal direction (or **k**-vector) [11]. The curves therefore cannot be fitted to provide a precise value of the effective temperature. This is illustrated by the gradient of the edge of the gap (Fig. 3.3a), which in a BCS superconductor would be a vertical line broadened by the effective temperature only. Nevertheless from these measurements we estimate our effective temperature to be close to that measured by Moussy *et al.* [7], who found $T_{eff} =$ 210 mK with a sample temperature of 60 mK. We are currently reproducing their experiment to determine a more precise value of T_{eff}. To test our superconducting magnet we applied a magnetic field perpendicular to the sample. Since NbSe$_2$ is a type-II superconductor, the field penetrates the sample and an Abrikosov flux lattice is formed. An image of this flux lattice is shown in Fig. 3.4. Figure 3.3b is a differential conductance spectrum measured in the center of a flux vortex, which exhibits a zero bias peak in the density of states. This feature was first observed by Hess *et al.* [11] and has been attributed to quasiparticle bound states within the 'potential well' formed by the vortex [12].

The image in Fig. 3.4 was acquired by recording the signal from the lock-in amplifier while scanning with a sample bias of 1.3 mV. At a bias of 1.3 mV
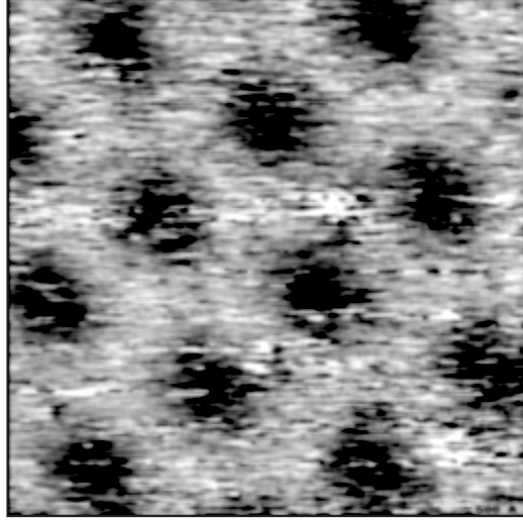
Figure 3.4: 500×500 nm^2 image of the Abrikosov flux lattice formed with a 0.5 T field applied perpendicular to the sample.

the dI/dV signal in the center of the vortex is smaller than the dI/dV signal in the superconducting region and the vortices appear as a dark depressions in the image. For a thorough discussion of the relationship between the measured dI/dV and the LDOS in a vortex core we refer the reader to the work of Hess *et al.* [11]. In many cases it is interesting to measure and map the variation of the LDOS across the sample at a particular bias rather than measure the LDOS versus energy at an individual point. To test this type of measurement we measured the spatial distribution of the quasiparticle density of states around 0 V. This can not be done with a straightforward scanning technique, so a different method is used where at each spatial point the tip is stabilized at a voltage above the gap energy and the feedback loop disengaged. The differential conductance is then measured over a small bias range around 0 V. Finally, the data point for each different bias setting is extracted from each curve and converted to a grayscale to produce an image. One such image using this technique is shown in Fig. 3.5.

White represents a high, and black a low conductance. To enhance the appearance of the shape of various critical features black lines have been added at periodic intervals to this grey scale, resulting in contour like shapes. The most white areas, one of which has been highlighted with a white circle, are the peaks in the LDOS at the vortex cores. The darkest areas, highlighted with white ovals, are superconducting regions. It is immediately noticeable that the vortex core is not completely surrounded by a superconducting region; there is a 6-fold
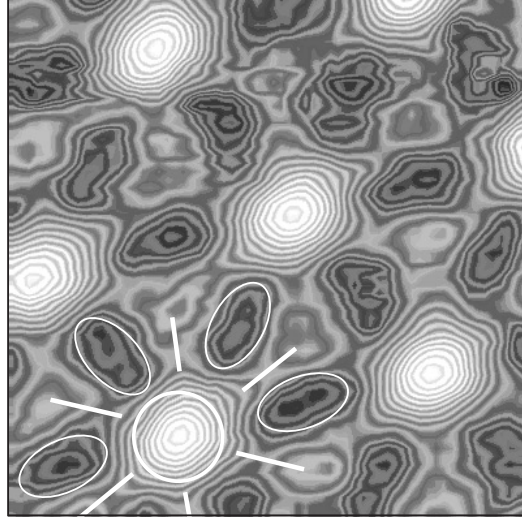
Figure 3.5: Real-space image of the local density of states at 0 V of a 400×400 nm^2 area containing 7 vortices, measured at 0.4 T and 125 mK.

star pattern (that has been highlighted by white lines). Our observations reproduce those of Hess *et al.* and have been explained by including effects from an anisotropic LDOS and an anisotropic pairing [13].

3.4 Conclusions

We have developed an STM attached to a dilution refrigerator operating at 70 mK. We have demonstrated the high quality imaging and spectroscopic capabilities of this instrument. Magnetic fields of up to 12 T can be applied perpendicular to the sample. The combination of low temperatures and a high magnetic field allows investigations of a variety of phenomena including the regime where the Zeeman spin splitting exceeds the thermal broadening ($g\mu_B B > kT$). We are currently pursuing experiments on the properties of unconventional superconductors such as the borocarbides and strontium ruthenates.*

*) For the results on Sr_2RuO_4, see M.D. Upward *et al.*, preprint (2001).

This chapter has been published in Applied Physics A **72**, S253 (2001).

References

[1] G. Binnig, H. Rohrer, Ch. Gerber and E. Weibel, Phys. Rev. Lett. **49**, 57 (1982).

[2] G. Binnig, H. Rohrer, Ch. Gerber and E. Weibel, Appl. Phys. Lett. **40**, 178 (1982).

[3] H. Fukuyama, H. Tan, T. Handa, T. Kumakura and M. Morishita, Czech. J. Phys. **46**, Suppl. S5, 2847 (1996).

[4] S.H. Pan, E.W. Hudson and J.C. Davis, Rev. Sci. Inst. **70**, 1459 (1999).

[5] M. Kugler, Ch. Renner, Ø. Fisher, V. Mikheev and G. Batey, Rev. Sci. Inst. **71**, 1475 (2000).

[6] H.F. Hess, R. B. Robinson and J.V. Waszczak, Phys. Rev. Lett. **64**, 2711 (1990).

[7] N. Moussy, H. Courtois and B. Pannetier, Rev. Sci. Instrum. **72**, 128 (2001).

[8] J.W.G. Wildöer, A.J.A. van Roy, H. van Kempen and C.J.P.M. Harmans, Rev. Sci. Inst. **65**, 2849 (1994).

[9] PZT5H piezoelectric tubes supplied by Morgan Matroc Inc.; scan tube: 12.6 mm long, 6.35 mm diameter, 0.7 mm wall thickness; coarse approach tube: 12.7 mm long, 15.6 mm diameter, 0.8 mm wall thickness.

[10] Stycast is a product of Emerson and Cuming Inc. We have used Stycast 2850FT.

[11] H.F. Hess, R. B. Robinson, R.C. Dynes, J.M. Valles Jr. and J.V. Waszczak, Phys. Rev. Lett. **62**, 214 (1989); H.F. Hess, R.B. Robinson and J.V. Waszczak, Physica B **169**, 422 (1991), and references therein.

[12] A.W. Overhauser and L.L. Daemen, Phys. Rev. Lett. **62**, 1691 (1989); L.L. Daemen and A.W. Overhauser, Phys. Rev. B **40**, 10778 (1989); J.D. Shore, M. Huang, A.T. Doresy and J.P. Sethna, Phys. Rev. Lett. **62**, 3089 (1989); F. Gygi and M. Schlüter, Phys. Rev. B **41**, 822 (1990).

[13] F. Gygi and M. Schlüter, Phys. Rev. Lett. **65**, 1820 (1990); N. Hayashi, M. Ichioka and K. Machida, Phys. Rev. Lett. **77**, 4074 (1996).

Chapter 4

Electronic properties of carbon nanotubes

This chapter discusses the basic electronic properties of carbon nanotubes. First the band structure is calculated starting from the electronic structure of graphite. We then discuss specific properties of the band structure relevant for measurements presented in this thesis.

4.1 Electronic structure

A carbon nanotube can be thought of as a sheet of graphite which is rolled up to form a cylinder. Starting from the band structure of graphite we can calculate the electronic properties of carbon nanotubes by applying periodic boundary conditions [1, 2]. We therefore first calculate the band structure of graphite.

4.1.1 Band structure of graphite

Carbon has four valence electrons available for bonds with other electrons. In a sheet of graphite three electrons form a sp^2 σ bond with the three nearest neighbours. The fourth electron is in a π bond. The electronic properties are well described by considering only this fourth electron [3].

The unit cell of graphite in real space is spanned up by two vectors $\mathbf{a}_1$ and $\mathbf{a}_1$ as is drawn in Fig. 4.1a. The reciprocal unit cell is drawn in Fig. 4.1b with the length of the reciprocal lattice vectors $\mathbf{b}_1$ and $\mathbf{b}_2$ given by $|\mathbf{b}_i| = J_{ab}^{-1} \frac{2\pi}{|\mathbf{a}_i|} = \frac{4\pi}{\sqrt{3}|\mathbf{a}_i|}$. The Jacobian $J_{ab} = \frac{1}{2}\sqrt{3}$ corrects for the use of non-cartesian coordinates.
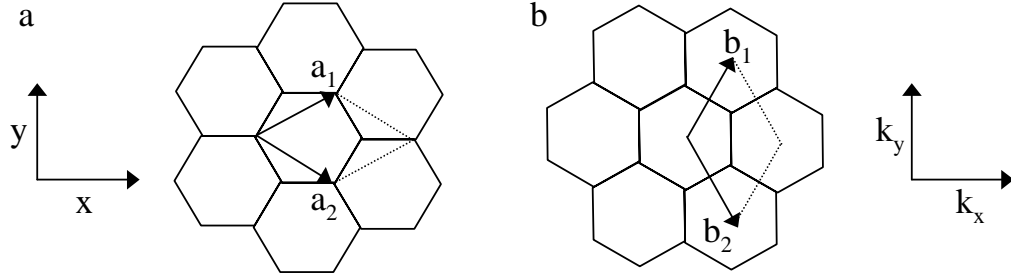
Figure 4.1: a) Definition of the unit cell of graphite in real space. The length of the vectors a_1 and a_2 is the atomic lattice constant $a_0 = 0.246$ nm. b) Unit cell in reciprocal space.

Now the dispersion relation for graphite can be calculated using a tight binding approximation [1]. The solutions are Bloch waves with two dimensional wave vector $\mathbf{k} = (k_x, k_y)$ and energies:

$$E_{2D}(\mathbf{k}) = \pm\gamma_0 \sqrt{1 + 4\cos\left(\frac{\sqrt{3}k_x a_0}{2}\right)\cos\left(\frac{k_y a_0}{2}\right) + 4\cos^2\left(\frac{k_y a_0}{2}\right)} \quad (4.1)$$

Here $a_0 = 0.246$ nm, the length of the real space lattice vectors, and $\gamma_0 = 3.1$ eV is the overlap energy between adjacent π-π carbon orbitals for graphite [4]. For carbon nanotubes this value is measured and we discuss this in chapter 10. In Fig. 4.2 the band structure is plotted. The Fermi surface for graphite is reduces to six points. This makes graphite not a true metal but merely a zero
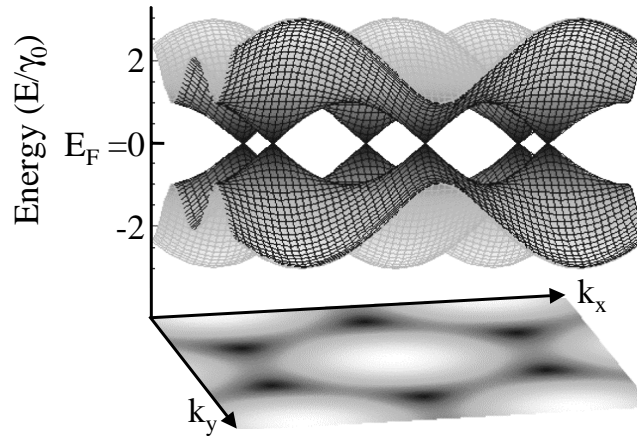
Figure 4.2: Band structure of graphite. At the corners of the hexagonal Brillouin zone the two bands cross the Fermi level. Below a projection of the band structure. The Fermi surface is reduced to six points.

gap semiconductor. Any disturbance of the regular hexagonal lattice will destroy
the symmetry and opens up a small gap at the Fermi level.
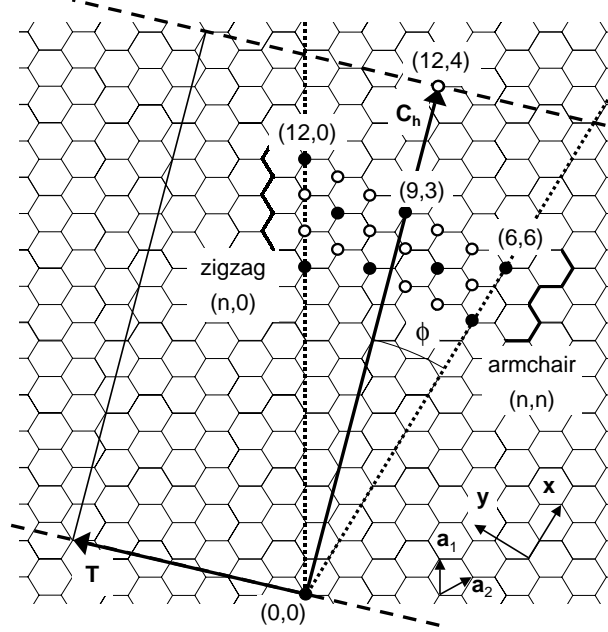
Figure 4.3: Graphene sheet from which different (n, m) tubes can be constructed.
The vector $\mathbf{C}_h$ defines a $(12, 4)$ tube. The zigzag $(n, 0)$ and armchair (n, n) direction,
which have a higher degree of symmetry. Vectors pointing to filled (open) circles define
metallic (semiconducting) tubes.

4.1.2 Band structure of carbon nanotubes

From a sheet of graphite we can construct a carbon nanotube. Using the vector
$\mathbf{C}_h = n\mathbf{a}_1 + m\mathbf{a}_2$ as in Fig. 4.3, a tube is completely identified by the two indices
(n, m). Making two cuts through the graphite sheet orthogonal to this vector
$\mathbf{C}_h$ (the dashed lines in Fig. 4.3) and rolling the sheet up by connecting these
two edges we have formed a (n, m) nanotube (a (12,4) tube in the figure). In
Fig. 4.3 some of the numerous other possible indices are indicated. With the
restriction $m \leq n$ and $m, n \geq 0$ all possible nanotubes are uniquely defined. This
is because vectors $\mathbf{C}_h$ pointing outside the two dotted lines $(n, 0)$ and (n, n) have
an equivalent vector inside these two lines.

A (n, m) tube corresponds to a tube with a diameter $d = \frac{a_0}{\pi}\sqrt{n^2 + nm + m^2}$
and the atoms spiral along the tube axis with a chiral angle $\phi = \cos^{-1}[\sqrt{3}(n + m)/2\sqrt{n^2 + nm + m^2}]$, which is the angle between the (n, n) direction and the
vector $\mathbf{C}_h$.

With these definitions we can calculate the band structure of a (n, m) tube. For waves traveling in the length direction of the tube all possible k values are allowed, assuming that the tube is very long. But in the circumferential direction waves have to obey periodic boundary conditions: $\mathbf{C}_h \cdot \mathbf{k} = 2\pi q$, were q is an integer. The band structure surface of the two dimensional graphite sheet is therefore reduced to a set of one dimensional subbands which are labeled by the index q. The allowed wave vectors k_x and k_y are $N_x\sqrt{3}a_0 k_x + N_y a_0 k_y = \mathbf{C}_h \cdot \mathbf{k} = 2\pi q$. Here N_y and N_x are defined by $(N_y, N_x) = (n, m)$. Substitution into Eq. 4.1 leads to the general dispersion relation for different bands q [4]:

$$E_q(k) = \pm\gamma_0 \sqrt{1 + 4\cos\left(\frac{q\pi}{N_x} - \frac{N_y k a_0}{2N_x}\right)\cos\left(\frac{k a_0}{2}\right) + 4\cos^2\left(\frac{k a_0}{2}\right)} \quad (4.2)$$

There are two special cases in which a nanotube has a higher degree of symmetry than in others, these are the armchair, (n, n) or $\phi = 0°$, and the zigzag, $(n, 0)$ or $\phi = 30°$, directions. We discuss these two cases as they cover all the specific properties of the band structure of carbon nanotubes and are straightforward to calculate.

For a (n, n) armchair tube with $N_x = n$, the allowed wave vectors $k_{x,q}$ are $N_x\sqrt{3}a_0 k_{x,q} = 2\pi q$, with $q = 1, .., N_x$. Inserting this in Eq. 4.1 gives:

$$E_q(k_y) = \pm\gamma_0 \sqrt{1 \pm 4\cos\left(\frac{q\pi a_0}{N_x}\right)\cos\left(\frac{k_y a_0}{2}\right) + 4\cos^2\left(\frac{k_y a_0}{2}\right)} \quad (4.3)$$

where now k_y is the one-dimensional wave vector k (i.e. along the tube axis). In Fig. 4.4a we have plotted Eq. 4.3 for a $(6, 6)$ tube. Two linear bands cross the Fermi level which is why armchair tubes are metallic.

For a $(n, 0)$ zigzag tube with $N_y = n$, the allowed wave vectors $k_{y,q}$ are $N_y a_0 k_{y,q} = 2\pi q$ with $q = 1, .., N_y$. The one dimensional wave vector along the axis of the tube is now k_x. We discuss this difference in one dimensional wave vector further on. The dispersion relation becomes:

$$E_q(k_x) = \pm\gamma_0 \sqrt{1 \pm 4\cos\left(\frac{\sqrt{3}k_x a_0}{2}\right)\cos\left(\frac{q\pi}{N_y}\right) + 4\cos^2\left(\frac{q\pi}{N_y}\right)} \quad (4.4)$$

Zigzag tubes with n a multiple of 3 are metallic. Others are semiconducting as can be seen in Fig. 4.4b where we plotted Eq. 4.4 for a $(7, 0)$ tube. There is a finite gap between the bands above and below the Fermi level.

Tubes which are not zigzag or armchair are called chiral tubes. These tubes can be either metallic or semiconducting depending on the (n, m) indices. Tubes
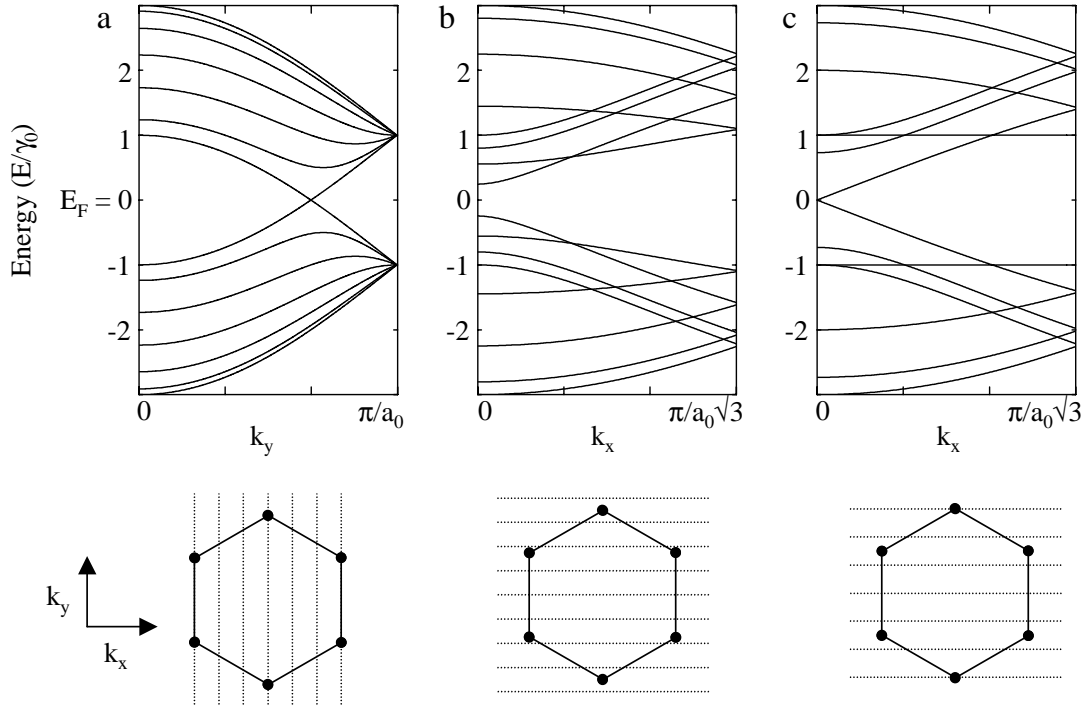
Figure 4.4: Calculated band structure for different carbon nanotubes. a) A $(6,6)$ armchair tube with two bands crossing the Fermi level which makes this tube metallic. Below the plot the hexagon represents the first Brillouin zone. The lines are allowed k values due to the quantization of k. Because the lines cross the Fermi points this tube is metallic. b) A $(7,0)$ zigzag tube with a finite distance between the bands around the Fermi level. This tube is semiconducting. The allowed k values do not cross the Fermi points so a finite energy is needed before there are possible excitations. c) Band structure for a $(6,0)$ zigzag tube. This tube is 'metallic', as can also be seen by the lines crossing the upper and lower Fermi points.

are semiconducting unless $(n - m)$ is a multiple of 3. If $(n - m)$ is a multiple of 3, the tube shows metallic behavior, but is in fact a zero gap semiconductor because the bands only touch at the Fermi level. Zigzag tubes also obey this rule. For zero gap semiconductors breaking of symmetry opens up a small gap. The origin and observation of this gap is discussed in section 4.2.

The dramatic change in electronic properties, metallic or semiconducting behavior for only slighty different (n, m) indices, becomes transparent if we draw the quantization conditions in reciprocal space. In Fig. 4.4a the first Brillouin zone for the $(6, 6)$ tube is drawn. This tube is metallic because the lines, which represent the allowed k values, cross the corners of the hexagon. In Fig. 4.4b the first Brillouin zone is drawn for a $(7, 0)$ tube. The lines do not cross the Fermi

points. This tube is semiconducting because a finite energy is needed before k values are available.

4.1.3   Density of states

From the band structure we are able to calculate the density of states (DOS) by adding up all possible states at a specific energy. In Fig. 4.5 the band structure and DOS for a $(6,6)$ armchair tube and a $(7,0)$ zigzag tube are plotted. Both metallic tubes (which have a finite DOS at the Fermi level) and semiconducting tubes (with zero DOS around the Fermi level) have bands that become available at higher energies. This leads to so-called van Hove singularities where on one side the DOS sharply rises. The one dimensional nature of the subbands manifests itself by a reduction of the DOS with $\sqrt{E}$ on the other side [5]. In Fig. 4.5a we label the energy difference between the first two van Hove singularities ΔE_{sub}, the subband separation.
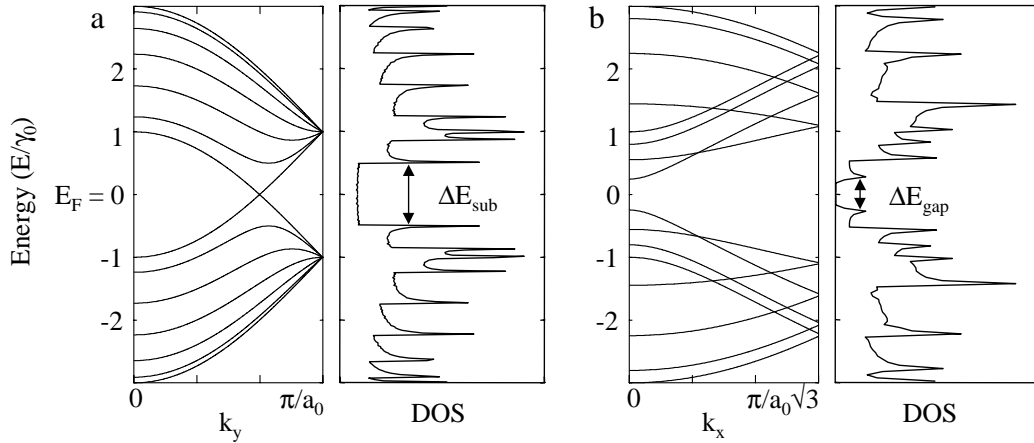
Figure 4.5: a) Band structure and corresponding density of states for a $(6,6)$ armchair tube. The DOS is calculated by adding up all available states at a specific energy. No units are given as we are only interested in the shape. ΔE_{sub} is the energy separation between the first two onsets of subbands. b) Band structure and DOS for a $(7,0)$ zigzag tube. The semiconducting gap is indicated by ΔE_{gap}.

In Fig. 4.5b the DOS around the Fermi level is zero and the energy difference between the first van Hove singularities is labeled as ΔE_{gap}, the semiconducting gap. Both ΔE_{sub} and ΔE_{gap} are inversely proportional to the diameter d of the tube: $\Delta_{gap} = 2a_0\gamma_0/\sqrt{3}d$ and $\Delta_{sub} = 6a_0\gamma_0/\sqrt{3}d$. Note that for equal diameters $\Delta_{sub} = 3\Delta_{gap}$. The spacings between van Hove singularities follow simple rules which are discussed in chapter 5.

4.1.4 Wave vector

In Fig. 4.4a k_y is the one dimensional wave vector and in Fig. 4.4c k_x. The value of k at the Fermi level is different in both cases due to a different choice for the unit cell. For a zigzag tube a more convenient rectangular shaped unit cell can be chosen than the unit cell for an armchair as drawn in Fig. 4.1. The reason for this is the 30° change in chiral angle between an armchair and a zigzag tube. However, the spatial structure of the waves in carbon nanotubes will still have $3a_0$ periodicity. In chapter 9 the periodicity of the wave function in an armchair nanotube is measured which equals $3a_0$, as expected. In chapter 10 the full spatial structure is measured of a chiral metallic tube and indeed the periodicity is again $3a_0$.

4.2 Energy gaps in 'metallic' tubes

For the $(6,0)$ tube in Fig. 4.4c the lines cross the Fermi points but for the $(6,6)$ armchair tube quantization lines coincide with an edge of the Brillouin zone. This means that for the $(6,0)$ tube the two bands touch at the Fermi level whereas for the $(6,6)$ tube the bands cross the Fermi level. For the $(6,0)$ tube any breaking of symmetry opens up a small gap. In fact, the curvature of the tube is already responsible for a small gap round E_F, since the overlap between the π orbitals changes for tubes with a finite chiral angle [6]. The curvature does change the overlap of orbitals in an armchair tube because of the more symmetric arrangement of atoms. Armchair tubes are therefore real metals and chiral 'metallic' tubes are in fact small gap semiconductors.

This small gap is measured in transport measurements [7]. By tuning a gate voltage the small gap was observed as a suppression in the conductance through the tube. More recently this gap is seen in scanning tunneling spectroscopy curves [8]. In Fig. 4.6 the results of this measurement are plotted.

In Fig. 4.6a the normalized dI/dV curve is plotted for a $(15,0)$ zigzag tubes. Where the width of the semiconducting gap is inversely proportional to the diameter, the small gap is is inversely proportional to the square of the diameter:

$$E_{smallgap} = \frac{\gamma_0 {a_0}^2}{4d^2} \sin(3\phi) \tag{4.5}$$

The size of the gap depends further on the chiral angle ϕ and is largest for zigzag tubes, where $3\phi = 90°$. In Fig. 4.6b the experimental results and relation 4.5 are plotted, showing the agreement between theory and experiment.

We observe similar gaps in our spectroscopy curves but we can not explain
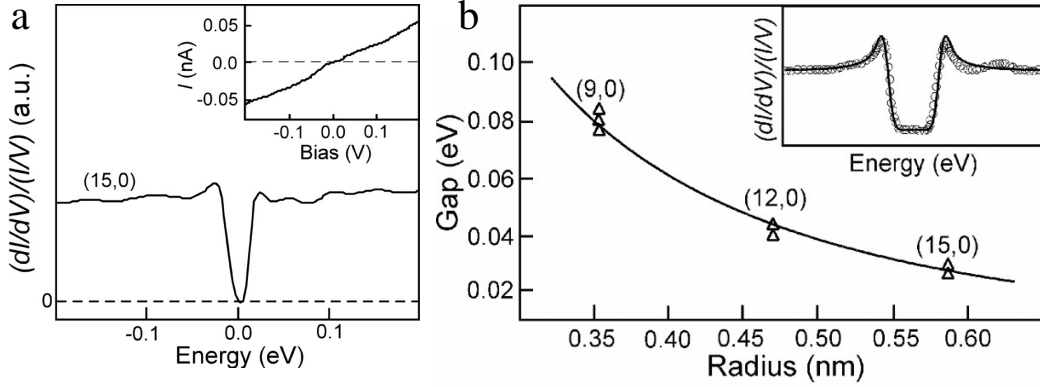
Figure 4.6: a) Low energy spectroscopy $(dI/dV)/(I/V)$ measured on a $(15,0)$ zigzag tube. The I/V curve is plotted in the inset. b) The width of the observed gap for a $(9,0)$, a $(12,0)$ and a $(15,0)$ zigzag tube plotted as a function of diameter. The gapsize is inversely proportional to the square of the diameter (solid line). The inset shows a fit to the measured gap on a $(9,0)$ zigzag tube. Reproduced from Ref. [8].

them with this model as our gaps are not in the center of the band structure. In chapter 8 we discuss our observations.

4.3   Discrete states in short nanotubes

In chapter 2 we showed that a slice at a voltage V out of a 3 dimensional $dI/dV(x,y,V)$ dataset corresponds to a spatial map of the individual wave function $|\psi_j|^2$, given that the energy resolution δ is better than the energy level spacing $\varepsilon_{j+1} - \varepsilon_j$. This condition can be fulfilled if the length L of a nanotube is short enough. In chapters 9 and 10 we present measurements of the shape of these wave functions in, respectively, one and two dimensions. In chapter 10 we also exploit the measured images to probe the dispersion relation of carbon nanotubes. Here we give some additional background on the properties of discrete states in a short carbon nanotube. We follow Ref. [9].

4.3.1   Two families of discrete states

For small energies, $E/\gamma_0 < \frac{1}{2}$, two right and two left moving Bloch waves with slightly different wave vectors k_1 and k_2 travel along the length direction of a carbon nanotube, see Fig. 4.7a. The waves are reflected by the ends, which are, in general, not perfect symmetric caps. This asymmetry leads to a mixing of the incoming and outgoing waves. Superimposing waves with wave vector k_1 and k_2

leads to a wave function with a wave vector $(k_1 + k_2)/2$, which is here equal to k_F, modulated by an envelope function with wave vector $(k_1 - k_2)/2$. The envelope function changes as a function of energy since the difference between k_1 and k_2 changes, see Fig. 4.7a. Measuring the envelope function as a function of energy thus yields information on the dispersion relation of carbon nanotubes.
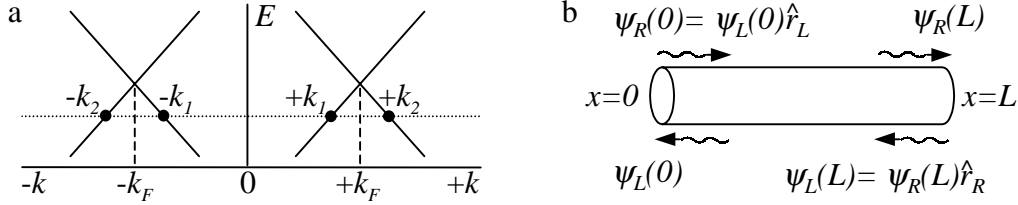
Figure 4.7: a) Band structure around E_F. Four waves with wave vector $\pm k_1$ and $\pm k_2$ travel along the tube. b) Right moving waves are reflected into left moving waves, and vice versa, by reflection matrices $\hat{r}_R$ and $\hat{r}_L$.

The exact nature of mixing at the ends is unknown and therefore we describe the reflection at the ends by unknown 2×2 reflection matrices $\hat{r}_L$ and $\hat{r}_R$. The waves, described by the two component function ψ_0, become a standing wave if they fulfill the condition $\psi_0 = \psi_0 \hat{r}_R \hat{r}_L e^{2iqL}$. Solving this eigenvalue problem gives $e^{i\delta_\gamma}$ as eigenstates for $\hat{r}_L \hat{r}_R$, with $\gamma = (1, 2)$. The energies of the discrete states become $E_{\gamma m} = \hbar v_F q_{\gamma m}$, with $q_{\gamma m} = (2\pi m - \delta_\gamma)/2L$. Thus, the mixing of waves leads to two distinct families labeled by $\gamma = (1, 2)$ and within a family states are numbered by m. The energy difference between states in a family is $h v_F/2L$, and in between families $\hbar v_F (\delta_1 - \delta_2)/2L$.

These two families should be observable by, for example, peak pairing of the discrete energy states in a spectroscopy curve. In Fig. 10.1c peaks are paired at first sight, but in a more detailed analysis we were not able to quantify this.

4.3.2   Wave function images

The simple 'particle in a box' can not account for the full spatial structure of wave functions in a carbon nanotube. Wave functions can be visualized by their two dimensional projection on a cylinder at a height h above the nanotube. The shape of the discrete states can be calculated from a superposition of Bloch waves in the nanotube. Only the lowest Fourier components contribute to such an image as Fourier components fall off exponentially with h and wave vector $\mathbf{k}$. The Fermi surface of graphite consists of six points with wave vectors $\pm \mathbf{k}_n^0$ with $n = -1, 0, 1$. Three independent Fourier components thus describe the total wave

function image. Since a wave function has to be zero at the center of a hexagon these components have to obey the nodal constraint $\sum_n \phi_{j,n} = 0$.

For sets of Fourier components for wave functions of different states there are also other constraints which ensure that wave functions are orthogonal. These constraints can be calculated assuming energy independent reflection at the ends [9]. The measured images in chapter 10 do not obey these constraints indicating that reflection at the ends is likely to be energy dependent.

References

[1] J.W. Mintmire, B.I. Dunlap and C.T. White, Phys. Rev. Lett. **68**, 631 (1992)

[2] N. Hamada, S. Sawada and A. Oshiyama, Phys. Rev. Lett. **68**, 1579 (1992).

[3] P.R. Wallace, Phys. Rev. **71** 622 (1947).

[4] M.S. Dresselhaus, G.Dresselhaus and P. C. Eklund, *Science of Fullerenes and Carbon Nanotubes* (Academic Press Inc., San Diego, 1996).

[5] N.W. Ashcroft and N.D. Mermin, *Solid State Physics* (Holt, Rinerhart and Wilson, New York, 1976).

[6] C.L. Kane and E.J. Mele, Phys. Rev. Lett. **78**, 1932 (1997).

[7] C. Zhou, J. Kong and H. Dai, Phys. Rev. Lett **84**, 5604 (2000).

[8] M. Ouyang, J.-L. Huang, C.L. Cheung and C.M. Lieber, Science **292**, 702 (2001).

[9] A.A. Maarouf, N.R. Wilson and C.L. Kane, submitted to Phys. Rev. B.

Chapter 5

Spatially resolved scanning tunneling spectroscopy on single-walled carbon nanotubes

L.C. Venema, J.W. Janssen, M.R. Buitelaar,
J.W.G. Wildöer, S.G. Lemay,
L.P. Kouwenhoven and C. Dekker

Scanning tunneling microscope spectroscopy is used to study in detail the electronic band structure of carbon nanotubes as well as to locally investigate electronic features of interesting topological sites such as nanotube ends and bends. From a large number of measurements of the tunneling density of states (DOS) nanotubes can be classified, according to predictions, as either semiconducting (two-third of the total number of tubes) or metallic (one-third). The energy subband separations in the tunneling DOS compare reasonably well to theoretical calculations. At nanotube ends, spatially resolved spectra show additional sharp conductance peaks that shift in energy as a function of position. Spectroscopy measurements on a nanotube kink suggest that the kink is a heterojunction between a semiconducting and a metallic nanotube.

5.1 Introduction

The electronic and atomic structure of a carbon nanotube are related to each other in a remarkable way. A nanotube can be thought of as a rolled up graphene sheet where two parameters, the chirality ϕ of the hexagonal lattice along the nanotube shell and the diameter d fully describe its atomic structure [1]. The indices (n, m) of a nanotube correspond to a specific combination of chiral angle

ϕ and diameter d. Depending critically on these (n, m) indices, a nanotube can be either semiconducting or metallic [2, 3, 4]. Of all possible (n, m) nanotubes, roughly one third is predicted to be metallic.

Scanning tunneling microscopy (STM) has proven to be a very useful technique to investigate carbon nanotubes since both the atomic and electronic structure can be investigated for individual nanotubes [5-14]. Atomically resolved imaging enables to observe the chiral structure of a nanotube. In addition, the electronic density of states (DOS) can be measured for the same tube by scanning tunneling spectroscopy (STS). The DOS of carbon nanotubes in theory consists of a number of one-dimensional (1D) subbands due to the quantization of available energy modes in the circumferential direction [2, 3, 4]. This may be seen for example in the theoretically calculated DOS for a semiconducting and a metallic nanotube in Fig. 5.2 (curves 1 and 6, respectively). The subband onsets are sharp van Hove singularities due to the one-dimensional nature of the subbands. The energy intervals at which the subband onsets appear depend on whether the tube is metallic or semiconducting and on the nanotube diameter [15, 16]. Recent STS measurements verified the general features predicted for the DOS. Nanotubes were found to be either semiconducting or metallic and also van Hove singularities could be observed [10, 11, 14]. Attention is now directed towards the electronic structure of topologically interesting sites in nanotubes, such as ends, bends and kinks. These sites can be studied spatially resolved by STS. Carrol *et al.* [9] observed sharp STS resonances at the tip of multi-walled nanotubes that could be associated with a particular cap structure. Recently, Kim *et al.* [14] also observed peaks in the DOS at the end of a metallic single-walled nanotube. They attributed this result to a specific arrangement of pentagons at the cap. Another interesting topological effect is a junction between two nanotubes with different (n, m) numbers, which appears as a sharp bend, or 'kink'. Section 5.3.2 discusses a measurement on a sharply bent nanotube that appears, from spectroscopy curves above and below the kink, to be a molecular semiconductor-metal heterojunction.

In this paper we review results from a large number of STS measurements on individual nanotubes. The main features of the electronic DOS as well as locally resolved data on tube ends and a tube kink are discussed in section 5.3. The following section first gives details of the sample and measurement methods.
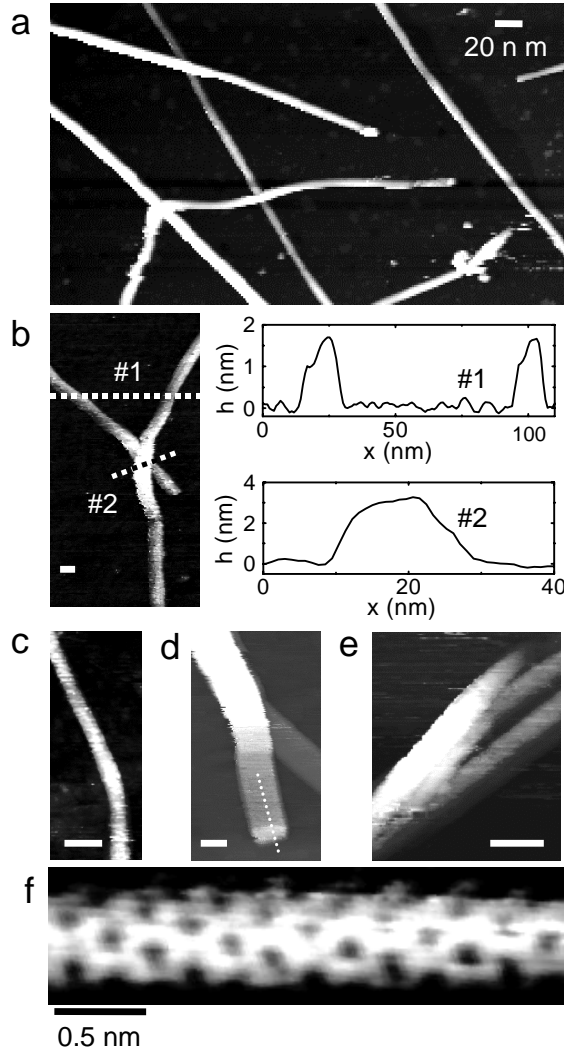
Figure 5.1: STM images at room temperature (a), and at 4 K (b-f). The scale bar in b-e is 10 nm. a) Large-scale image where various nanotubes and small bundles on a surface of Au(111) can be observed. b) Crossing of two nanotubes. The curves on the right are two height profiles taken along the dashed lines indicated in the image. h is the height, x is the coordinate along the lines. c) A sharply bent nanotube. d) An end of a nanotube that splits off from a bundle. The dotted line illustrates how a series of STS curves can be taken to observe gradual changes in the local DOS at the end. e) A bundle in which individual nanotubes can be discerned. f) Atomically resolved image of a chiral nanotube. The image is corrected for the geometrical distortion that stretches the apparent nanotube lattice in the direction normal to the tube axis [21].

5.2   Experimental details

Measurements were performed on samples of Au (111) surfaces with single-walled carbon nanotubes that were synthesized by laser evaporation (by R.E. Smalley and coworkers) [17]. The Au (111) was prepared by melting pieces of about 15 mm^3 from a 99.99% pure gold wire in a gas flame. The single-crystalline (111) facets appearing on the surface during cooling were used as substrates. Pieces of nanotube soot were dispersed in dichloroethane and ultrasonically agitated to unravel the bundles of tubes. A droplet of the dispersion was then deposited on the substrates of Au (111) in ambient conditions. The measurements were done in a home-built 4K STM. STM tips were mechanically cut from a Pt(90%)Ir(10%) wire. Imaging was done in constant-current mode at typical parameters of 60 pA for the tunnel current I and 0.1 V for the bias voltage V.

Some examples of nanotubes imaged with STM at room temperature (a) and at 4 K (b-f) are shown in Fig. 5.1. The scale bar in Fig. 5.1b-d corresponds to 10 nm. The apparent width of the nanotubes varies between 5 and 20 nm. This scale is determined by the size of the STM tip rather than the nanotube diameter which is in the range of 1.4 nm. Various nanotubes and small bundles can be seen in the image of Fig. 5.1a. Carbon nanotubes usually lie straight on the surface but may be deformed due to irregularities in the surface such as monoatomic steps or crossings with other tubes. Hertel *et al.* showed that single-walled carbon nanotubes may experience substantial deformations at surface irregularities due to the large van der Waals binding energies between nanotubes and the substrate surface [18].* The nanotube emerging from the left bottom corner in Fig. 5.1a is indeed bent strongly at the crossings with two other nanotubes. The total lateral extent of such bends is typically about 30 nm. The STM images of Figs. 5.1b-e show details of respectively a crossing, a sharp bend, a nanotube end and a bundle in which several individual nanotubes can be resolved. The right part of Fig. 5.1b are two height profiles $h(x)$ that are taken along the dashed lines shown in the STM image on the left. From the top profile, the individual nanotubes have an apparent height relative to the surface of 1.70 and 1.65 nm. Taking into account a van der Waals distance between the tubes and the surface of about 0.25 nm [19], the diameters are 1.45 and 1.40 nm. The crossing of the two tubes, shown in the bottom $h(x)$ profile, has a total height of 3.35 nm. This corresponds to the sum of the individual tube heights and a van der Waals distance between the nanotubes and between the lower nanotube and the surface. Figure 5.1c is an image of a sharply bent nanotube, or possibly of a nanotube 'kink'. As mentioned in the introduction, kinks can be junctions between different nanotubes. Figure

---

*) See also chapter 7.

5.1d is zoomed in on a nanotube that splits off from a small bundle. The dotted line crossing the end of the nanotube is an example of a line along which a series of spectroscopy measurements can be taken to observe the change in the local DOS at the end of the tube. Such measurements are discussed in section 5.3.2. Figure 5.1e shows a bundle of nanotubes in which the individual nanotubes can be discerned. Figure 5.1f is an atomically resolved image of a chiral nanotube. The image has been corrected for the geometric distortion that stretches the apparent carbon lattice in the direction perpendicular to the tube [20, 21]. The chiral angle obtained from Fig. 5.1f is $21 \pm 1°$. In general, a large variety of chiral angles could be found for this nanotube material, ranging from zigzag to armchair. Diameters that are measured from apparent height measurements are in general quite small, about 0.9 nm, which is probably due to the flattening of nanotubes by tip forces during imaging [21]. More reliable values can be obtained from tunneling spectroscopy measurements. As will be discussed in detail below, the energy differences between the subbands in the DOS depend strongly on the diameter. Using this to deduce the diameter, values of $\sim 1.1 - 1.5$ nm are found, which corresponds reasonably well to TEM measurements where diameters of about 1.4 nm were determined [17].

All spectroscopy measurements presented in this paper were done at 4 K and on individual nanotubes. Current-voltage ($I(V)$) tunnel spectra were taken by switching off the feedback and recording the current as a function of the bias voltage while keeping the STM tip at a fixed position. $dI/dV(V)$ curves (from here called dI/dV curves) were numerically calculated from $I(V)$ spectra. dI/dV can be taken as a measure for the DOS.

5.3 Experimental results

5.3.1 Density of states

Long nanotubes

Two classes of DOS are expected for nanotubes, one for semiconducting and one for metallic nanotubes. The curves 1 and 6 in Fig. 5.2, represent the theoretical DOS for a $(11, 7)$ and a $(9, 9)$ tube, which have approximately the same diameter but are semiconducting and metallic respectively. Two types of dI/dV spectra taken with STM can indeed be distinguished for various nanotubes. Several examples are shown in Fig. 5.2. The left figure shows dI/dV curves (2-5) with various peaks and a small energy gap ΔE_{gap} of about 0.7 V. The right figure, curves (7-10), have only two clear peaks or onsets in the displayed voltage

range and have a large plateau of constant conductance around zero bias ΔE_{sub} of about 1.9 V in width. The experimentally obtained spectra compare well to the theoretical curves. Both energy differences ΔE_{gap} and ΔE_{sub} should scale in theory inversely linear with the diameter of a nanotube. Semiconducting nanotubes with a diameter of 1.4 nm have an energy gap $\Delta E_{gap} = 2d_{nn}\gamma_0/d \approx 0.6$ eV where $d_{nn} = 1.42$ Å is the distance between nearest neighbor carbon atoms and $\gamma_0 = 2.9$ eV is the energy overlap integral between nearest neighbors [22].*

For metallic nanotubes, the separation ΔE_{sub} between the onsets is $\Delta E_{sub} = 6d_{nn}\gamma_0/d \approx 1.8$ eV for $d = 1.4$ nm. In this case, there is no energy gap but the DOS between the subbands is finite (albeit small) and constant. The experimentally obtained ΔE_{gap} and ΔE_{sub} correspond to these calculated values. Out of 29 nanotubes on which dI/dV spectra have been obtained, 19 were semiconducting and 10 were metallic. This result confirms the prediction that about one third of the (n, m) nanotubes is metallic and two third is semiconducting.

It is well known from STS literature that at large bias voltage the tunnel barrier is reduced considerably, which leads to an overestimated DOS at higher bias [23]. To account for this effect, dI/dV can be normalized by I/V. The top curves 5' and 10' in Fig. 5.2 are normalized spectra, $dI/dV/(I/V)$, calculated from curves 5 and 10. The normalization technique is especially useful for metallic spectroscopy curves since the first onsets appear at a relatively high voltage, around ± 1 V. The peak shapes of the subband onsets are enhanced by the normalization as can be observed for the metallic curve 10'. The value for ΔE_{sub} determined from the normalized curves is slightly smaller, by about 0.03 eV, as compared to the value found from dI/dV curves, due to a small shift of the onsets. For the semiconducting curves, the normalization does not significantly affect the intervals between the subband onsets since they are smaller. The normalized curves are smoothed near zero bias because of the large divergences from the normalization procedure. Determining the peak position of the first valence subband onset for the semiconducting curves often is problematic because small noise fluctuations may lead to spurious peaks. We therefore use the normalization technique for metallic nanotubes to obtain the most reliable value for ΔE_{sub}, but determine the intervals between subband onsets for semiconducting nanotubes from dI/dV curves.

Various energy intervals ΔE_{i-j}, both above and below the Fermi energy, are indicated for the semiconducting curve in Fig. 5.3b. The differences between

---

*) From more recent experiments, shown in chapter 10 of this thesis, we obtain a value for γ_0 of 2.6 eV. With this value the diameters deduced from spectroscopy measurements are in better agreement with diameters obtained from height measurements. The statement that the nanotubes are probably flattened by tip forces is therefore less relevant.
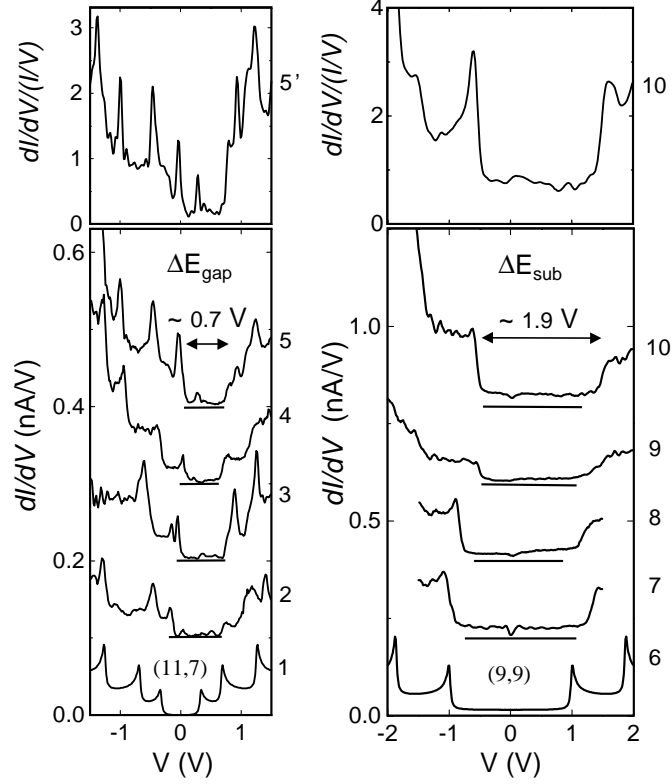
Figure 5.2: Experimental and theoretical DOS for semiconducting (left) and metallic (right) nanotubes. For clarity the curves are vertically offset by 0.1 and 0.2 nA/V respectively. The DOS consists of a number of subbands with sharp (van Hove) singularities at the onsets. Curves 1 and 6 represent the theoretical DOS for a $(11, 7)$ and a $(9, 9)$ nanotube, which are semiconducting and metallic respectively. Curves 2-5 are dI/dV spectra taken by STM on nanotubes that can be identified as semiconducting and have an energy gap ΔE_{gap} of about 0.7 V. Curves 7-10 are spectra on nanotubes that can be identified as metallic and have a large plateau of constant conductance ΔE_{sub} of about 1.9 V. The curves 5' and 10' in the top parts are normalized curves, obtained from 5 and 10.

the subband onsets follows within a good estimate a simple rule [15, 16]. From the approximately linear energy dispersion near the Fermi level for graphene, the first four van Hove singularities for semiconductors can be found to appear at energies $E_1 = \pm d_{nn}\gamma_0/d$, $E_2 = \pm 2d_{nn}\gamma_0/d$, $E_3 = \pm 4d_{nn}\gamma_0/d$ and $E_4 = \pm 5d_{nn}\gamma_0/d$. The separations between the singularities are then $\Delta E_{2-1} = d_{nn}\gamma_0/d = \frac{1}{2}\Delta E_{gap}$, $\Delta E_{3-2} = 2d_{nn}\gamma_0/d = \Delta E_{gap}$ and $\Delta E_{4-3} = d_{nn}\gamma_0/d = \frac{1}{2}\Delta E_{gap}$. For a metal, the Van Hove singularities appear at energies $E_1 = \pm 3d_{nn}\gamma_0/d$, $E_2 = \pm 6d_{nn}\gamma_0/d$ and $E_3 = \pm 9d_{nn}\gamma_0/d$. The separations ΔE_{i-j} are therefore all of the size $3d_{nn}\gamma_0/d = \Delta E_{sub}$. It is difficult to observe several energy intervals in the metal-
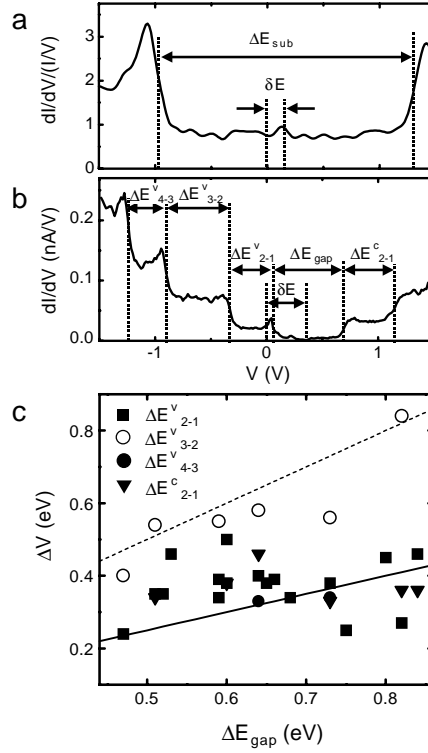
Figure 5.3: Analysis of energy intervals between subbands and the shifts of the Fermi level. a) Metallic $dI/dV/(I/V)$ spectrum in which ΔE_{sub} and Fermi level shift δE are indicated. b) Semiconducting dI/dV spectrum with several subband onset separations indicated, ΔE_{i-j}^{v} for the valence band and ΔE_{i-j}^{c} for the conductance band. The shift of the Fermi level δE is also shown. c) Subband intervals $\Delta E_{i-j}^{v,c}$ in voltage differences ΔV plotted as a function of the energy gaps for about 20 semiconducting nanotubes. The solid line represents $\frac{1}{2}\Delta E_{gap}$ and the dotted line ΔE_{gap}.

lic case since the onsets appear at large energies ($|V|\gtrsim 1$ V, see for example Fig. 5.3a). However, in the semiconducting spectra, three to five subband onsets are usually visible. In Fig. 5.3c energy differences that were obtained for about 20 semiconducting nanotubes are plotted against the energy gap of each tube and compared with ΔE_{gap} (dotted line) and $\frac{1}{2}\Delta E_{gap}$ (solid line). There is much scatter in the data, but it can be observed that the first and third subband separations (closed squares, circles and triangles) are near the $\frac{1}{2}\Delta E_{gap}$ line whereas the second subband separations (open circles) are closer to the ΔE_{gap} line. This observation is in agreement with the simple rule of alternating subband spacings. Deviations in the positions of the subband onsets may occur due to the nonlinearity of the graphene energy dispersion far away from the Fermi energy and due to hybridization with the gold substrate.

Also indicated in Fig. 5.3a and b is the shift δE of the spectra relative to zero bias. This shift can be attributed to the charge transfer between the gold-nanotube interface due to the difference in work function. Au has a work function of ~ 5.3 eV, whereas nanotubes were found to have a work function of about 4.3 eV [24, 25]. The aligning of the Fermi levels by transfer of electrons from nanotube to gold leads to an asymmetric position of the nanotube band structure relative to the Fermi level. From the STS spectra we find that δE is about 0.3 ± 0.1 eV for both metallic and semiconducting nanotubes, independent of ΔE_{gap} and ΔE_{sub}. This agrees with the theoretical Fermi level shift of about 0.2 eV as a result of the charge transfer between a metallic substrate and a nanotube [26]. In the case of the semiconducting nanotubes the Fermi level is actually shifted into the valence band. For metallic tubes the Fermi level stays well within the plateau between the subband onsets ΔE_{sub}.

Often, a suppression of the tunneling conductance near zero bias can be observed, see for example the metallic dI/dV curves 7 and 10 in Fig. 5.2. This zero bias anomaly is also sometimes present in spectra taken on the bare gold substrate away from nanotubes. The suppression of the tunneling DOS at the Fermi energy for disordered conductors is a well-known problem in the literature [27, 28]. It was found that electron-electron interactions in the presence of impurities results in a negative correction to the DOS, which is singular at the Fermi energy. This theory may apply to the present case, since the STM tip is likely to be a disordered conductor as it is made from an alloy of Pt and Ir. In a more classical point of view, the system can be described by a tunnel junction between the STM tip and the sample in series with a resistance closeby. The disordered tip material leads to the resistance in this case. If the resistance is large enough to inhibit fast recharging after a tunneling event, there will be a blockade of current when the external voltage is smaller than the charging energy [29]. The zero bias anomaly in nanotubes is possibly enhanced by the Luttinger liquid [30, 31].*

Short nanotubes

In short nanotubes the DOS may show additional structure due to finite size effects. For nanotubes of finite length the available energy states in the length direction will be quantized. For finite metallic nanotubes it has been shown that the energy bands that cross at the Fermi level consist of well-separated single electron states that are coherent over a considerable length of the nanotube

---

*) In chapter 8 the suppression of the differential conductance at zero bias on carbon nanotubes is discussed in more detail and possible models to explain our observations are reviewed.

[32, 33, 34]. The energy level splitting ΔE_L scales inversely linear with the length L, as $\Delta E_L = h v_F / 2L$, where $v_F = 9 \times 10^5$ m/s is the Fermi velocity. Discrete energy levels can be observed by cutting nanotubes into small pieces using voltage pulses to the STM tip [35].
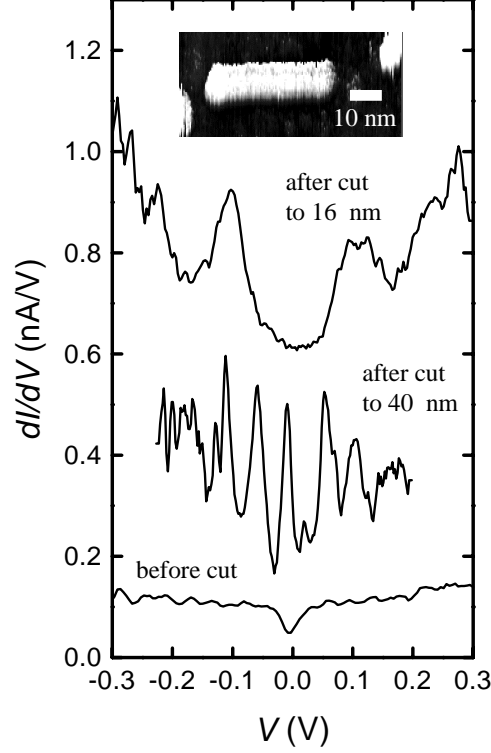
Figure 5.4: *dI/dV* spectra zoomed in at low energies on a metallic nanotube that has been cut into short pieces to observe energy level splitting. The inset shows a topographic image of the tube after it was cut by voltage pulses to a piece of 40 nm. The bottom spectrum was taken on the nanotube before it was cut. The tunneling conductance shows an oscillatory behavior (middle curve) with a period of about 50 mV for the 40 nm piece. After cutting the tube to 16 nm, the period is about 160 mV (top curve). The top curve is offset vertically for clarity by 0.6 nA/V. The middle curve is not offset, but was taken at a smaller tunnel distance and therefore has a higher tunneling conductance.

The inset of Fig. 5.4 shows a nanotube that was cut into a piece of about 40 nm. Its metallic character is apparent from *dI/dV* measurements before the cuts, that were similar to the metallic curves in the right plot of Fig. 5.2. After the nanotube was cut into a piece of 40 nm, the DOS showed oscillatory behavior near the Fermi energy, with a peak-peak separation of about 50 meV (Fig. 5.4). More pulses were applied to cut the tube to even smaller pieces. *dI/dV* spectra

on a 16 nm piece (Fig. 5.4, top curve) also showed clear oscillations, with a peak-peak separation of about 160 meV. These values correspond reasonably well with the predicted energy level separation: the theoretical ΔE_L is 50 meV for $L = 40$ nm and 120 meV for $L = 16$ nm.

5.3.2 Spatially resolved spectroscopy

Nanotube ends

By measuring dI/dV as a function of position in the length direction of a nanotube, the evolution of the DOS near special sites such as nanotube ends can be observed. The straight dotted line drawn in Fig. 5.1d crossing the end of a nanotube is an example of such a measurement.
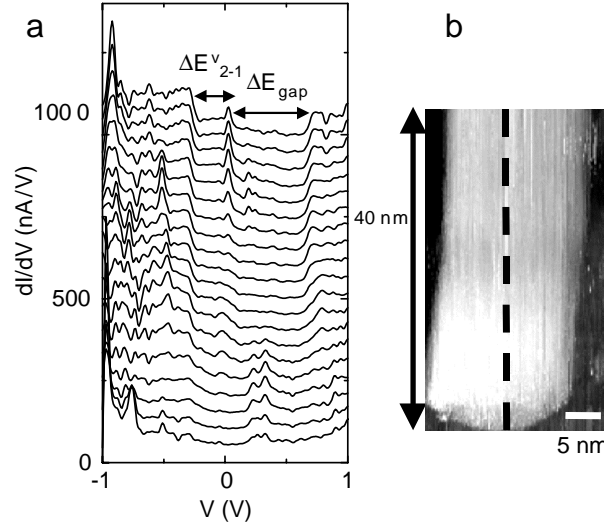
Figure 5.5: Electronic structure of the end of a semiconducting nanotube. a) dI/dV spectra measured at positions 2 nm apart along the dashed line shown in b. The energy gap ΔE_{gap} and the subband interval ΔE_{2-1}^v are indicated in the top curve. From top to bottom, the band structure gradually fades out and conductance peaks arise at the end. b) Topographic image of the nanotube end taken at a bias voltage of 0.4 V.

Figure 5.5a displays a series of curves, measured on a semiconducting nanotube, each about 2 nm apart along the dashed line indicated in the topographic image of Fig. 5.5b. The curves are offset vertically to show the gradual change of the tunneling DOS along the tube near the end. Starting form the top, the band structure can be well observed and is reproducible for adjacent curves. The energy gap ΔE_{gap} and the first subband separation ΔE_{2-1}^v are indicated for the top curves. Near the tube end, the subband edges fade out and two new peaks

appear within the energy gap at about 0.3 V. These peaks also fade out again in the last two curves where the STM moves off the tube end and onto the gold substrate. In the topographic image of Fig. 5.5b, which is obtained at a bias voltage of 0.4 V, the nanotube appears brighter near the end. This corresponds to the observed higher local density of states within the energy gap in the last ~ 10 nm.
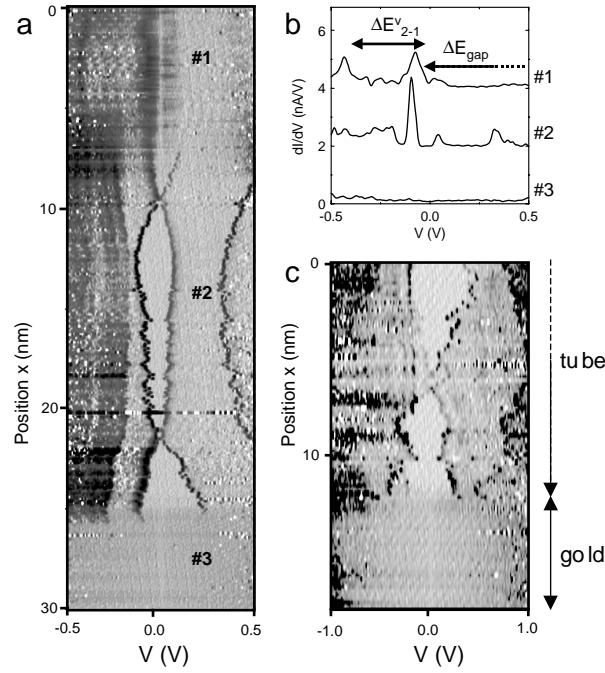
Figure 5.6: Tunneling conductance measured as a function of both the bias voltage and the position along ends of semiconducting nanotubes. a) dI/dV in grayscale plotted against the voltage V and position x along a nanotube length axis. Dark colors correspond to large tunneling conductance. In the bulk of the nanotube ($x < 8$ nm), the STM tip is far away from the end and the local DOS is similar to the semiconducting band structure. For $x > 8$ nm sharp peaks arise in the dI/dV that fluctuate in energy as a function of position. At the last few nm, ($x > 25$ nm) the STM tip is off the tube. b) dI/dV curves that are taken from horizontal cross-sections in a) indicated with the numbers #1, #2 and #3. c) dI/dV in grascale versus V and x for another semiconducting nanotube end. The tip is off the tube at the last few nm, where $x > 13$ nm.

A very illustrative way of presenting the spatially resolved data is to plot dI/dV in grayscale as a function of both the voltage V and the position x along the nanotube. Such a grayscale graph is shown in Fig. 5.6a for a spectroscopy

measurement on another semiconducting nanotube. dI/dV curves are obtained about 0.15 nm apart along a line of 30 nm. At the top, where $x = 0$, the STM tip is far away from the end. After about 25 nm, the tip moves off the tube and onto the gold. A dark color in this graph corresponds to a high tunneling conductance. Figure 5.6b shows a few dI/dV curves taken from horizontal cross-sections in Fig. 5.6a, at the positions #1, #2 and #3 that are indicated in the grayscale graph. The dI/dV spectrum measured far away from the tube end, curve #1, indicates that this nanotube is semiconducting. The energy gap is not completely visible due to the finite ± 0.5 V voltage window, but the strong rise in dI/dV near zero bias corresponds to the onset of the first valence subband observed for all semiconducting curves. The zero bias anomaly can be clearly observed in the grayscale graph, as the light-gray vertical stripe at 0 V for $0 < x < 8$ nm. The most striking feature is the fading out of the band structure at $x \approx 8$ nm and the appearance of three sharp peaks that show an oscillating behavior. These three dI/dV peaks can for example also be seen in curve #2. In the bottom few nm, for $x > 25$ nm, the STM tip actually measures dI/dV on the gold substrate. The tunneling conductance here is indeed featureless (curve #3). Measurements on the same nanotube, taken several minutes later showed that the oscillating pattern of dI/dV peaks is highly reproducible. Between measurements, voltage pulses were applied to the STM tip, away from the nanotube, to change the shape of the tip apex. Since this did not change the observed behavior in the nanotube we can exclude artefacts due to the microscopic shape of the tip. The remarkable behavior of oscillating peaks has also been observed on other semiconducting nanotubes. An example is shown in Fig. 5.6c for a semiconducting nanotube. Again, sharp peaks are observed that fluctuate along the tube.

We have no good understanding of all the observed features in dI/dV at the nanotube ends. It would be useful to know the geometry of the ends, for example whether they are closed or open. The single-walled nanotubes are assumed to be closed by caps during the growth, but it is difficult to confirm this by imaging because of the bluntness of the STM tip. In fact, STM spectroscopy can in principle be used to identify the nanotube ends [9, 36] as has been done by Carrol *et al.* [9] and Kim *et al.* [14]. They measured sharp resonances in the tunneling conductance at the last few nm at the end of nanotubes and identified these as localize states corresponding to a specific arrangement of pentagons at the end. In our case, sharp peaks also appear but they are found to oscillate in energy position over a large distance, 10-20 nm, which can not be explained by the presence of localized defects alone. Possibly, the gradually changing capacitance between the STM tip and nanotube when the tip scans over the end has to be taken into account. Simulations [37] show that the capacitance between the tube

and tip changes at the end over a length scale corresponding to the tip size. Our STM tips are typically 10-20 nm, which is also the scale over which the fluctuation patterns are observed. However, when the tip is displaced a few nm, the change in capacitance should be of the order of a few 10^{-3} aF, which can not explain the large energy fluctuations of about 0.1 eV within that distance.

Nanotube kink
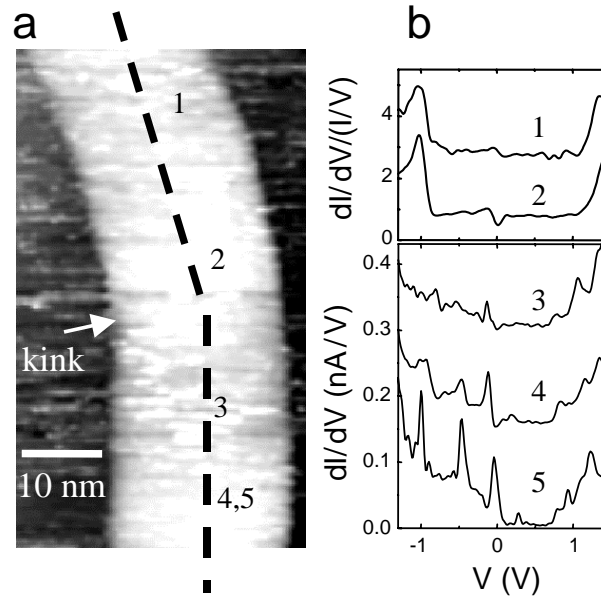
Figure 5.7: Topography and spectroscopy measurements on a nanotube kink that appears to be a semiconductor-metal junction. a) Topographic image of the nanotube kink. The bend angle is 17°. Numbers $1-5$ indicate positions where spectroscopy measurements were done. b) dI/dV and normalized dI/dV curves measured at positions $1-5$. These curves indicate metallic behavior of the top part (1,2) and semiconducting behavior of the bottom part $(3-5)$.

As discussed in section 5.2, nanotubes are often continuously bent due to elastic deformations. However, sharp bends or 'kinks' may also appear due to junctions between two nanotubes with different (n, m) indices. Such junctions can be possible when pentagon-heptagon defect pairs are present in the hexagonal carbon network [38, 39, 40]. In principle, nanotubes with a different electronic character can be connected to each other by such kinks, which is of interest for nanoscale electronics. Nanotube kinks have indeed been observed by TEM [41, 42] and AFM [43] imaging. A recent report of the electronic conductance of nanotube kinks provided evidence for the existence of semiconductor-metal

and metal-metal heterojunctions [43]. Kink-like sharp bends are occasionally observed in STM topographic images (for example Fig. 5.1c). Figure 5.7a shows a zoomed image of such a sharply bent nanotube. At various positions, indicated by the numbers $1 - 5$, STS measurements were done. The tunnel spectra above the kink are metallic (curve 1 and 2 in Fig. 5.7b) whereas below the kink they are semiconducting (curves $3 - 5$). This result strongly suggests that the kink is a heterojunction between a semiconducting and metallic nanotube.

5.4   Summary

In this paper we surveyed various measurements of the tunneling DOS in single-walled carbon nanotubes on Au(111). From dI/dV tunnel spectra all nanotubes that showed various chiralities could be classified as either metallic or semiconducting, with energy subband separations that compare well to the theoretical predictions. Discrete energy levels could be measured in the local DOS at low energies for a short metallic nanotube. The measured DOS curves are positioned asymmetrically around zero bias, indicating a shift of the Fermi level towards lower energies. This can be attributed to the difference in work function between the nanotubes and the gold substrate.

Spatially resolved measurements are used to observe changes in the local DOS at interesting topological sites such as nanotube ends and kinks. Measurements on semiconducting tube ends show that sharp conductance peaks appear within the energy gap which fluctuate in energy with position along the nanotube axis in a reproducible pattern. We do not yet have an explanation for all the experimental facts. We obtained also spectroscopy data on a nanotube kink that appears to be a molecular semiconducting-metal heterojunction. These measurements show that spatially resolved STM spectroscopy can be a useful technique to study the electronic structure of carbon nanotubes and may be exploited further to characterize nanotube devices such as kink heterojunctions.

References

[1] C. Dekker, Physics Today **52**, 22-28 (1999).

[2] J.W. Mintmire, B.I. Dunlap and C.T. White, Phys. Rev. Lett. **68**, 631 (1992).

[3] N. Hamada, S. Sawada and A. Oshiyama, Phys. Rev. Lett. **68**, 1579 (1992).

[4] R. Saito, M. Fujita, G. Dresselhaus and M. S. Dresselhaus, Appl. Phys. Lett. **60**, 2204 (1992).

[5] Z. Zhang and C.M. Lieber, Appl. Phys. Lett. **62**, 2792 (1993).

[6] M. Ge and K. Sattler, Appl. Phys. Lett. **65**, 2284 (1994).

[7] C. Olkand and J. Heremans, J. Mater. Res. **9**, 259 (1994).

[8] W. Rivera, J.M. Perez, R.S. Ruoff, D.C. Lorents, R. Malhorta, S. Lim, Y.G. Rho, E.G. Jacobs and R.F. Pinizzotta, J. Vac. Sci. & Techn. B **13**, 327 (1995).

[9] D.J. Carrol, P. Redlich, P.M. Ajayan, J.C. Charlier, X. Blase, A. de Vita and R. Car, Phys. Rev. Lett. **78**, 2811 (1997).

[10] J.W.G. Wildöer, L.C. Venema, A.G. Rinzler, R.E. Smalley and C. Dekker, Nature **391**, 59 (1998).

[11] T. Odom, J.-L. Huang, P. Kim and C.M. Lieber, Nature **391**, 62 (1998).

[12] W. Clauss, D.J. Bergeron and A.T. Johnson, Phys. Rev. B **58**, R4266 (1998).

[13] A. Hassanien, M. Tokumoto, Y. Kumazawa, H. Kataura, Y. Maniwa, S. Suzuki and Y. Achiba, Appl. Phys. Lett. **73**, 3839 (1998).

[14] P. Kim T. Odom, J.-L. Huang and C.M. Lieber, Phys. Rev. Lett. **82**, 1225 (1999).

[15] C. T. White and J.W. Mintmire, Nature **394**, 29 (1998).

[16] J.-C. Charlier and Ph. Lambin, Phys. Rev. B **57**, R15037 (1998).

[17] A. Thess, R. Lee, P. Nikolaev, H. Dai, P. Petit, J. Robert, C. Xu, Y.H. Lee, S.G. Kim, A.G. Rinzler, D.T. Colbert, G.E. Scuseria, D. Tománek, J.E. Fischer and R.E. Smalley, Science **273**, 483 (1996).

[18] T. Hertel, R.E. Walkup and Ph. Avouris, Phys. Rev. B **58**, 13870 (1998).

[19] A. Rubio, Appl. Phys. A **68**, 275 (1999).

[20] V. Meunier and Ph. Lambin, Phys. Rev. Lett. **81**, 5888 (1998).

[21] L.C. Venema, V. Meunier, Ph. Lambin and C. Dekker, Phys. Rev. B **61**, 2991 (2000).

[22] G. Dresselhaus, M.A. Pimenta, R. Saito, J.C. Charlier, S.D.M. Brown, P. Corio, A. Marucci and M.S. Dresselhaus, in *Science and Application of Nanotubes*, edited by Tománek and Enbody, (Kluwer Academic / Plenum Publishers, New York, 2000) pp. 275-295.

[23] J.A. Stroscio and R.M. Feenstra, in *Scanning Tunneling Microscopy, Vol 27 of Methods in Experimental Physics*, edited by J.A. Stroscio and W.J. Kaiser (Academic Press Inc., San Diego, 1993), chapter 4 and references therein.

[24] P. Chen, X. Wu, S.J. Lin, W. Ji and K.L. Tan, Phys. Rev. Lett. **82**, 2548 (1999).

[25] H. Ago, T. Kugler, F. Cacialli, W.R. Salaneck, M.S.P. Shaffer, A.H. Windle and R.H. Friend, J. Phys. Chem. B **103**, 8116 (1999).

[26] Y. Xue and S. Datta, Phys. Rev. Lett. **83**, 4844 (1999).

[27] B.L. Altshuler and A.G. Aronov, Solid State Comm. **30**, 115 (1979).

[28] B.L. Altshuler, A.G. Aronov and P.A. Lee, Phys. Rev. Lett. **44**, 1288 (1980).

[29] G.-L. Ingold and Yu.V. Nazarov, in *Single Charge Tunneling, NATO ASI Series B, Vol 294*, edited by H. Grabert and M.H. Devoret (Plenum Press, New York and London, 1991), chapter 2.

[30] R. Egger and A. Gogolin, Phys. Rev. Lett. **397**, 5082 (1997).

[31] C. Kane, L. Balents and M.P.A. Fisher, Phys. Rev. Lett. **79**, 5086 (1997).

[32] S.J. Tans, M.H. Devoret, H. Dai, A. Thess, R.E. Smalley, L.J. Geerligs and C. Dekker, Nature **386**, 474 (1997).

[33] M. Bockrath, D.H. Cobden, P.L. McEuen, N.G. Chopra, A. Zettl, A. Thess and R.E. Smalley, Science **275**, 1922 (1997).

[34] L.C. Venema, J.W.G. Wildöer, J.W. Janssen, S.J. Tans, H.L.J. Temminck Tuinstra, L.P. Kouwenhoven and C. Dekker, Science **283**, 52 (1999).

[35] L.C. Venema, J.W.G. Wildöer, H.L.J. Temminck Tuinstra and C. Dekker, Appl. Phys. Lett. **71**, 2629 (1997).

[36] A. de Vita, J.-Ch. Charlier, X. Blase and R. Car, Appl. Phys. A **68**, 283 (1999).

[37] The program used for the capacitance simulations is FastCap, developed by the Research Laboratory of Electronics at MIT (1992).

[38] Ph. Lambin, A. Fonseca, J.P. Vigneron, J.B. Nagy and A.A. Lucas, Chem. Phys. Lett. **245**, 85 (1995).

[39] R. Saito, G. Dresselhaus and M.S. Dresselhaus, Phys. Rev. B, **53,** 2044 (1996).

[40] L. Chico, V.H. Crespi, L.X. Benedict, S.G. Louie and M.L. Cohen, Phys. Rev. Lett., **76**, 971 (1996).

[41] S. Iijima, T. Ichihashi and Y. Ando, Nature **356**, 776 (1992).

[42] J. Han, M.P. Anantram, R.L. Jaffe, J. Kong and H. Dai, Phys. Rev. B **57**, 14983 (1998).

[43] Z. Yao, H.W.Ch. Postma, L. Balents and C. Dekker, Nature **402**, 273 (1999).

Chapter 6

Scanning tunneling spectroscopy on a carbon nanotube buckle

J.W. Janssen, S.G. Lemay, M. van den Hout, M. Mooij,
L. P. Kouwenhoven and C. Dekker

The topography and electronic structure of a semiconducting carbon nanotube with a sharp bend is studied by scanning tunneling microscopy and spectroscopy. From the increased height it is concluded that the nanotube is 'buckled', i.e. collapsed due to very strong bending. Detailed spatially resolved spectroscopy measurements at the location of the buckle reveal a well-defined localized state inside the semiconducting gap. The spatial extent of this localized state is about 2 nanometers.

6.1   Introduction

Nanotubes are molecular wires that reveal new interesting physical phenomena typical for one dimensional systems [1]. Transport and scanning tunneling microscopy measurements have revealed many of the bulk electronic properties of carbon nanotubes. Attention is now turning towards localized structures such as kinks and bends within tubes.

Two nanotubes with different chirality can be connected together seamlessly by a pentagon-heptagon pair, as is predicted by Lambin *et al.* [2] and Chico *et al.* [3]. This leads to a kink-like structure within that nanotube. Diode behavior has been measured through a kink connecting a metallic and a semiconducting tube [4]. Recently scanning tunneling microscopy (STM) and spectroscopy (STS) measurements on kinks showed that a metallic tube and a semiconducting tube can indeed be connected together [5, 6].

Applying mechanical force on a nanotube can create a bend within that nanotube [7]. If the strain in the tube exceeds a critical limit, the elastically bent nanotube deforms into a buckle [8], a severe distortion of the atomic structure where all the strain is concentrated locally. The buckle is associated with a rearrangement of atoms and bonds which will have a large impact on the band structure in the region of the buckle and thus on the electronic properties of the tube [8, 9]. Buckles made by AFM manipulation were shown to behave as tunnel barriers in transport studies [7]. Here, we present the first detailed spatially resolved spectroscopy on a buckle. We show that this buckle strongly affects the local electronic structure.

6.2   Experimental details

As a substrate for our STM studies we use gold (111) facets, which form after flame annealing a small (15 mm^3) piece of 99.99% pure gold. Gas-phase catalytically grown carbon nanotubes [10] are dispersed in dichloroethane by sonication. Small droplets are deposited on the facets resulting in mainly individual carbon nanotubes on the atomically flat surface. Such a sample is cooled down in an Omicron low-temperature STM that is operated at 4.6 K. At low temperature there is no movement of the tip with respect to the sample due to thermal drift. This is important as it allows time-consuming spatially resolved spectroscopy measurements. As a tip we use a 0.25 mm diameter 90%Pt/10%Ir wire which is cut in ambient with cleaned scissors.

During sonication, or when the tubes are deposited on the substrate, mechanical forces can induce strain into a nanotube, which can lead to the formation of bends or even buckles. Once in contact with the substrate the adhesion force, caused by the van der Waals interaction between the tube and the substrate, may be sufficiently strong to lock this deformation. A bend or buckle can thus remain stable on the substrate. In our measurements we frequently observe slightly curved tubes, i.e., bends with very low angles. Occasionally we observe sharper angles such as the one presented here. Figure 6.1a shows a topography map of such a sharply bent tube with a bend angle of 26° or 0.45 rad.

6.3   Buckle or kink?

We need to distinguish whether the local bend of Fig. 6.1 corresponds to a buckle formed by mechanical strain, or a kink connecting tubes with different diameter and chirality. Spectroscopy measurements performed far away from the bend,
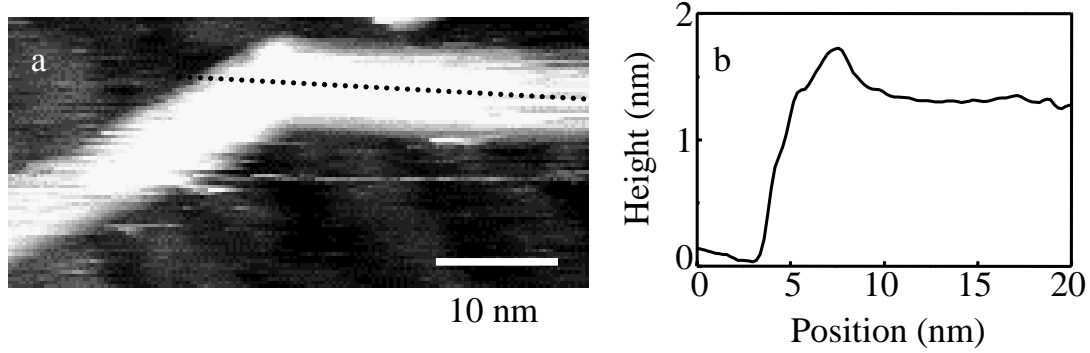
Figure 6.1: a) STM constant current image of a sharply bent individual single-walled carbon nanotube. This image was obtained at a sample bias voltage of $V = -1$ V and a feedback current of $I = 20$ pA. b) Height profile over the bend along the dotted line in a. At the location of the bend, the nanotube height of 1.4 nm is increased up to 1.8 nm.

to be discussed in further detail below, shows identical semiconducting behavior on both sides of the tube. In addition, the local height at the bent region is clearly higher, as can be seen in Fig. 6.1b. The tube has a height of 1.4 nm which increases up to 1.8 nm near the bend. Note that a small distance of 0.2 nm between tube and substrate is included in this height due to van der Waals interaction. For a nanotube kink, no height increase is expected. By contrast, in the case of buckled tube, the tube cylinder is pressed ('squashed') together and the height can theoretically increase up to $\pi d/2$, were d is the diameter of the tube. For a tube with a diameter of 1.2 nm this upper bound for the height increase due to a buckle is 1.9 nm. Iijima *et al.* derived an equation for the critical curvature for a buckle to form [8]. For a tube of 1.2 nm in diameter the expected degree of bending necessary to form a buckle is 0.10 rad/nm. Determining the exact radius of curvature of the tube is difficult because the image is broadened by convolution with the shape of the tip. From the height profile we know that the tube has a diameter of 1.2 nm while it appears laterally as broad as 5 nm. The tip convolution thus is of the order of 4 nm. As an upper bound we find that the bend is at least localized within the width of the tip since the observed angle is very sharp. This puts a lower limit of 0.11 rad/nm on the curvature.

We conclude that indeed a buckle is formed but the tube may not be completely pressed together since the height does not increase up to its theoretical maximum. To date we have studied only one buckle. Note that the apparent height change can in principal also be caused by a change in the local density of states (LDOS). However, we can rule this out since the profile shown here is taken at a bias voltage of -1 Volt, were the LDOS does not change. Therefore we

conclude that the height change is solely due to a topological buckle deformation.

6.4   Spectroscopy over the buckle

We have performed one dimensional (1D) line scans, measuring the change in the electronic structure as a function of position on the tube. At every point $I(V)$ is measured. The derivative $dI/dV(V)$ is taken numerically and plotted in grayscale in Fig. 6.2. The grayscale indicates the magnitude of the differential conductance dI/dV, which is a measure of the local density of states (LDOS), as a function of the bias voltage over the tip-tube junction. White is high DOS and black is zero DOS. The horizontal axis is the position on the tube as indicated by the dotted lines in the top illustration of Fig. 6.2. The semiconducting gap is clearly visible as a dark band. The onsets of the first van Hove singularities show up in white. The spectroscopy is featureless along the tube away from the buckle except for small fluctuations in energy. Such fluctuations are also observed in straight tubes [11]. However, at the position of the buckle a clear localized state is visible inside the gap.
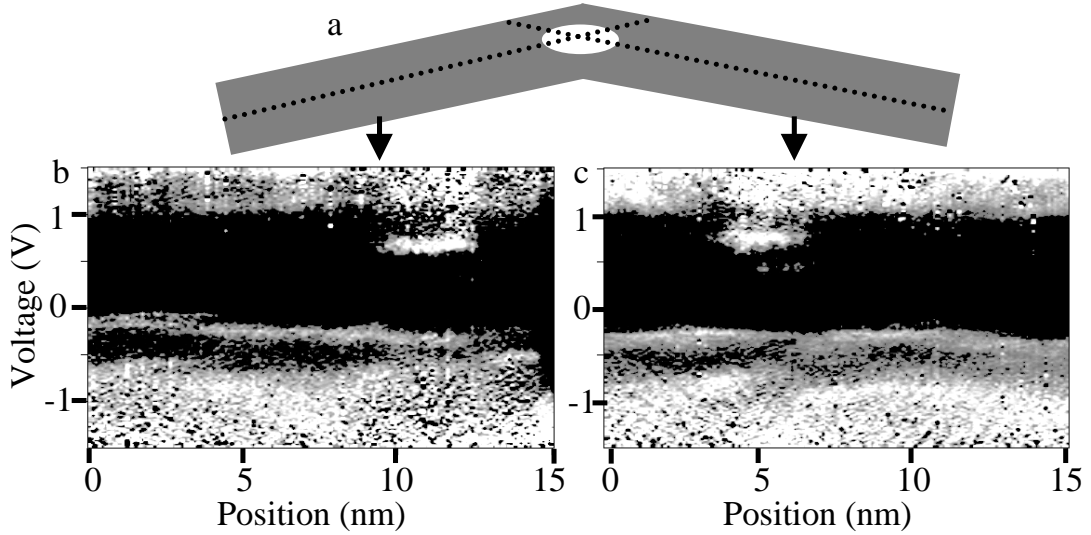
Figure 6.2: a) Schematic drawing of the buckle. The two dotted lines indicate the tip position for the two spectroscopy plots given at the bottom figures. b,c) Grayscale plots of dI/dV as a function of voltage (y-axis) and position along the tube (x-axis). At the position of the buckle, a localized state within the semiconducting gap is clearly visible.
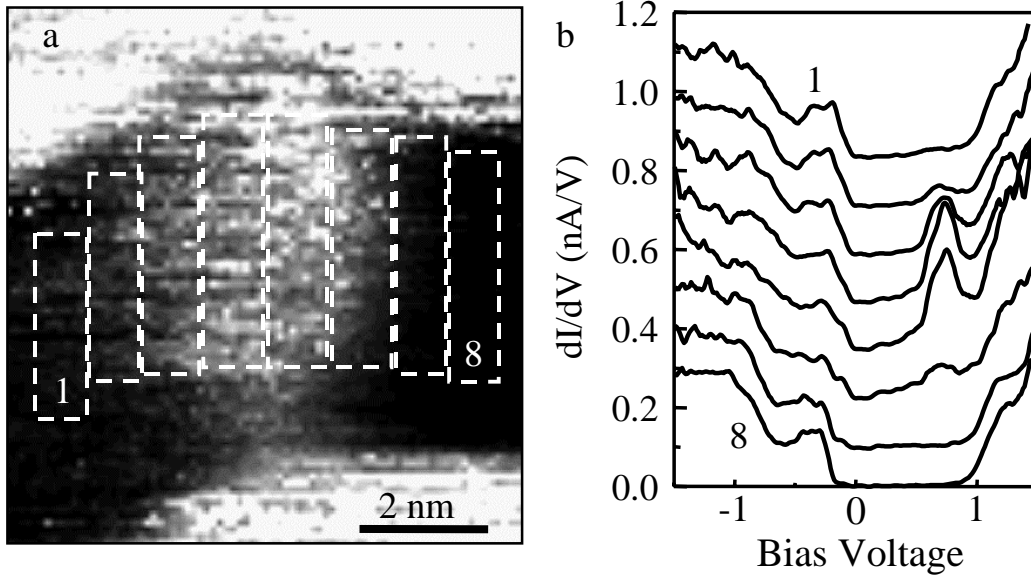
Figure 6.3: a) STM current image in grayscale at +0.72 V of 8×8 nm^2. White is a high current, black is a low current. The semiconducting gap shows up as black. The gold around the tube is white since a current can flow also at low bias. b) Curves 1 to 8 are averaged over the regions indicated in a, starting from the left of the localized state moving gradually to the right. The gap is visible as the flat part with an essentially zero DOS. The curves in (b) are offset vertically by 0.1 nA/V for clarity.

From spectroscopy measurements over a grid of points on top of the buckle we can gain more insight in the spatial and electronic structure of the localized state. Figure 6.3a shows a measurement of a current image of the localized state at a bias voltage of 0.72 Volt. Tip convolution broadens the state in the transverse direction but along the tube we can measure the extent of the state away from the buckle. We find that the state extends 2 nm in either direction from the buckle. Figure 6.3b shows spectroscopy curves averaged over the indicated regions in Fig. 6.3a. The localized state is quite well defined with a full width at half maximum of 0.3 V. Away from the buckle the semiconducting gap is essentially flat. Upon moving over the buckle the sharp localized state appears and decays symmetrically.

6.5 Discussion

Several calculations of the electronic structure of kinks and buckles have been reported. However, there are no calculations of the LDOS versus position for this particular measurement layout. We therefore limit ourselves to a qualitative

comparison with related cases. Chico *et al.* showed that defect states appear inside the gap at the interface between two semiconducting tubes connected by topological kink defect [3]. The states fall off within a few unit cells, i.e. within 1 nm. Here, we measured a buckle and not a kink but we believe that the spatial extent of the defect states is expected to be comparable.

Rochefort *et al.* calculated the effect on the electronic structure caused by bending a metallic nanotube [9]. No significant change was observed for moderate curvature but once a buckle is formed, charge accumulates in the buckled region and additional states appear in between the first van Hove singularities. The states were attributed to a mixing of π and σ states. Since the mixed states have a more local character than pure π states, the transmission through the tube is lower, resulting in an increased resistance. This is consistent with the experimental observation that buckles behave as tunnel contacts [7]. Although we have measured a semiconducting buckle, the observation of a localized state is qualitatively consistent with this prediction. A theoretical calculation of the LDOS over a buckle in a semiconducting tube is desirable.

6.6   Conclusion

We have shown the first spectroscopy measurements on a nanotube buckle. The formation of a buckle leads to an extra peak within the semiconducting gap. The spatial extent of 2 nm of the localized state agrees with theoretical predictions.

References

[1] C. Dekker, Physics Today **52**, 22 (1999).

[2] Ph. Lambin, A. Fonseca, J.P. Vigneron, J.B. Nagy and A.A. Lucas, Chem. Phys. Letters **245**, 85 (1995).

[3] L. Chico, V.H. Crespi, L.X. Benedicht, S.G. Louie and M.L. Cohen, Phys. Rev. Lett. **76**, 971 (1996).

[4] Z. Yao, H.W.Ch. Postma, L. Balents and C. Dekker, Nature **402**, 273 (1999).

[5] M. Ouyang, J.L. Huang, C.L. Cheung and C.M. Lieber, Science **291**, 97 (2001).

[6] L.C. Venema, J.W. Janssen, M.R. Buitelaar, J.W.G. Wildöer, S.G. Lemay, L.P. Kouwenhoven and C. Dekker, Phys. Rev. B **62**, 5238 (2000).

[7] H.W.Ch. Postma, M. de Jonge, Z. Yao and C. Dekker, Phys. Rev. B **62**, 10653 (2000).

[8] S. Iijima, C. Brabec, A. Maiti and J. Bernholc, J. of Chem. Phys. **104**, 2089 (1996).

[9] A. Rochefort, Ph. Avouris, F. Lesage and D.R. Salahub, Phys. Rev. B **60**, 13824 (1999).

[10] P. Nikolaev, J.M. Bronikowski, R. Kelley Bradley, F. Rohmund, D.T. Colbert, K.A. Smith and R.E. Smalley, Chem. Phys. Lett. **313**, 91 (1999).

[11] J.W. Janssen, S.G. Lemay, L.P. Kouwenhoven and C. Dekker, unpublished results.

Chapter 7

Scanning tunneling spectroscopy on crossed carbon nanotubes

J.W. Janssen, S.G. Lemay, L.P. Kouwenhoven and C. Dekker

Crossing nanotubes were investigated using scanning tunneling microscopy and spectroscopy. From the analysis of the measured mechanical deformation of the nanotubes, the contact force between the nanotubes is estimated to be 1 nN. Spectroscopy measurements showed two effects on the electronic structure: (i) band bending, which we attribute to a position-dependent interaction with the substrate, and (ii) the formation of localized states, as signaled by additional peaks in the density of states at the crossing point. The existence of localized states at the junction represents a much stronger perturbation of the electronic structure than has generally been assumed. The relevance of these STM results for the interpretation of transport measurements is discussed.

7.1 Introduction

Since carbon nanotube molecules have been electrically contacted [1, 2] a variety of single nanotube electronic devices has been fabricated. These include devices based on individual single-wall carbon nanotube (SWNT) such as field-effect transistors [3, 4], single-electron transistors [5] and diodes [6]. More complex arrangements involving more than one SWNT have also been fabricated recently using AFM manipulation [7], and crossed nanotube junctions have been contacted to produce multi-terminal nanotube devices [8].

Such nanotube junctions are the subject of this article. From transport measurements, Fuhrer *et al.* proposed that nanotube junctions can exhibit two different types of behavior [8]. The behavior of a crossing between two metallic or

two semiconducting tubes was interpreted as a conventional tunnel contact at the junction. The behavior of a crossing between a metallic and a semiconducting SWNT was instead interpreted as a Schottky barrier combined with a tunnel contact. Both these and other measurements [7] could be explained by assuming that the bulk electronic properties of each nanotube were not severely affected by the presence of the junction. The validity of this assumption is difficult to ascertain by transport measurements, however, since the latter provide only indirect information about the local electronic structure near the junction.

Scanning tunneling microscopy (STM) and spectroscopy (STS) are ideally suitable to tackle this problem. On carbon nanotubes, STM and STS have confirmed the relation between the atomic structure and the electronic properties [9, 10]. More recently, the effect of strong bends (buckles) [11] and kink-like topological defects [12] have been studied. Here we use STM to study nanotube crossings. We estimate the force between the nanotubes and their binding energy to a supporting gold substrate. More importantly, our STS studies show that the local electronic structure can be severely distorted due to the crossing. We observe two effects on the electronic structure: (i) band bending, which we attribute to a position-dependent interaction with the substrate, and (ii) localized states, as signaled by additional peaks in the density of states at the crossing point. The existence of localized states at the junction represents a much stronger perturbation of the electronic structure than has generally been assumed, and is highly relevant for the interpretation of transport measurements.

The outline of this article is as follows. We first present the topographic images of crossed carbon nanotubes. Using a simple continuum model we estimate the force between the tubes from these topographic images, and compare this with results from theoretical calculations. The results of STS measurements are then presented and their implications are discussed.

7.2   Topography results

Single-wall carbon nanotubes (SWNT) were produced using laser evaporation by the group of R.E. Smalley at Rice University, USA. A small amount of the raw material was ultrasonically dispersed in dichloroethane. A few droplets were deposited on gold (111) facets, which were formed by flame annealing a small (15 mm^3) piece of 99.99% pure gold. This procedure results in (mainly individual) carbon nanotubes on an atomically flat surface. Such a sample was cooled down in a home-built 4 K STM [13] and scanned with 90%Pt/10%Ir tips cut under ambient conditions. Nanotubes crossing other nanotubes were regularly found.
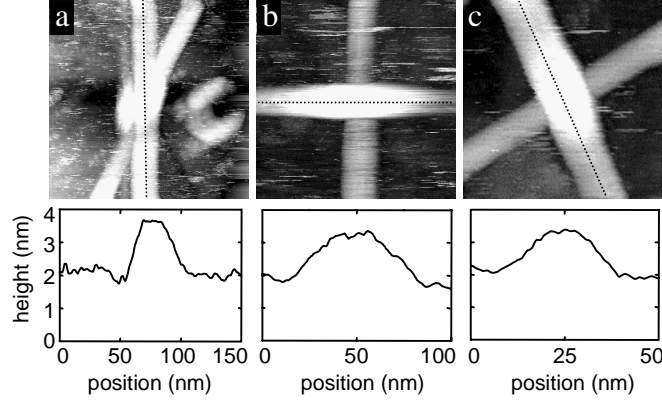
Figure 7.1: Topographic images of three crossings between pairs of individual SWNTs. These images were obtained using a feedback current of 20 pA at a sample voltage of -1 V. The height profile along the dotted line in each image is plotted below the image. The gold substrate is taken as reference height.

Eight of these crossings have been studied in detail. Three typical examples are shown in Fig. 7.1. All three topographs were obtained using a sample bias voltage of -1 V and a feedback current of 20 pA. The two tubes in Fig. 7.1a cross at a 26° angle, while those in Figs. 7.1b and 7.1c cross at 90° angles. The diameter of these SWNTs is ∼ 1.5 nm, as determined from height measurements. The nanotubes can appear up to 15 nm in width in the images due to tip convolution.

Height profiles along the longitudinal axis of the uppermost tube are shown below each image in Fig. 7.1. These plots show that a tube crossing another tube does not closely follow the height profile of the obstacle. The deformations associated with the crossings instead occur over lengths of 40 nm in Fig. 7.1a, 60 nm in Fig. 7.1b and 35 nm in Fig. 7.1c. The height profiles are thus smooth on a length scale much longer than the diameter of the underlying SWNT and the size of the STM tip. This reflects the intrinsic stiffness of the SWNTs.

The top tube in Fig. 7.1a (b,c) has a diameter of 1.6 (1.5, 1.7) nm. Here 0.3 nm was subtracted from the topographic height to account for the van der Waals distance [14]. These values are in good agreement with values for the diameter deduced from spectroscopy measurements [15]. In Fig. 7.1a (b,c) the underlying tube is 1.7 (1.5, 1.4) nm in diameter. The total height of the crossing is 3.2 (2.9, 3.0) nm and is thus lower by 20-23% than the sum of the diameters of both tubes plus the van der Waals distances. This indicates that a certain amount of mechanical deformation ('squashing') of the nanotubes exists at the crossings. From the smoothness of the height profiles at the junction, we can however exclude the presence of local buckles at the crossing.

7.3   Determination of the contact force

In this section we discuss how the contact force between the nanotubes at the crossing can be calculated from the measured height profiles. The magnitude of this force provides a quantitative measure of the strength of the interaction between the nanotubes and of the deformation of the nanotubes at the crossing. It also allows for comparison with theoretical calculations which additionally assess the impact of the crossing on the tubes' electronic interaction. We calculate the contact force using a simple continuum model, similar to models used in discussions of the mechanical properties of carbon nanotubes [16, 17].

A nanotube on a gold substrate feels an attractive force from the substrate due to the van der Waals interaction. When a nanotube crosses another nanotube (or other obstacle) the upper nanotube deforms elastically by slightly bending over the lower nanotube. This induces strain in the upper nanotube, resulting in a normal contact force between the nanotubes. The situation is similar to the model of a centrally loaded cylinder with fixed ends [18].

The force exerted at the area of contact is given in this case by $F = 192EIh/l^3$, where E is the Young's modulus, I the second moment of area, h the central deflection of the upper tube and l the length over which the tube is bent or deformed. Values for both h and l can be obtained from the height profiles in Fig. 7.1. The Young's modulus of an individual SWNT has previously been estimated to have the value $E = 1.3 \pm 0.4$ TPa from deflection measurements on multiwall nanotubes (MWNT) and ropes of SWNTs [16]. A SWNT can be approximated as a hollow cylinder with a second moment of area $I = \frac{\pi}{4}(r_{outer}^4 - r_{inner}^4)$. Here r_{outer} and r_{inner} are the outer and inner radius, respectively. They can be estimated from the measured diameter using 0.3 nm as the wall thickness for an individual tube [14]. Typical values for our junctions are $r_{outer} = 0.9 \pm 0.1$ nm and $r_{inner} = 0.6 \pm 0.1$ nm, $h = 1.5 \pm 0.1$ nm and $l = 50 \pm 5$ nm. This yields a force ranging from 0.6 nN to 1.2 nN for different junctions, with a typical uncertainty of 0.3 nN for each case. For comparison, the force exerted by the STM tip is estimated not to exceed 0.05 nN for the scan parameters used [19]. As this force is significantly smaller than the intertube force of ~ 1 nN, we neglect effects from tip forces.

The estimated contact force of 1 nN can be compared to theoretical calculations. In Ref. [17] it was argued, based on continuum and molecular mechanics simulations, that two crossing $(10, 10)$ tubes on a graphite surface exhibit a contact force of 5 nN. This is of the same order of magnitude as our experimental results, which were obtained for tubes with diameters similar to a $(10, 10)$ tube. In the simulations, the force pressing the two tubes together reduces the total height of the crossing by 20%. This fits very well with our observation of 20%-23%

height reduction.

The *inter*tube conductance at crossings with a geometry very similar to that studied here was measured by Fuhrer *et al.* [8] to be as high as 0.2 e^2/h. This corresponds to 10% of the value for perfect transmission, 2e^2/h. The dependence of the conductance between two crossing (5,5) nanotubes on the contact force was investigated in calculations by Yoon *et al.* [20], and a strong dependence on the contact force was found. For a contact force of 1 to 2 nN (corresponding to our experimentally determined force), a low intertube conductance (< 0.05e^2/h) was predicted. The experimental results by Fuhrer *et al.* were best explained by contact forces of 10 to 15 nN. At such high contact forces it was calculated that there is a significant mechanical deformation of the nanotubes resulting in an enhancement of the wave function overlap between the nanotubes. It was further concluded that the *intra*tube conductance is, however, only weakly affected by the presence of the crossing. We will return to these calculations in the discussion section.

Analysis of the height profile can also be used to estimate the binding energy of nanotubes on gold using the method of Hertel *et al.* [21]. Briefly, this involves balancing the cost of elastically bending the nanotube and the gain in binding energy to the substrate. The binding energy is obtained by integrating $\frac{1}{8}E\pi(r_{outer}^4 - r_{inner}^4)\int \rho(x)^{-2}dx$ along the longitudinal axis of the tube. Here $\rho(x)$ is the local radius of curvature. Our profiles are well fitted by a circle with a typical radius of ~ 100 nm. We then obtain a binding energy of 0.8 ± 0.2 eV/Å. The results for different crossings range from 0.5 to 1.2 eV/Å. A similar binding energy of 0.8 ± 0.3 eV/Å was obtained by Hertel *et al.* for MWNT on hydrogen-passivated silicon [21].

7.4 Spectroscopy results

We now turn to the effect of a crossing on the electronic structure of the SWNTs. We have performed STS measurements on the upper nanotube as a function of position for a number of crossings. In STS, the STM tip is held at a fixed distance from the sample and the differential tunnel conductance dI/dV is measured as a function of tip-sample bias V. It can be shown that $dI/dV(V)$ is approximately proportional to the density of states (DOS) at energy eV [22]. Such measurements were repeated on a series of equally spaced positions along the length axis of the tube with sub-ångstrom resolution. We find that a crossing can have two different effects on the local electronic structure in a carbon nanotube, viz., band bending (i.e. spatially-dependent energy bands) and the formation of localized states.
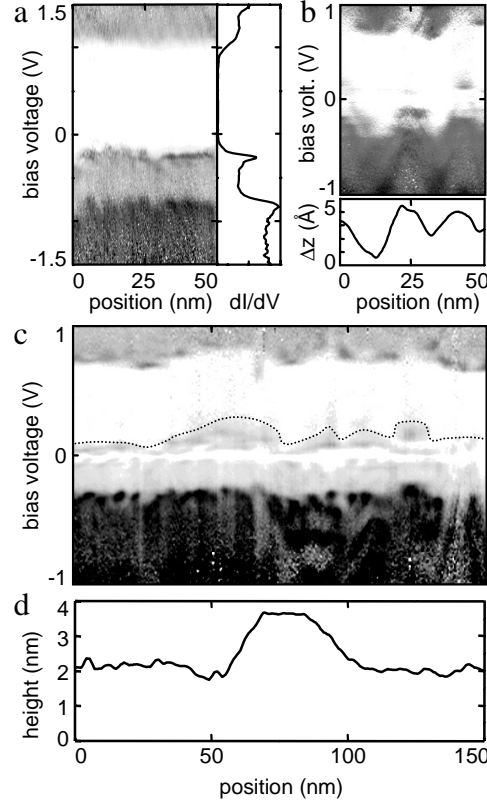
Figure 7.2: a) The differential conductance dI/dV for a semiconducting tube lying on an atomically flat gold substrate shown as a function of sample voltage (y-axis) and position along the nanotube (x-axis). The grayscale indicates the magnitude of dI/dV: white corresponds to 0 nA/V, black to 0.2 nA/V. A single $dI/dV(V)$ curve is also plotted on the right for reference. b) Grayscale plot of $dI/dV(V)$ as a function of position for a semiconducting SWNT lying on a granular platinum substrate. Black corresponds to 0.6 nA/V. The height profile along the nanotube is plotted below. c) Grayscale plot of $dI/dV(V)$ as a function of position for a semiconducting SWNT crossing another semiconducting SWNT (Fig. 7.1a). Black corresponds to 0.2 nA/V. The onset of the first van Hove singularity at the valence band edge is marked by a dotted line. Fluctuations of the energy of the valence and conduction band edges are highly correlated. d) Height versus position; the crossing is located at $x \approx 80$ nm.

For reference, we first discuss spectroscopy results on straight nanotubes lying on a gold or platinum substrate. Fig. 7.2a shows the DOS as a function of position for a semiconducting nanotube on atomically flat gold. dI/dV is plotted in grayscale as a function of position on the tube (x-axis) and sample voltage (y-axis). For clarity a single $dI/dV(V)$ curve is also shown on the right. The white area in the grayscale plot corresponds to the semiconducting gap and is bordered

by two van Hove singularities (vHs). A vHs marks the onset of a one-dimensional band in the carbon nanotube band structure. In this figure we observe the vHs for the conduction band at +1.0 V and for the valence band at -0.1 V. In the valence band, the second vHs is visible at -0.6 eV. The energies of the vHs are normally assumed to be independent of position. Figure 7.2a however exhibits small ($\sim$ 0.05 eV) variations in these energies, even in this simple case of a nanotube on an atomically flat surface. A more dramatic effect is evident in Fig. 7.2b, which shows the case of a tube lying on a platinum substrate. This surface is not atomically flat but instead consists of grains with a typical lateral size of 20 nm. The corrugation between the peaks and valleys of the grains is 1.5 to 2 nm. The height profile (plotted below the STS plot) shows that the corrugation on the nanotube is however only 0.5 nm. The nanotube thus does not follow the contour of the grains, but instead hangs in between grains at both $x \approx 13$ and $x \approx 32$ nm due to its stiffness. In the DOS(x) plot, a shift of the semiconducting gap towards negative energies is observed at these positions. We interpret this shift as a change in the amount of charge transfer between the nanotube and the substrate ('doping') due to variations in the strength of interaction with the substrate. Such band bending is also exploited in nanotube field-effect transistors [3].

Figure 7.2c shows STS measurements for a semiconducting nanotube crossing another semiconducting nanotube (see Fig. 7.1a). At the onset of the valence band a dotted line is plotted as a guide to the eye. The second vHs in the valence band is also visible. Following the position in energy of the vHs along the length of the tube, we observe energy fluctuations of about 0.25 eV. Similar fluctuations are also observed in the energy of the first vHs of the conduction band. The fluctuations in both valence and conductance band are strongly correlated, indicating local band bending. Since such large fluctuations are not normally observed for tubes lying flat on an Au(111) surface, we attribute them to the presence of the crossing. Accounting quantitatively for these fluctuations is difficult because several parameters are poorly known (eg. the amount of charge transfer at the nanotube-nanotube junction), and this will not be discussed further here.

In addition to band bending, crossings can exhibit more severe perturbations of the electronic structure, namely the formation of additional states. Figures 7.3a-c show STS data taken along a metallic tube crossing over a semiconducting tube (Fig. 7.1b). The central region in energy, with a width of $\sim$ 1.8 eV, is bordered by two van Hove singularities at about -0.8 eV and 1.0 eV, as shown in Fig. 7.3a [23].

The height profile over the junction is also plotted in Fig. 7.3d. At the top of the crossing, near $x = 50$ nm, two peaks in the DOS appear, as emphasized
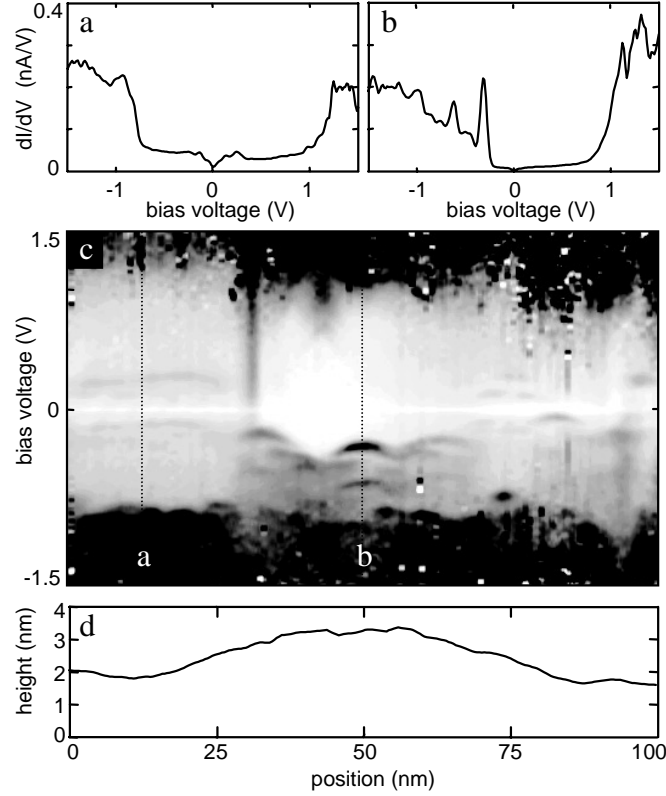
Figure 7.3: Differential conductance for a metallic SWNT crossing a semiconducting SWNT (Fig. 7.1b). a) Differential conductance dI/dV versus sample bias V far from the crossing. The DOS is finite around near the Fermi level, and van Hove singularities are observed at -0.8 and ~ 1.0 eV. b) $dI/dV(V)$ at the position of the crossing. Two additional peaks are visible at -0.3 and -0.6 eV, whereas the DOS in the pseudogap is suppressed between -0.2 and +0.3 eV. c) Grayscale plot of the differential conductance as a function of sample bias voltage (y-axis) and position along the metallic tube (x-axis). White corresponds to 0 nA/V, black to 0.2 nA/V. The dotted lines indicate the positions of the curves shown in (a) and (b). d) Height versus position; the crossing occurs at $x \approx 50$ nm.

in Fig. 7.3b. The black areas indicate an enhanced DOS at -0.3 eV and -0.6 eV. These states are highly localized near the crossing. At the same position we observe a reduction in the DOS at energies between -0.2 and 0.3 eV, which appears as a white region in Fig. 7.3c. These features are qualitatively consistent with Coulomb blockade for tunneling into a small island. An estimate for the size of such an island can be obtained from the energy spacing $\Delta E = 0.3$ eV between the two localized peaks. Using $L = hv_f/2\Delta E$, were h is Planck's constant and $v_f = 8.2 \times 10^7$ cm/s [24], we obtain $L = 6$ nm. This agrees well with the observed

extension of about 8 nm. Tip convolution does not have a big effect since the height change on top is small in the length direction of the nanotube.

Localized states can arise from severe topological distortions like buckles [25, 26], in which atomic bonds are rearranged. As discussed in section 7.2, however, such a distortion is unlikely to be present here. This strongly suggests that the interaction between the tubes at the crossing is responsible for the features observed.

7.5   Discussion and conclusions

The contact force that we determine experimentally would, according to calculations [20], result in a weak electrical contact between the nanotubes. These calculations suggested that backscattering due to the crossing is very weak and that the intratube conductance is only slightly reduced. We instead observe a severe distortion of the electronic structure even in the case of small forces and expect this to have a significant impact on backscattering. Direct comparison is however not possible since published simulations only provide information on the conductance, whereas our experiment only measures the local density of states.

The layout of our crossings is very similar to that used in transport measurements [7, 8], but the underlying substrates (SiO_2 for transport measurements and Au(111) for STM measurements) differ. Nonetheless, the binding energy between nanotube and substrate [21] and the height profile at the crossing [7] are comparable in the two cases. We therefore expect changes in the electronic structure induced by the crossing to also be comparable. The interpretation of the transport measurements has so far been based on tunneling between nanotubes whose bulk electronic properties are not affected by the crossing. We have shown here that the local electronic structure can instead be severely distorted, that is, that the bulk electronic properties can be strongly affected. This is further supported by recent EFM measurements which found that a large intratube resistance is present at the crossing [27].

It has been suggested that carbon nanotube crossings provide an excellent opportunity to probe the interaction between Luttinger liquids, and some experiments have already been interpreted in this context [7, 28]. Calculations so far have however neglected scattering due to the presence of the crossing [29]. The effect of scattering is expected to be large since, for example, an impurity is predicted to lead to vanishing conductance in a Luttinger liquid at $T = 0$. Our observation of a severe distortion of the electronic structure at the crossing implies that the approximation of negligible scattering probably does not hold

under current experimental conditions. Additional experiments which minimize the amount of mechanical strain at the crossing, or corrections to the theory to include the role of this strain, will be required to resolve this matter.

In summary, we have presented STM and STS results on SWNT junctions. From analysis of topography measurements, we estimated the contact force between crossing nanotubes to be at most 1 nN. Spectroscopy measurements on crossed tubes show clear modifications of the band structure due to the crossing. Two types of effects were observed: band bending which we attribute to non-uniform doping by the substrate, and localized states due to interactions between the nanotubes at the crossing.

Acknowledgements

This chapter has been submitted to Physical Review B.

References

[1] S.J. Tans, M.H. Devoret, H. Dai, A. Thess, R.E. Smalley, L.J. Geerligs and C. Dekker, Nature **386**, 474 (1997).

[2] M. Bockrath, D.H. Cobden, P.L. McEuen, N.G. Chopra, A. Zettl, A. Thess and R.E. Smalley, Science **275**, 1922 (1997).

[3] S.J. Tans, A.R.M. Verschueren and C. Dekker, Nature **393**, 49 (1998).

[4] R. Martel, T. Schmidt, H.R. Shea, T. Hertel and Ph. Avouris, Appl. Phys. Letters **73**, 2447 (1998).

[5] H.W.Ch. Postma, T. Teepen, Z. Yao, M. Grifoni and C. Dekker, Science **293**, 76 (2001).

[6] Z. Yao, H.W.Ch. Postma, L. Balents and C. Dekker, Nature 402, 273 (1999).

[7] H.W.Ch. Postma, M. de Jonge, Z. Yao, and C. Dekker, Phys. Rev. B **62**, 10653 (2000).

[8] M.S. Fuhrer, J. Nygard, L. Shih, M. Forero, Y.G. Yoon, M.S.C. Mazzoni, H.J. Choi, J. Ihm, S.G. Louie, A. Zettl and P.L. McEuen, Science **288**, 494 (2000).

[9] J.W.G. Wildöer, L.C. Venema, A. Rinzler, R.E. Smalley and C. Dekker, Nature **391**, 59 (1998).

[10] T. Odom, J.-L. Huang, P. Kim and C.M. Lieber, Nature **391**, 62 (1998).

[11] J.W. Janssen, S.G. Lemay, M. van den Hout, M. Mooij, L.P. Kouwenhoven and C. Dekker, *Electronic Properties of Novel Materials - Molecular Nanostructures*; Editors: H. Kuzmany, J. Fink, M. Mehring and S. Roth, AIP Melville, New York (2001).

[12] M. Ouyang, J.-L. Huang, C.L. Cheung and C.M. Lieber, Science **291**, 97 (2001).

[13] J.W.G. Wildöer, A.J.A. van Roy, H. van Kempen and C.J.P.M. Harmans, Rev. Sci. Inst. **65**, 2849 (1994).

[14] J. Israelachvili, *Intermolecular & Surface forces* (Academic Press, London, 1994).

[15] L.C. Venema, J.W. Janssen, M.R. Buitelaar, J.W.G. Wildöer, S.G. Lemay, L.P. Kouwenhoven and C. Dekker, Phys. Rev. B **62**, 5238 (2000). We use 2.6 eV as the value for the overlap integral γ_0, see Ref. [24].

[16] For a review see, A. Krishnan, E. Dujardin, T.W. Ebbesen, P.N. Yianilos and M.M.J. Treacy, Phys. Rev. B **58**, 14013 (1998) and references therein.

[17] T. Hertel, R.E. Walkup and Ph. Avouris, Phys. Rev. B **58**, 13870 (1998).

[18] A.H. Cottrell, *The Mechanical Properties of Matter* (John Wiley & Sons, New York, 1964).

[19] R. Wiesendanger, *Scanning Probe Microscopy and Spectroscopy* (Cambridge University Press 1994).

[20] Y.G. Yoon, M.S.C. Mazzoni, H.J. Choi, J. Ihm and S.G. Louie, Phys. Rev. Lett. **86**, 688 (2001).

[21] T. Hertel, R. Martel, and Ph. Avouris, J. Phys. Chem. B **102**, 910 (1998).

[22] J. Tersoff and D.R. Hamann, Phys. Rev. B **31**, 805 (1985).

[23] A small suppression of the DOS can also be seen near zero bias with an energy width of ~ 50 meV at all positions. This feature is present in essentially all our STS measurements on metallic SWNTs [15] and is discussed separately, see chapter 8.

[24] S.G. Lemay, J.W. Janssen, M. van den Hout, M. Mooij, M.J. Bronikowski, P.A. Willis, R.E. Smalley, L.P. Kouwenhoven and C. Dekker, Nature **412**, 617 (2001).

[25] S. Iijima, C. Brabec, A. Maiti and J. Bernholc, J. of Chem. Phys. **104**, 2089 (1996).

[26] A. Rochefort, Ph. Avouris, F. Lesage and D.R. Salahub, Phys. Rev. B **60**, 13824 (1999).

[27] A. Bachtold, private communications; the measurement method is described in A. Bachtold, M.S. Fuhrer, S. Plyasunov, M. Forero, E.H. Anderson, A. Zettl and P.L. McEuen, Phys. Rev. Lett. **84**, 6082 (2000).

[28] J. Kim, K. Kang, J. Lee, K. Yoo, J. Kim, J. Park, H. So and J. Kim, cond-mat/0005083 (2000).

[29] A. Komnik and R. Egger, Phys. Rev. Lett. **80**, 2881 (1998).

Chapter 8

Suppression of the differential conductance at zero bias in single wall carbon nanotubes

J.W. Janssen, S.G. Lemay, M. van den Hout,
M. Mooij, M.R. Buitelaar, J.W.G. Wildöer,
L.C. Venema, L.P. Kouwenhoven and C. Dekker

We discuss the observation of a suppression of the differential conductance at zero bias voltage observed in single wall carbon nanotubes. We show that this suppression can not be explained by band structure effects, such as the curvature induced 'gap', but more likely by interactions between electrons. For this, two models are discussed with respect to results: Coulomb blockade and Luttinger liquid theory. A full explanation for all our observations is lacking and we give recommendations for future experiments.

8.1 Introduction

The electronic properties of carbon nanotubes have been intensively studied in recent years, mainly because of their future prospect to play a key role in electronic devices on a molecular scale. The most dramatic property, the fact that nanotubes show either metallic or semiconducting behaviour, has been confirmed by scanning tunneling microscopy (STM) and spectroscopy (STS) measurements [1, 2]. This was the first verification of predictions on the electronic structure of carbon nanotubes. The predictions were based on imposing periodic boundary conditions on a sheet of graphite. This simple model works surprisingly well, but it breaks down when we look at smaller energy scales. Then, for example, the

curvature of the hexagonal lattice can introduce a small gap in the band structure of chiral metallic nanotubes [3]. Also finite size effects and interactions between the electrons can significantly modify the electronic structure.

Some of these corrections have been studied by previous investigations. The curvature induced gap has been measured in both transport [4] and STS measurements [5]. Multiple experiments have probed effects that were explained by the Luttinger liquid model which is based on strong interactions between electrons in one dimension [6, 7, 8]. In multiwall carbon nanotubes a suppression of tunneling was observed and explained within a Coulomb blockade model including electron-electron interactions [9].

In this article we report on our low energy observations in STS measurements on single wall carbon nanotubes. In other papers we have already mentioned the suppression of the density of states at zero bias [10, 11], here we describe our observations in detail and show its characteristics. We show how we can distinguish between the curvature induced gap and models based on interacting electrons like the Luttinger liquid model and the Coulomb blockade model. We do not have a conclusive interpretation for our data but we discuss the different models with respect to our data and give recommendations for future experiments.

8.2   Description of experimental data

Single-wall carbon nanotubes (SWNT) were produced using either laser evaporation (material A) or catalytically grown in high pressure carbon monoxide (material B) [12], both by the group of R.E. Smalley at Rice University, USA. A small amount of the raw material was ultrasonically dispersed in dichloroethane. A few droplets were deposited on gold (111) facets, which were formed by flame annealing a small (15 mm^3) piece of 99.99% pure gold. This procedure results in (mainly individual) carbon nanotubes on an atomically flat surface. Such a sample was cooled down in an Omicron LT-STM operated at 4.6 K or in a home-built 4 K STM [13], and scanned with 90%Pt/10%Ir tips which were cut under ambient conditions. All the results presented here were measured on nanotubes of material A or B (indicated in the text or in the figure captions) in the Omicron STM, except for Fig. 8.1a and Fig. 8.2, which were measured in the 4 K STM.

Scanning tunneling spectroscopy curves were obtained by turning the feedback off and sweeping the voltage while measuring the current. Such a curve was numerically differentiated to obtain a $dI/dV(V)$ curve. Measurements were performed on numerous individual metallic tubes ($\sim$30) and a number of metallic ropes ($\sim$10). This includes data that has been published to show the large energy

band structure of carbon nanotubes [1, 10]. The latter results were all obtained in the 4 K STM on material A. Here we focus on the low energy properties and show unpublished or new data, both on individual SWNTs as well as on ropes of SWNTs.

8.2.1   General behavior on individual SWNTs

In Fig. 8.1a a spectroscopy curve is shown measured on a 1.2 nm diameter metallic SWNT. The band structure of a metallic tube is apparent from the onsets of two van Hove singularities (vHs) at -0.8 eV and +1.1 eV. The positions of the vHs are not centered around zero bias voltage but are shifted towards positive energies by ~ 0.3 eV. We interpret this as charge transfer between the substrate and the tube [10]. In between the vHs dI/dV is finite and constant except for a clear suppression centered around zero bias voltage. The width of this suppression is ~ 200 meV and the depth is about 40% of the original dI/dV value. For comparison the low energy spectroscopy on gold is displayed in Fig. 8.1a as well. In all the measurements shown here the tip is checked on gold before or after measurements on nanotubes to make sure that the tip itself is featureless.
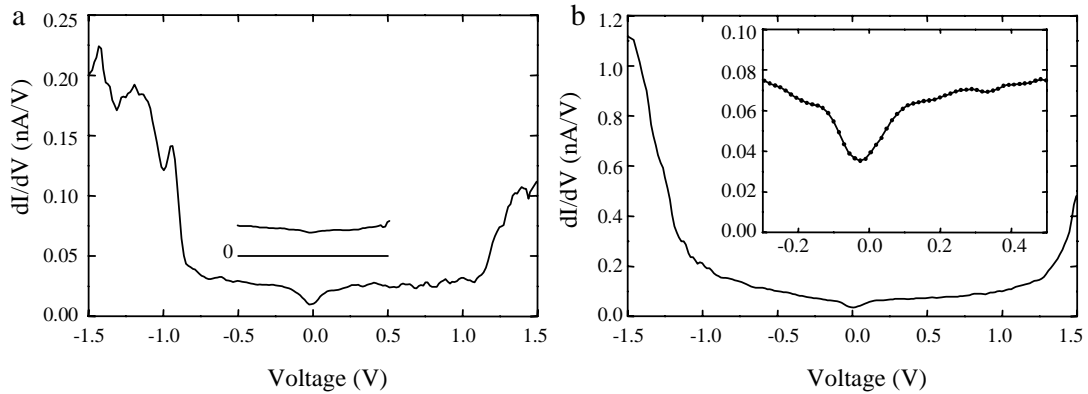
Figure 8.1: a) Large bias spectroscopy on a 1.2 nm diameter metallic SWNT (material A). The onsets of the vHs are visible at -0.8 eV and +1.2 eV. A spectroscopy curve measured on gold is plotted as well. The DOS is featureless around zero bias voltage. b) Large bias spectroscopy on a 1 nm diameter metallic SWNT (material B). The onsets of the vHs are not as pronounced as in (a) but the suppression at zero bias voltage is clearly visible. The insets zooms in on the suppression on a smaller energy scale. The black dots indicate the measured spectroscopy points.

Another example is shown in Fig. 8.1b where the spectroscopy on a 1.0 nm diameter SWNT is plotted. At -1.2 V and +1.3 V the pseudogap is bounded by two van Hove singularities (vHs). The inset of Fig. 8.1b shows in more detail the

shape of the suppression, the dots indicate the measured points. The suppression of about 50% has a width of ~ 150 meV.

The suppression of dI/dV described above is observed in essentially all metallic tubes studied. The width and depth of the suppression change from tube to tube. Typical values lie between 20 to 200 meV for the width and 20 to 80% suppression for the depth. The suppression is *always* around zero bias voltage whereas the shift in position of the vHs exhibits slight changes from sample to sample due to differences in charge transfer. There is no clear relation between the width or depth and the measured diameter of the tube or its chirality.
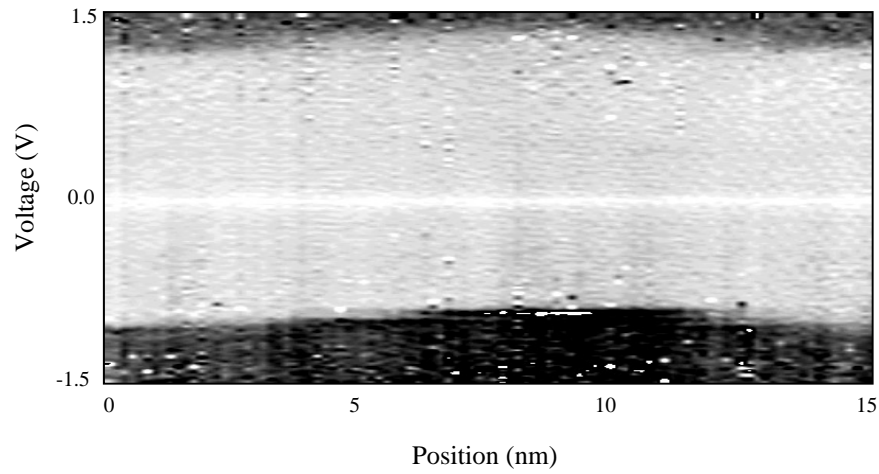
Figure 8.2: The differential conductance dI/dV for the metallic tube in Fig. 8.1b shown as a function of position along the nanotube (x axis) and sample bias voltage (y axis). The grayscale indicates the magnitude of dI/dV. White corresponds to no conductance or 0 nA/V, black to 0.2 nA/V. The vHs change in energy position along the tube axis whereas the suppression at zero bias voltage does not change.

In Fig. 8.2 the magnitude of dI/dV is plotted in grayscale as a function of both position along the longitudinal axis of the tube (x axis) and bias voltage (y axis). The figure is made up out of 100 curves like the ones displayed in Fig. 8.1 measured on equidistant positions over 15 nm along the SWNT axis. The curve of Fig. 8.1a is measured on this tube at $x \approx 8$ nm. The onset of the vHs is pronounced around -0.9 eV and is also clearly visible around 1.1 eV. The onset energies of the vHs change slowly as a function of position and track each other. Such band bending is often observed. Possible causes are a change in contact with the substrate which influences the charge transfer [11] or a nearby localized charge which acts as a gate on the tube [14]. The striking observation here, is that the suppression at zero bias, the white stripe in the figure, stays at the same energy and does not track the shift in the vHs.

8.2.2 Spatial dependence

Figure 8.2 showed the spatial dependence of the vHs and the relative position of the suppression. At these large energy scales the exact shape of the suppression is not visible. Figure 8.3 shows the result of small bias spectroscopy with high energy resolution as a function of position on the tube. Again the magnitude of dI/dV is plotted as a function of both position (x axis) and bias voltage (y axis). On the left and on the right of the grayscale image two individual curves are plotted, measured at $x = 0$ nm and $x = 30$ nm, respectively. At $x = 0$ nm, one central dip is visible at $V = 0$ V surrounded by oscillations in dI/dV. At $x = 30$ nm, the position in energy of the oscillations has significantly changed. As this figure shows, we observe a clear spatial dependence on this low energy scale, with a typical length scale of 10-20 nm. On three tubes we have investigated the shape of the suppression as a function of position up to this detail, with similar results.
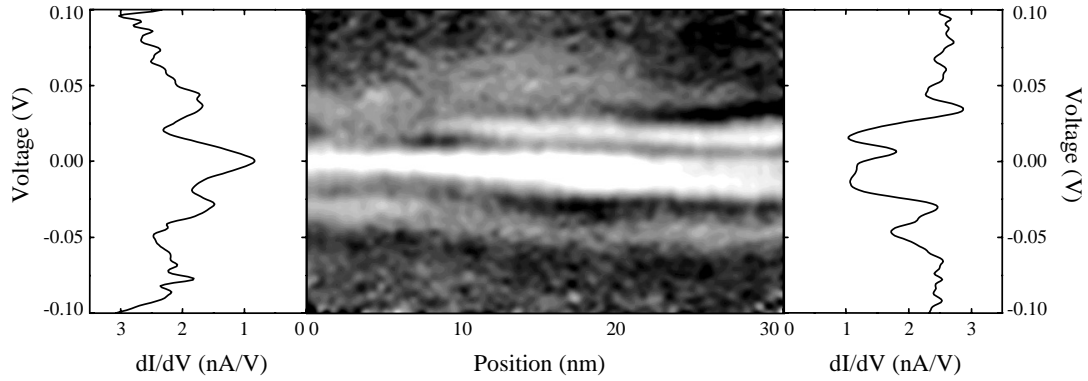
Figure 8.3: Small bias differential conductance dI/dV for an individual metallic SWNT (material B) shown as a function of position along the nanotube (x axis) and sample bias voltage (y axis). The grayscale indicate the magnitude of dI/dV, white is 1 nA/V and black is 3 nA/V. On this low energy scale clear fluctuations in the shape of the suppression are visible which are highlighted by the two single curves plotted on the left and right of the figure. They correspond to dI/dV measured at $x = 0$ nm and $x = 30$ nm, respectively.

8.2.3 Suppression on ropes of SWNTs

We have also observed a suppression of dI/dV on ropes of SWNTs. In Fig. 8.4a large bias spectroscopy curves are displayed measured both on gold and on a 'metallic' rope. The ropes we have studied here generally consists of 3 to 5 individual tubes and are recognized both from a larger apparent height as well
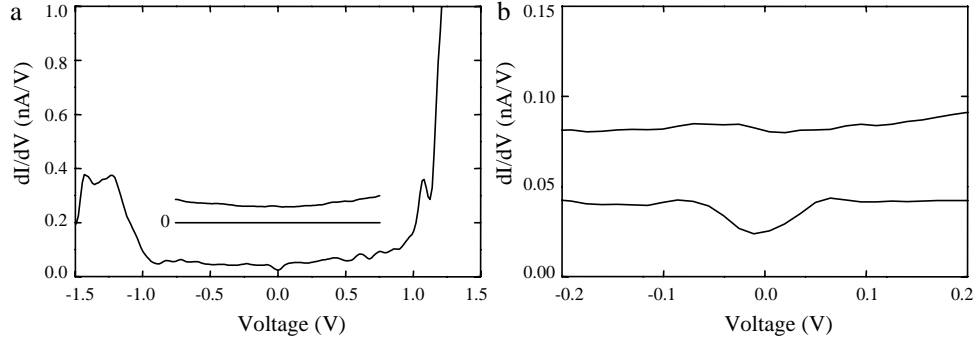
**Figure 8.4:** a) Large bias spectroscopy on a rope with an apparent height of 3 nm (material A). The dI/dV measured on gold is plotted as well and is featureless whereas on the rope a suppression of the DOS is visible at zero bias. b) Small bias spectroscopy on both the rope and the gold. The width of the suppression is ~ 100 meV.

as from anomalous spectroscopy curves that can not be attributed to the band structure of an individual SWNT. When a rope has a constant non-zero dI/dV over a ~ 1 V energy range around 0 V, most likely a metallic rope is dominating the spectroscopic behavior. Again we concentrate on the small bias spectroscopy. In Fig. 8.4a we also plotted the spectroscopy measured on gold which is essentially featureless. The spectroscopy measured on the rope shows a clear suppression of dI/dV at zero bias. Figure 8.4b zooms in on the suppression. The width of the suppression is 100 meV and this is about the largest width we observe on ropes. Out of 10 metallic ropes measured, the measured widths range from 20 to 100 meV and the depth changes from a 30% suppression to a real zero dI/dV.

Where the suppressions observed on individual metallic SWNTs had a very homogeneous shape on all SWNTs, on ropes we see a much richer behaviour. Here we give three examples. In Fig. 8.5a spectroscopy on a rope shows a very asymmetric suppression almost down to zero dI/dV. For comparison the spectroscopy measured on gold is displayed as well and the difference is striking. Compared to curves measured on individual SWNTs the edges of the suppression are sharper. Typical values for the broadening are 20 meV in individual SWNTs and 5-10 meV in ropes of SWNTs. In Fig. 8.5b dI/dV becomes really zero between -0.02 and 0.01 eV and three pronounced peaks are visible at -0.05, -0.03 and 0.02 eV. This extreme case was only observed once. Also on ropes we looked at the spatial dependence, see Fig. 8.5c. The two curves are measured on the same rope some 25 nm from each other. Besides the central suppression of dI/dV, oscillations are visible in both curves which change as a function of position. In 4 cases comparable behaviour was observed.
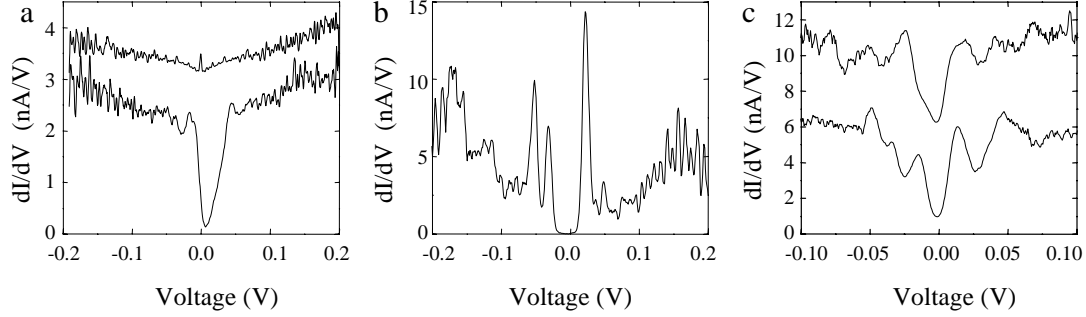
Figure 8.5: Three other examples of the suppression at zero bias measured on ropes. a) A steep and narrow suppression which almost goes down to 0 nA/V. The curve measured on gold is also plotted with an offset of 1 nA/V (material A). b) A real zero DOS surrounded by sharp peaks or singularities. Different singularities are visible (material B). c) The DOS measured on two different positions 25 nm away from each other, the upper curve has an offset of 5 nA/V. Oscillations in dI/dV change as a function of position (material A).

8.3 Possible physical mechanisms

To explain our observations we look at modifications of the band structure and effects arising from interacting electrons. For the latter we see two possible models that cause a suppression of dI/dV at the Fermi energy: (i) Coulomb blockade, when we treat the tip-tube-gold as a double junction system, and (ii) Luttinger liquid behavior, based on the fact that nanotubes are one dimensional conductors. In this section we discuss these three possible explanations.

8.3.1 Curvature induced gap

Chiral metallic SWNTs are in fact zero gap semiconductors. The curvature of the carbon lattice breaks the symmetry, causing a change in the overlap of atomic orbitals, which opens a gap at the charge neutrality point [3]. The size of this gap depends on the chiral angle ϕ and is inversely proportional to the square of the diameter d by $E_{smallgap} = \gamma_0 a_0{}^2 \sin(3\phi)/4d^2$. Here $a_0 = 0.246$ nm, the lattice constant and $\gamma_0 = 2.6$ eV, the overlap energy [15]. For our tubes with a typical diameter of 1.4 nm the theoretical gap size ranges from 0 meV for an armchair tube to 20 meV for a zigzag tube with a 30° chiral angle. Due to the shift towards positive voltage the charge neutrality point lies around +0.3 eV in our curves. Furthermore, Fig. 8.2 shows that the observed suppression at zero bias does not follow bending of bands. This provides conclusive evidence that our suppression can not be interpreted as the curvature induced gap.

In Fig. 8.1b the voltage range covers the charge neutrality point which lies at +0.31 V. Here a small suppression can be seen but it is too speculative to attribute this to the curvature induced gap. Also in other curves no gap was found at the charge neutrality point. Our curves are broadened by ~ 20 meV and it is likely that this obscures the curvature induced gap, especially for chiral angles smaller than 30° where the gap is smaller than 20 meV.

In Ref. [5] the observation of a suppression or 'gap' similar to ours is reported and interpreted as the curvature induced gap. In those experiments no shift in the vHs is observed and the charge neutrality point thus coincides with zero bias voltage. Since our spectroscopy curves are shifted we are able to distinguish between band structure properties and effects at the Fermi energy from interacting electron. The latter we discuss now.

8.3.2   Coulomb blockade

When we treat the nanotube as an island connected by two junctions to both the tip and the gold, we can define a charging energy needed to put one extra electron on the island. This finite energy leads to a Coulomb gap around zero bias voltage and the size depends on the total capacitance $C_\sum$ by $E_{charging} = e^2/2C_\sum$. An offset charge can change the size of this gap from this maximum value to zero.

With a simple double junction model we are able to fit the suppression reasonably well. The parameters used to fit our largest gaps are $R_{tip-tube} = 200$ MΩ, $C_{tip-tube} = 100 \times 10^{-21}$ F, $R_{tube-gold} \approx 50$ kΩ (see below) and $C_{tube-gold} = 3 \times 10^{-18}$ F. We use the feedback settings of the STM to calculate $R_{tip-tube}$ since we expect that $R_{tube-gold}$ is small compared to $R_{tip-tube}$. The capacitances are estimated based on simulations [16]. To fit the broadening of the curves we used an effective temperature of ~ 50 K. We discuss the broadening below.

To test the Coulomb blockade model, we measured dI/dV at a fixed spot using different feedback setting. By changing $R_{tip-tube}$ we change the tip-tube distance and thus $C_{tip-tube}$, which should have an effect on the size of the Coulomb gap. Such a measurement is plotted in Fig. 8.6. Here the small bias spectroscopy curves are plotted for feedback bias voltages of 1 V, 0.8 V, 0.5 V and 0.2 V and a current of 500 pA. In Fig. 8.6 we observe oscillations next to the small suppression with a width of 20 mV. The suppression becomes wider for a smaller voltage and also the position of the oscillations changes. $R_{tip-tube}$ changes from 400 MΩ for the top curve to 2 GΩ for the bottom curve. This roughly changes the tip-tube distance by 1 Å. Simulations show that this has only a small effect on $C_{tip-tube}$, using a typical tunneling distance of 7 Å between tip and tube. The small variation in the size of the gap and position of the oscillations in Fig. 8.6
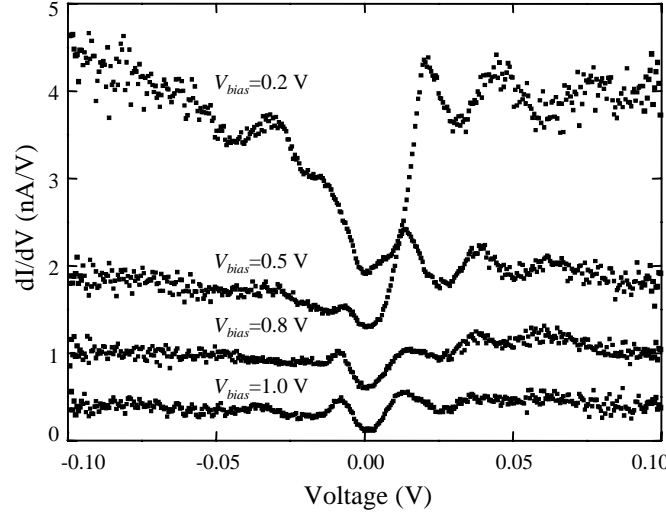
Figure 8.6: The suppression for different feedback voltages, 1.0 V, 0.8 V, 0.5 V and 0.2 V. Curves are offset by 0.0, 0.5, 1.0 and 1.5 nA/V, respectively. Oscillations in the DOS are visible. The change in feedback voltage adjusts the distance between the tip and the tube and thus the tube-tip capacitance. We observe a small variation in the size of the gap and the positions of the oscillations.

can be caused by the change in capacitance but further measurements are needed to draw a firm conclusion.

The broadening is much higher than the thermal smearing at 4 K, which is ~ 1 meV, and is possibly caused by hybridization of orbitals in a nanotube with orbitals of the gold substrate [17]. This can lead to higher order tunneling processes like co-tunneling. Broadening can also be caused by charge fluctuations. These can arise if $R_{tube-gold}$ is close to the quantum resistance. This is possible since we find in our simulations that the exact value of $R_{tube-gold}$ is of little influence as long as it is small compared with $R_{tip-tube}$. We can account for these effects by using a higher effective temperature [18]. On ropes the broadening is smaller possibly due other semiconducting tubes in the rope that uncouple the metallic tube from the gold substrate. We did not look into the details of these effects yet but we think that they possibly also can provide explanations for the observed oscillations and the spatial dependence.

We can exclude that the effective temperature of 50 K is due to bad filtering of the wires or non-efficient cooling of the STM, since we can measure the superconducting properties and vortices on NbSe$_2$, which has a T_c of 7.2 K.

8.3.3 Luttinger liquid

Carbon nanotubes are considered truly one dimensional conductors. Interactions between the electrons cause them to aggregate into one correlated electron fluid, the Luttinger liquid [19, 20]. This results in a vanishing DOS at the Fermi energy. Electrons tunneling into a Luttinger liquid therefore need a finite energy to enter a SWNT, which can cause a suppression of the differential conductance at the Fermi level. The strength of the interactions are described by the interaction parameter g, which is estimated to be 0.2-0.3 from fitting power laws to conductance measurements where tubes lie on an insulating substrate [6, 7, 8]. For our layout of nanotubes on a conducting gold substrate, screening of the interactions is expected to be much better which results in value for g closer to 1, where $g = 1$ corresponds to no interactions. Screening by a conducting plane has been modeled but only for planes far away with respect to the nanotube diameter [21]. To our knowledge no description is available for a plane very close to the nanotube. Based on the available models [21, 22] this is a non-trivial modification and not easy to solve [23].

For finite lengths different Luttinger liquid phenomena are expected, this is for example seen in transport experiments were a difference was observed for electrons tunneling close to the end or in the middle of a nanotube [8]. This length scale is set by the thermal length $L_{thermal} = \hbar v_F / k_B T$ which equals ~ 1 μm at 4 K. In our STM observations we rarely observe tubes which are longer than 1 μm. Thus, Luttinger liquid phenomena can be expected to be modified. Combining this with the weaker interactions due to more efficient screening the total effect of Luttinger liquid behavior on our spectroscopy curves is expected to be small. We believe that it is unlikely that Luttinger phenomena can cause the spatial dependence observed in Fig. 8.3 [23].

8.4 Conclusion and recommendations

We have presented the observation of a suppression of the differential conductance at zero bias voltage, both on individual tubes as well as on ropes. We have shown that the suppression can not be interpreted as the curvature induced 'gap' but, more likely, has to be explained by interactions between electrons. We have discussed two models that include interacting electrons with respect to our results: Coulomb blockade and Luttinger liquid theory. However, no conclusive explanation for the suppression at zero bias has been found yet.

Both models can be tested further. We propose a few other or additional experiments. A higher range in voltage and current can be used to repeat the

experiment as shown in Fig. 8.6. Here we only changed the voltage but changing the current too, allows for covering a larger range in tunnel resistances resulting in a larger range in capacitance and hence a more clear change of the size of the gap and the position of the oscillations.

Testing the Luttinger model most likely requires less efficient screening which can be realized by using insulating layers in between a nanotube and the (gold) substrate or by suspending nanotubes over trenches, eventually filled with non-conducting material to allow for stable imaging. Also the temperature dependence of the suppression could be measured, for example, to check if the thermal length does influence Luttinger phenomena.

This chapter is in preparation for Phys. Rev. B.

References

[1] J.W.G. Wildöer, L.C. Venema, A. Rinzler, R.E. Smalley and C. Dekker, Nature **391**, 59 (1998).

[2] T. Odom, J.-L. Huang, P. Kim and C. Lieber, Nature **391**, 62 (1998).

[3] C.L. Kane and E.J. Mele, Phys. Rev. Lett. **78**, 1932 (1997).

[4] C. Zhou, J. Kong and H. Dai, Phys. Rev. Lett **84**, 5604 (2000).

[5] M. Ouyang, J.-L. Huang, C.L. Cheung and C.M. Lieber, Science **292**, 702 (2001).

[6] M. Bockrath, D.H. Cobden, A.G. Rinzler, R.E. Smalley, L. Balents and P.L. McEuen, Nature **397**, 598 (1999).

[7] Z. Yao, H.W.Ch. Postma, L. Balents and C. Dekker, Nature 402, 273 (1999).

[8] H.W.Ch. Postma, M. de Jonge, Z. Yao, and C. Dekker, Phys. Rev. B **62**, 10653 (2000).

[9] A. Bachtold, M. de Jonge, K. Grove-Rasmussen, P.L. McEuen, M.R. Buitelaar and C. Schönenberger, accepted for publication in Phys. Rev. Lett.

[10] L.C. Venema, J.W. Janssen, M.R. Buitelaar, J.W.G. Wildöer, S.G. Lemay, L.P. Kouwenhoven and C. Dekker, Phys. Rev. B **62**, 5238 (2000).

[11] J.W. Janssen, S.G. Lemay, L.P. Kouwenhoven and C. Dekker, submitted to Phys. Rev. B.

[12] M.J. Bronikowski, P.A. Willis, D.T. Colbert, K.A. Smith and R.E. Smalley, J. Vac. Sci. & Technol. A **19**, 1800 (2001).

[13] J.W.G. Wildöer, A.J.A. van Roy, H. van Kempen and C.J.P.M. Harmans, Rev. Sci. Inst. **65**, 2849 (1994).

[14] R. Wilkins and R.C. Jaclevic, Phys. Rev. Lett **63**, 801 (1989); J.G.A. Dubois, E.N.G. Verheijen, J.W. Gerritsen and H. Van Kempen, Phys. Rev. B **48**, 11260 (1993).

[15] S.G. Lemay, J.W. Janssen, M. van den Hout, M. Mooij, M.J. Bronikowski, P.A. Willis, R.E. Smalley, L.P. Kouwenhoven and C. Dekker, Nature **412**, 617 (2001).

[16] The program used for the capacitance simulations is FastCap, developed by the Research Laboratory of Electronics at MIT (1992). See also Ref. [10].

[17] J.W. Gadzuk, Phys. Rev. B **1**, 2110 (1970).

[18] D.C. Glattli, Physica B **189**, 88 (1993).

[19] R. Egger and A. Gogolin, Phys. Rev. Lett. **79**, 5082 (1997).

[20] C. Kane, L. Balents and M.P.A. Fisher, Phys. Rev. Lett. **79**, 5086 (1997).

[21] R. Egger and A.O. Gogolin, Eur. Phys. Journal B **3**, 281 (1998).

[22] T. Kleimann, M. Sassetti, B. Kramer and A. Yacoby, Phys. Rev. B **62**, 8144 (2000).

[23] M. Thorwart and M. Grifoni, private communications.

Chapter 9

Imaging electron wave functions of quantized energy levels in carbon nanotubes

L.C. Venema, J.W.G. Wildöer, J.W. Janssen,
S.J. Tans, H.L.J. Temminck Tuinstra,
L.P. Kouwenhoven and C. Dekker

Carbon nanotubes provide a unique system for studying one-dimensional quantization phenomena. Scanning tunneling microscopy was used to observe the electronic wave functions that correspond to quantized energy levels in short metallic carbon nanotubes. Discrete electron waves were apparent from periodic oscillations in the differential conductance as a function of position along the tube axis, with a period that differed from that of the atomic lattice. Wave functions could be observed for several electron states at adjacent discrete energies. The measured wavelengths are in good agreement with the calculated Fermi wavelength for armchair nanotubes.

9.1 Introduction

Carbon nanotubes are molecular wires that exhibit fascinating electronic properties [1]. Electrons in these cylindrical fullerenes are confined in the radial and circumferential directions and can only propagate in the direction of the tube axis. Nanotubes are therefore interesting systems for studying the quantum behavior of electrons in one dimension (1D). Limiting the length of a carbon nanotube leads to a 'particle in a box' quantization of the energy levels. Such discrete energy levels have been observed in transport experiments on individual nanotubes and

87

ropes [2, 3]. The electron wave functions corresponding to these discrete states can in principle be imaged by scanning tunneling microscopy (STM). The well-known STM work on quantum corrals demonstrated the possibility to directly image wave patterns in the local density of states of a 2D metal surface [4]. Here, we apply this technique to map out the wave functions of single molecular orbitals in short metallic carbon nanotubes. Electronic wave functions are apparent from periodic oscillations in the low-bias differential conductance along the tube axis. To our knowledge, this is the first time that wave functions of discrete electron states have been imaged in a molecular wire.

Previous STM spectroscopy studies were done at a large (~ 2 eV) energy scale to investigate the band structure of nanotubes [5, 6]. These experiments confirmed the prediction [7] that carbon nanotubes can be semiconducting or metallic depending on the tube diameter and the chiral angle between the tube axis and hexagon rows in the atomic lattice. In this paper we focus on the low-energy (~ 0.1 eV) features of short metallic nanotubes which exhibit quantum size effects. Single-wall nanotubes with a diameter of about 1.4 nm were deposited on Au(111) substrates [5, 8].
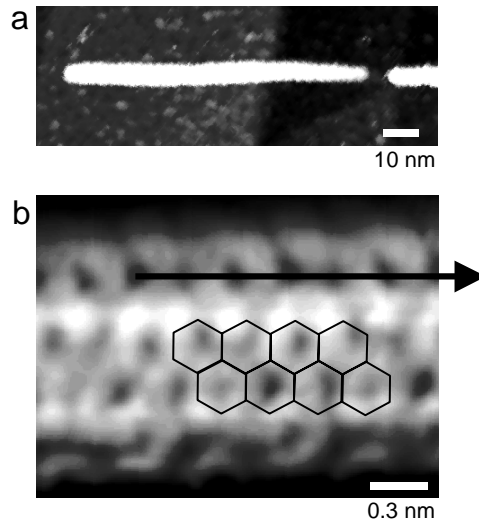
Figure 9.1: STM topographic images of individual single-wall carbon nanotubes. a) Example of a nanotube shortened by applying a voltage pulse to the STM tip above the tube [11]. b) Atomically resolved image of an armchair nanotube. The arrow denotes the direction of the tube axis. This nanotube can be identified as armchair-type because the hexagon rows run parallel to the direction of the tube axis (cf. overlay of the graphene lattice). The tube diameter is 1.3 nm. This image has been taken before the tube was shortened to 30 nm. Feedback parameters are $V = 0.1$ V, $I = 20$ pA. Images were taken in constant-current mode.

9.2 Experimental results and discussion

On most tubes we were able to obtain STM images with atomic resolution [5] which allows to determine the chiral angle and diameter of the tubes [9]. The nanotube of Fig. 9.1b is identified as an 'armchair' tube from the good fit between the observed hexagon structure and the overlay of the graphene lattice. Armchair tubes have a nonchiral structure because the hexagon rows are parallel to the tube axis. This type of tubes has metallic properties [7]. Current-voltage $I(V)$ characteristics measured up to ± 0.5 V on the armchair tube of Fig. 9.1b indeed demonstrate the simple linear behavior expected for a metallic tube. Such $I(V)$ measurements are done by keeping the STM tip stationary above the nanotube, switching off the feedback, and recording the current as a function of the voltage applied to the sample. In all our experiments the STM is operated at 4.2 K [10].

In the experiments reported here, the armchair tube of Fig. 9.1b was shortened to a length of about 30 nm. This was achieved by locally cutting the tube by applying a voltage pulse of +5 V to the STM tip at a position on the tube located 30 nm from its end [11]. STM spectroscopy was then carried out near the middle of the short tube. $I(V)$ curves on the shortened nanotube show a step-like behavior (Fig. 9.2a), which we ascribe to quantum size effects.

Steps in $I(V)$ correspond to quantized energy levels entering the bias window upon increasing the voltage. Current steps at a voltage V thus correspond to discrete electron states at energy $E = E_F + \alpha eV$, with E_F the Fermi energy, e the electron charge, and $\alpha \simeq 1$ [12]. The experimentally observed width of the current plateaus between the steps ranges from 0.05 V to 0.09 V. The plateau width is determined by the total energy to add an electron to the tube. This addition energy consists of a combination of finite-size level splitting and the Coulomb charging energy that is due to the small capacitance of the tube. A simple estimate for the energy level splitting for a tube of length $L = 30$ nm is given by $\Delta E = h v_F / 2L = 0.06$ eV, where $v_F = 8.1 \times 10^5$ m/s is the Fermi velocity and h is Plancks constant. The capacitance of a nanotube lying on a metallic substrate can be approximated by the formula for a metallic wire parallel to a conducting plane, $C = 2\pi\epsilon_0 L / \ln[(d + \sqrt{(d^2 - R^2)})/R]$ [13], where $\epsilon_0 = 8.85 \times 10^{-12}$ F/m, d is the distance from the wire axis to the plane and $R = 0.65$ nm is the wire radius. Estimating $d \approx 0.9$ nm gives $C \approx 2.0$ aF, which yields a charging energy $E_c = e^2/C = 0.08$ eV. Both numbers are in the same range as the observed plateau width. Since the charging energy and level splitting are of about equal magnitude, an irregular step spacing in the $I(V)$ curve is expected [14]. For this report, the main point is that each step corresponds to a discrete energy level entering the bias window.
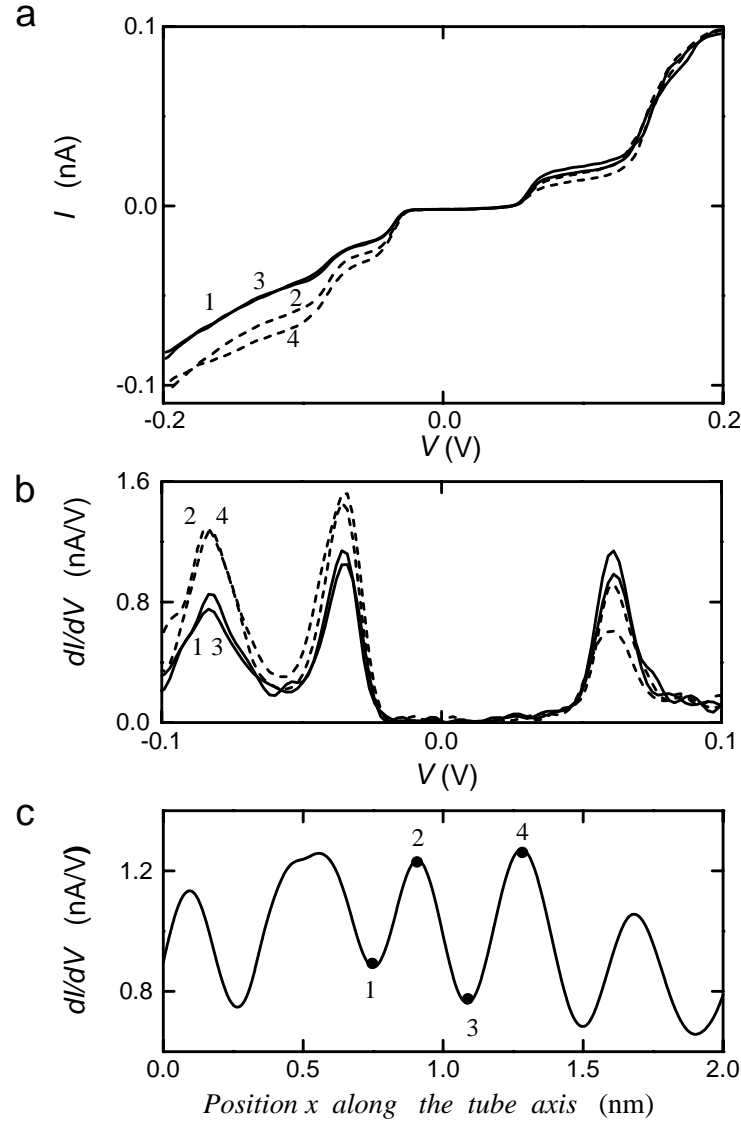
Figure 9.2: STM spectroscopy measurements on a 30 nm long armchair tube. a) Current-voltage $I(V)$ characteristics on the tube shown in Fig. 9.1b, taken at positions about 0.18 nm apart (data points 1 to 4 in (c)) on a straight line along the tube axis. Current steps correspond to discrete energy states entering the bias window. b) Differential conductance dI/dV versus V, as calculated from the $I(V)$ curves. Peaks appear at the voltage positions of current steps in the $I(V)$ curves. c) Differential conductance dI/dV as a function of position along the tube. Data was taken at a bias voltage of -0.08 V. Data points 1 to 4 indicate the positions at which the four $I(V)$ curves plotted in (a) and dI/dV curves in (b) were obtained.

The central result of our experiments is that the tunneling conductance measured for such discrete states is found to oscillate along the length direction of the nanotube with a period different from the atomic lattice constant. $I(V)$ spectroscopy curves were obtained at different locations on top of the nanotube along a line parallel to the tube axis in constant-current mode. At every point, spaced 23 pm apart, the feedback was switched off to take an $I(V)$ curve, starting at the bias voltage used for feedback in the constant-current mode. Figure 9.2a shows several $I(V)$ curves obtained in this way at different positions. The current displays a clear variation between maximum (dashed curves) and minimum values (solid curves) for negative bias voltage. Peaks in the differential conductance dI/dV (Fig. 9.2b) appear at the voltage positions of current steps in the $I(V)$ curves. The height of the dI/dV peaks varies periodically with position x along the tube axis, as shown in Fig. 9.2c. The period of these oscillations in the differential conductance is about 0.4 nm, which clearly differs from the lattice constant of 0.25 nm. The periodic variation of dI/dV versus x can - as discussed below in detail - be attributed to the electronic wave functions in the nanotube.

The wave functions of several adjacent energy levels can be displayed simultaneously by plotting the differential conductance dI/dV as a function of the voltage and the position x along the tube (Fig. 9.3a). Wave patterns can be observed for 4 different energy levels appearing at bias voltages 0.11 V, 0.04 V, 0.00 V and -0.05 V [15]. At each level a horizontal row of about 7 maxima is resolved in dI/dV as a function of position x along the tube (see Fig. 9.3b for the 1D spatial profile of the wave functions belonging to these states). The experimental quantity dI/dV is a measure for the squared amplitude of the quantized electron wave function $|\psi(E, x)|^2$ [16]. The curves in Fig. 9.3b are fitted with a function of the form $dI/dV = A\sin^2(2\pi x/\lambda + \phi) + B$, which represents a simple trial function for $|\psi(E, x)|^2$. The separation of about 0.4 nm between peaks in dI/dV corresponds to half the wavelength λ, because dI/dV measures the square of the wave function. The wavelengths obtained from the fitting procedure vary from 0.66 to 0.76 nm (Fig. 9.3b). Other measurements on the same tube reproduced values for λ in the range of $0.65 - 0.8$ nm. From repeated spectroscopy measurements such as Fig. 9.3a on the same tube, we estimate the error in the wavelength to be about 0.02 nm. Note that the dI/dV maxima in Fig. 9.3a occur at different positions x for the different horizontal rows. This excludes many experimental artifacts such as for example oscillations in the STM and provides compelling evidence for the interpretation in terms of standing electron waves. Typically only a small number (~ 4) of discrete levels were observed around zero bias. At larger bias voltages (beyond the images shown here), peaks in $dI(V)/dV$ could no longer be discerned clearly. At these voltages the broadening of energy states apparently
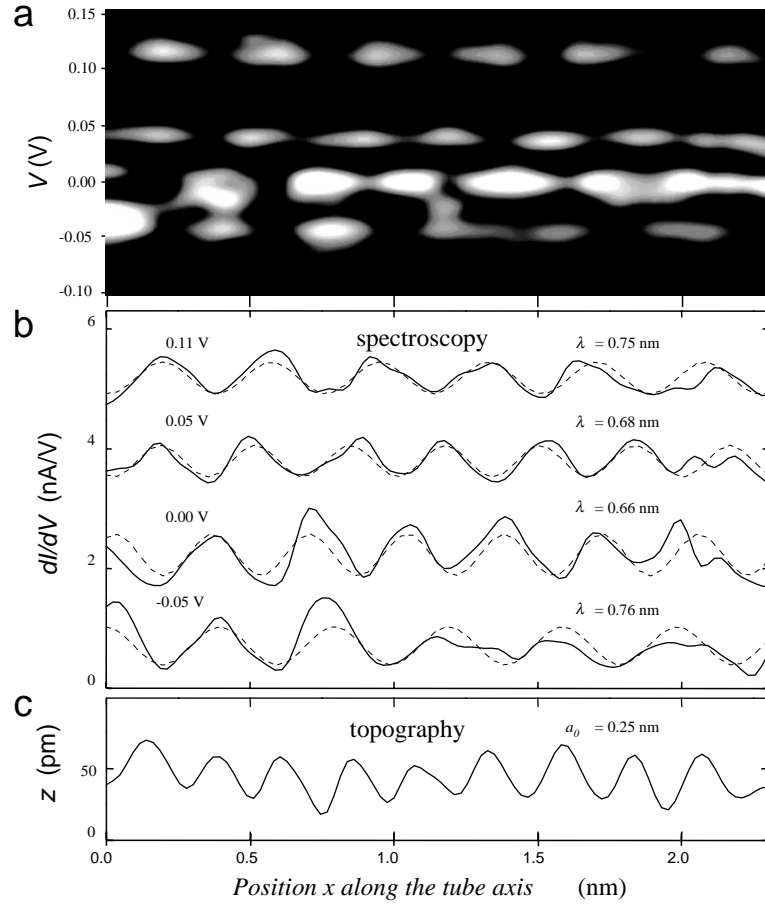
Figure 9.3: Spectroscopy and topography line scans along the nanotube which show electron wave functions of discrete electron states as well as the atomic lattice. a) Differential conductance dI/dV (in gray scale) against the bias voltage (y-axis) and the position on a straight line along the tube (x-axis). This plot results from about 100 $I(V)$ curves taken at positions about 23 pm apart along the tube axis. Electron wave functions of 4 different energy levels are observed as periodic variations in dI/dV along the tube at voltages of 0.11 V, 0.04 V, 0.00 V and -0.05 V. A horizontal row of about 7 dI/dV maxima is observed at each energy level. Note that the exact voltages at which the peaks in dI/dV appear in Fig. 9.2 and Fig. 9.3a are different [15]. b) dI/dV profiles at the 4 resolved energy levels. Fits of the function $dI/dV = A\sin^2(2\pi x/\lambda + \phi) + B$ are plotted as dashed curves. The resulting wavelengths λ are given above the curves on the right. Curves are vertically offset for clarity. c) Topographic height profile $z(x)$ of the nanotube. STM topographic imaging and spectroscopy was performed simultaneously by scanning the tip along the tube and recording both the tip height (with feedback on) and $I(V)$ spectroscopy curves (feedback off). Feedback parameters are $V = 0.3$ V and $I = 100$ pA.

exceeds their separation. Similar electron waves with a wavelength of about 0.7 nm were also observed in a number of other shortened metallic nanotubes. On shortened semiconducting nanotubes the level splitting could not be resolved and attempts to measure electron waves were unsuccessful. A small energy level splitting is indeed expected for semiconducting tubes since here the Fermi energy is located at the top of a band [5].

Figure 9.3c shows the topographic height profile from the constant-current measurement at +0.3 V, which clearly has a different periodicity from that observed in dI/dV (Fig. 9.3b). The period of 0.25 nm is in agreement with the atomic lattice constant $a_0 = 0.246$ nm for an armchair nanotube. Apparently we image the atomic corrugation at high bias voltage. Simultaneously, $I(V)$ spectroscopy curves are measured at every point (Fig. 9.3b and c), starting at the set-point used for feedback (100 pA and +0.3 V). As a result from maintaining feedback at this voltage, the lattice periodicity is largely compensated because the STM tip follows the atomic corrugation, which makes it possible to resolve the quantized electron waves in Fig. 9.3b and c [16].

Discrete levels are probed at energies near the Fermi energy E_F, and therefore the wavelength of the electron waves is close to the Fermi wavelength λ_F. Electronic band structure calculations [1, 7] for armchair tubes yield two bands near E_F with a linear energy dispersion $E(k) = E_F \pm \hbar v_F(k - k_F)$, where $\hbar = h/2\pi$, $k = 2\pi/\lambda$ is the wave vector, and $k_F = 2\pi/\lambda_F$ is the Fermi wave vector. In undoped nanotubes, the two bands cross at the Fermi energy where $k = k_F = 2\pi/3a_0$. This yields $\lambda_F = 3a_0 = 0.74$ nm, independent of the length of the tube. For nanotubes on Au(111) however, E_F is shifted away from the crossing point to lower energy by $\delta E = 0.3$ eV. This is due to charge transfer as a result of a difference in workfunction with the underlying substrate [5]. This shifts k_F to $k_F \pm \delta k$ with $\delta k = \delta E/\hbar v_F$, and λ_F thus becomes $2\pi/(k_F \pm \delta k) = 0.69$ nm (+) or 0.79 nm (−). The experimentally observed wavelengths (Fig. 9.3b) correspond well to the theoretical values, confirming the predicted band structure with two linear bands crossing near E_F. This result provides quantitative evidence for our interpretation of the oscillations in dI/dV in terms of wave functions of discrete electron states.

A short metallic nanotube resembles the textbook model for a particle in a 1D box. For a discrete energy state with quantum number n, the corresponding wavelength $\lambda_n = 2L/n$. The observed wavelength is much smaller than the tube length, in accordance with the fact that the number of electrons within one nanotube band is large ($n \sim 10^2$). The wavelength will therefore vary only slightly ($\lambda_n/n \sim 0.01$ nm) for adjacent discrete energy levels in one band.

The measurements reported here are technically challenging because they re-

quire a large series of reproducible $I(V)$ curves. Occasionally, we were able to resolve some of the spatial structure in the wave function at a length scale smaller than the Fermi wavelength, as shown in Fig. 9.4a. In this scan the peak spacing is non-equidistant, leading to an apparent 'pairing' of peaks. This feature indicates that the wave function does not conform to a simple sinusoidal form. Recent calculations by Rubio *et al.* [17] indicate a nontrivial spatial variation of the nodes in the wave function of discrete electron states in the direction perpendicular to the tube axis (compare Fig. 9.4b). Line profiles can either show pairing or an equidistant peak spacing depending on the exact position of the line scan. The observation of pairing confirms that the relevant period in the line scans is the distance between next-nearest-neighbor peaks.
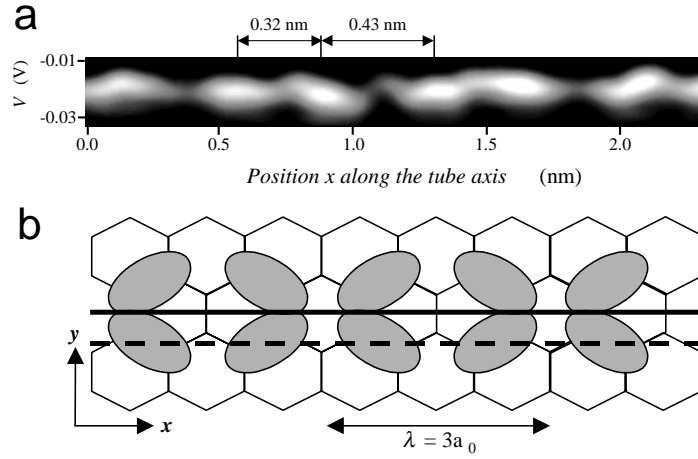
Figure 9.4: Pairing of conductance peaks. a) Spectroscopy line scan where pairing of dI/dV maxima can be observed. Neighboring peaks are non-equidistant, indicating a non-sinusoidal wave function. The distance between next-nearest-neighbor peaks is approximately 0.75 nm which agrees with the Fermi wavelength. b) Schematic of a possible arrangement of lobes of the wave function of a single molecular orbital. In a line scan along the dashed line, peaks in dI/dV will be equidistant, whereas pairing will occur if a line scan is carried out along the solid line.

9.3   Conclusion and outlook

Our experiments demonstrate that individual wave functions corresponding to the quantized energy levels in a short metallic nanotube can be resolved because of the large energy level splitting. The technique for recording the wave periodicity at different energy states provides a tool for further exploration of the dispersion relation in nanotubes. Future work will include similar experiments on nanotubes

with various chiral angles. The methodology presented in this paper also opens up the possibility of obtaining full 2D spatial maps of the electron wave functions in carbon nanotubes.

Acknowledgements

This chapter has been published in Science **283**, 52 (1999).

References

[1] M.S. Dresselhaus, G.Dresselhaus and P. C. Eklund, *Science of Fullerenes and Carbon Nanotubes* (Academic Press Inc., San Diego, 1996)

[2] M. Bockrath, D.H. Cobden, P.L. McEuen, N.G. Chopra, A. Zettl, A. Thess and R.E. Smalley, Science **275**, 1922 (1997).

[3] S.J. Tans, M.H. Devoret, H. Dai, A. Thess, R.E. Smalley, L.J. Geerligs and C. Dekker, Nature **386**, 474 (1997).

[4] M.F. Crommie, C.P. Lutz and D. M. Eigler, Science **262**, 218 (1993); M.F. Crommie, C.P. Lutz and D.M. Eigler, Nature **363**, 424 (1993); Y. Hasegawa and Ph. Avouris, Phys. Rev. Lett. **71**, 1071 (1993).

[5] J.W.G. Wildöer, L.C. Venema, A.G. Rinzler, R.E. Smalley and C. Dekker, Nature **391,** 59 (1998).

[6] T.W. Odom, J.-L. Huang, P. Kim and C.M. Lieber, Nature **391,** 62 (1998).

[7] J.W. Mintmire, B.I. Dunlap and C.T. White, Phys. Rev. Lett. **68**, 631 (1992); N. Hamada, S.-I. Sawada and A. Oshiyama, Phys. Rev. Lett. **68**, 1579 (1992); R. Saito, M. Fujita, G. Dresselhaus and M.S. Dresselhaus, Appl. Phys. Lett. **60**, 2204 (1992).

[8] A. Thess, R. Lee, P. Nikolaev, H. Dai, P. Petit, J. Robert, C. Xu, Y.H. Lee, S.G. Kim, A.G. Rinzler, D.T. Colbert, G.E. Scuseria, D. Tománek, J.E. Fischer and R.E. Smalley, Science **273**, 483 (1996).

[9] Exact identification of the exact lattice indices (n, m) (see ref. [1]) of chiral nanotubes is quite difficult since both the nanotube diameter and the chiral angle between hexagon rows and the tube axis have to be measured with

high accuracy. The (n, m) indices are crucial for chiral tubes because a minor change in one of these determines whether the tube is a metal or a semiconductor. For armchair tubes, however, the situation is easier. The non-chiral structure with hexagon rows running parallel to the tube axis can be easily observed from the atomically resolved images, and a precise determination of the diameter is not essential because armchair tubes of all diameters are metallic.

[10] J.W.G. Wildöer, A.J.A. van Roij, H. van Kempen and C.J.P.M. Harmans, Rev. Sci. Instrum. **65**, 2849 (1994). In our setup the lateral drift is almost negligible (typically less than 1 nm per hour) because the STM is cooled in a ^{4}He bath cryostat. Successive STM spectroscopy line scans therefore show identical results. Over a longer period, however, the tip may change position slightly as a result of residual drift as well as minor tip changes.

[11] L.C. Venema, J.W.G. Wildöer, H.L.J. Temminck Tuinstra and C. Dekker, Appl. Phys. Lett. **71**, 2629 (1997). After this cutting event the tip was cleaned by applying voltage pulses above the gold substrate, far away from the tube. Linear $I(V)$ spectroscopy curves on clean areas of the gold substrate demonstrated that the tip was free from any debris.

[12] The applied voltage is in principle divided into a part that drops over the tunnel gap and a part that drops between the nanotube and the substrate. The ratio α between these voltages is determined by the capacitance ratio. Because the capacitance between nanotube and substrate is much larger than that between the nanotube and the STM tip, the voltage will drop almost entirely over the tunnel gap, and accordingly α has a value close to 1.

[13] W.T. Scott, *The Physics of Electricity and Magnetism*, (John Wiley and Sons, Inc., New York, 1966, 2nd ed.), pp. 163-165.

[14] L.P. Kouwenhoven, C.M. Marcus, P.L. McEuen, S. Tarucha, R.M. Westervelt and N.S. Wingreen, in *Mesoscopic Electron Transport, proceedings of a NATO Advanced Study Institute*, Curaçao, Netherlands Antilles, 25 June to 5 July 1996, L.L. Sohn, G. Schön and L.P. Kouwenhoven, Eds. (Kluwer, Dordrecht, Netherlands, 1997), ser. E, vol. 345, pp. 105-214.

[15] Note that the exact voltages at which the peaks in dI/dV appear in Fig. 9.2 and Fig. 9.3a are different. This can be attributed to variations in the offset charge caused by trapping of charge in the environment of the tube, as is well known in Coulomb charging phenomena (see e.g. R. Wilkins and R.C. Jaclevic, Phys. Rev. Lett. **63**, 801 (1989); J.G.A. Dubois, E.N.G. Verheijen, J.W. Gerritsen and H. Van Kempen, Phys. Rev. B **48**, 11260 (1993)).

Variation of the offset charge may change the Coulomb gap and thus shift the exact voltage at which the discrete levels of the tube appear in the $I(V)$ measurements. In fact, switching of offset charges was observed in some of our line scans. This effect is irrelevant for the observation reported here, which are the periodic oscillations in the differential conductance of discrete energy levels.

[16] The total wave function is in fact defined by the atomic lattice potential modulated with a standing wave profile resulting from the confinement in the length direction. Because the STM tip follows the atomic corrugation by scanning in constant-current mode at a high bias voltage, the lattice periodicity is largely compensated so that the standing waves can be resolved in the spectroscopy measurements for several discrete states at low bias.

[17] A. Rubio, D. Sánchez-Portal, E. Artacho, P. Ordejón and J.M. Soler, Phys. Rev. Lett. **82**, 3520 (1999).

Chapter 10

Two-dimensional imaging of electronic wave functions in carbon nanotubes

S.G. Lemay, J.W. Janssen, M. van den Hout,
M. Mooij, M.J. Bronikowski, P.A. Willis,
R.E. Smalley, L.P. Kouwenhoven and C. Dekker

In the previous chapter we presented the first observation of standing waves in carbon nanotubes. Here we expand on this result by showing the full two-dimensional spatial structure of wave functions in carbon nanotubes. Delicate interference patterns allow us to probe basic electronic properties. We show that the dispersion relation $E(k)$ is linear, as predicted by theory. From this measurement of the dispersion relation we obtain a value for the Fermi velocity of $(8.2 \pm 0.7) \times 10^5$ m/s, in good agreement with theoretical predictions.

10.1   Introduction

The drive towards the development of molecular electronics is placing increasing demands on the level of control that must be exerted on the electronic structure of materials. Proposed device architectures ultimately rely on tuning the interactions between individual electronic states, which amounts to controlling the detailed spatial structure of the electronic wave functions in the constituting molecules [1, 2]. Few experimental tools are available to probe this spatial structure directly, and the shape of molecular wave functions is usually only known from theoretical investigations. Here we present scanning tunneling spectroscopy measurements of the two-dimensional structure of individual wave functions in metallic single-wall carbon nanotubes, revealing spatial patterns that can be directly understood from the electronic structure of a single graphite sheet and
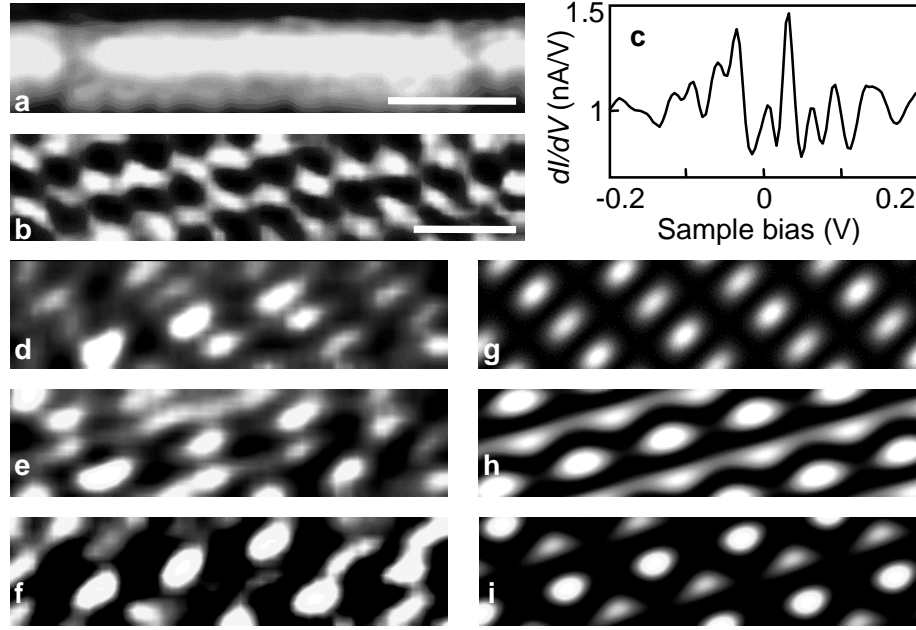
Figure 10.1: Energy-resolved images of individual molecular wave functions. a) Constant-current topographic image of a metallic SWNT that has been cut to a length of 34 nm. This nanotube has an apparent height of 1.1 nm and a chiral angle of 12°. The data were recorded in constant current-mode using a feedback current of 200 pA and a sample voltage of -200 mV. The scale bar is 10 nm. b) Constant-current topographic image of the atomic lattice of the shortened nanotube. The scale bar is 0.5 nm. c) Scanning tunneling spectroscopy measurement. The vertical axis is approximately proportional to the local electronic density of states; sharp peaks are attributed to discrete 'particle in a box' electronic states. The data are a spatial average over the area shown in (b). d,e,f) Energy-resolved images of the individual states at energies of -96, 30 and 96 meV, respectively, illustrating the variety in the appearance of individual wave functions. These dI/dV images are obtained using a lockin technique. The periodicity of these images differs from that of the simultaneously acquired atomic lattice image shown in (b). g-i) Calculated spatial maps of $|\psi_j(\mathbf{r})|^2$ based on Eq. 10.2. The characteristic features of each image are well reproduced. The calculation does not include a slow variation of the observed structure with position to be described in detail in Fig. 10.3. All measurements were carried out in an Omicron LT-STM operated at 4.6 K using Pt/Ir tips cut in air. Featureless $I(V)$ characteristics were observed on the Au(111) substrate both before and after STS measurements were performed on the SWNT. All data shown in this chapter are from the same sample (except Fig. 10.2d). Consistent results were obtained on a second shortened SWNT sample. In addition, similar two-dimensional patterns were observed on disordered ropes of SWNTs.

which represent an elegant illustration of Bloch's theorem [3] at the level of individual wave functions. We also observe energy dependent interference patterns in the wave functions and exploit these to directly measure the linear electronic dispersion relation of the metallic single-wall carbon nanotube.

## 10.2   Experimental details and images

Nanotubes were deposited on atomically flat Au(111) surfaces from a sonicated dichloroethane suspension [4]. To reduce disorder in the observed electronic band structure [5], we used high purity carbon nanotubes that had been catalytically grown in high pressure carbon monoxide [6]. To increase the electronic energy-level spacing, individual metallic SWNTs were shortened to less than 40 nm by locally applying a short bias pulse of 6.5 V between the STM tip and the sample [7], as illustrated in Fig. 10.1a. Topography (Fig. 10.1b) and STS measurements were then performed as a function of position on a two-dimensional grid with sub-ångstrom resolution.

Scanning tunneling spectroscopy (STS) measures the tunneling differential conductance dI/dV between the STM tip and the sample as a function of sample bias V, where dI/dV is to a good approximation proportional to the local density of electronic states (LDOS) of the sample [8]. For a system described by discrete electronic wave functions $\psi(r)$, the measured STS signal is thus given by:

$$\frac{dI}{dV}(V, \mathbf{r}) \propto \sum_{|eV - \varepsilon_j| < \delta} |\psi_j(\mathbf{r})|^2 \tag{10.1}$$

where $\mathbf{r}$ is the place coordinate and δ is the experimental energy resolution. When δ is less than the energy level spacing $\varepsilon_{j+1} - \varepsilon_j$, the sum in Eq. 10.1 reduces to a single term, and a two-dimensional measurement of the LDOS at fixed energy ε_j corresponds to a spatial map of $|\psi_j|^2$.

Figure 10.1c shows a measurement of dI/dV versus V performed on a metallic SWNT. The presence of a series of sharp peaks in the LDOS indicates that the effective energy resolution δ is indeed smaller than the confinement-induced level spacing in our short SWNTs. Figures 10.1d-f show three representative images of dI/dV versus position at fixed V. These correspond to spatial maps of different individual molecular wave functions $|\psi_j|^2$. All of the measured wave function images show a quasi-periodic pattern of spots with similar spacing, but each image also exhibits unique features such as stripes, alternating rows of bright and dim spots, or a rectangular supercell. The discrete wave functions of carbon nanotubes thus appear to display a variety of spatial patterns.
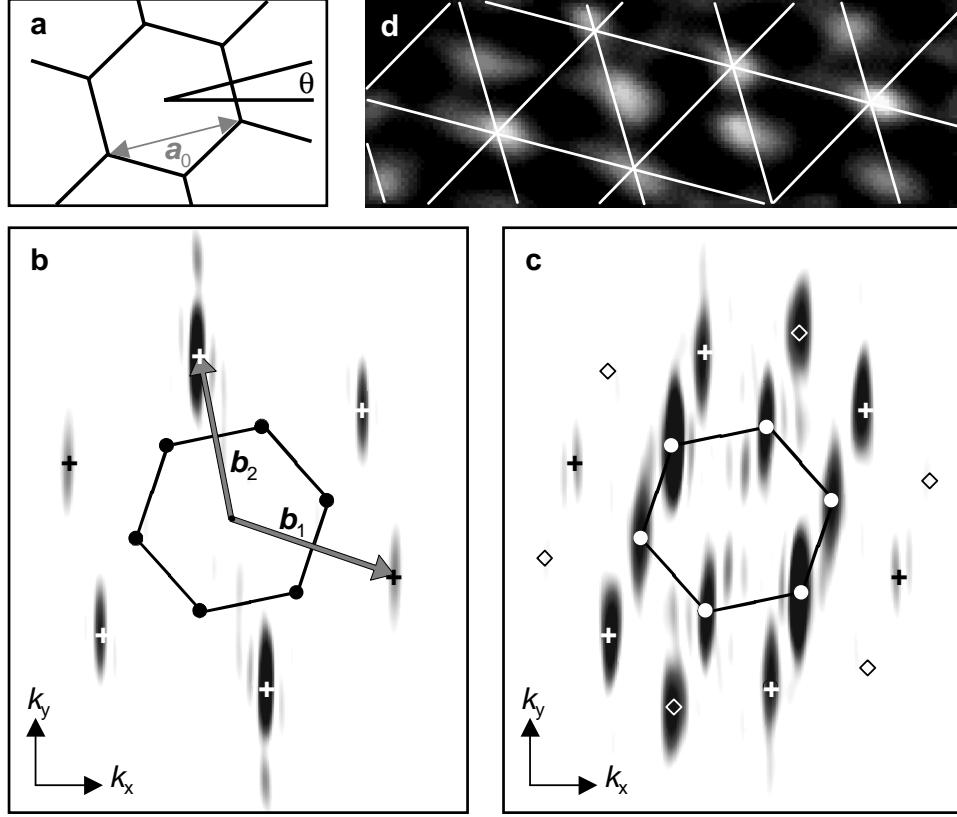
Figure 10.2: Comparison of the observed spatial structure with theory. The horizontal direction corresponds to the longitudinal axis of the SWNT. a) Real-space hexagonal lattice and definitions of the lattice spacing a_0 and of the chiral angle θ. b) Two-dimensional Fourier transform of a topographic image of the atomic lattice. Peaks appear at wave vectors corresponding to reciprocal lattice vectors $\mathbf{G} = m\mathbf{b}_1 + n\mathbf{b}_2$, where m, n are integers (black and white +). The hexagon indicates the border of the first Brillouin zone, and the black bullets correspond to the calculated Fermi wave vectors $\pm\mathbf{k}_n^0$. The peaks in the data are elongated in the transverse (k_y) direction because the SWNT is intrinsically narrow in that direction. c) Two-dimensional Fourier transform of a wave function image at a sample bias V = 64 mV. As per Eq. 10.2, the wave function $\psi_j(\mathbf{r})$ is dominated by six Fourier components with wave vectors corresponding to the corners of the first Brillouin zone (white bullets). Additional Fourier components corresponding to the second harmonics of these six fundamental components also appear (black and white + and ◇) because the experiment is sensitive to $|\psi_j(\mathbf{r})|^2$ instead of $\psi_j(\mathbf{r})$. For clarity, the high intensity peak at $\mathbf{k} = 0$ was removed from the Fourier transforms in (b) and (c). d) Relation between a measured wave function image and the calculated Fourier components. Each set of parallel lines represents the wave fronts of one of the 'fundamental' Fourier components $\pm\mathbf{k}_n^0$ represented by white bullets in (c).

Figure caption 10.2 continued: The spacing and orientation of these wave fronts were determined from a topographic measurement of the atomic lattice; only the phase of each wave was adjusted to coincide with the position of the bright spots in the energy-resolved image. Some spots appear in-between crossing white lines. These are due to the second harmonics corresponding to the + and ⬦ symbols in (c), and are present because we measure $|\psi_j(\mathbf{r})|^2$. Image (d) was obtained on a SWNT rope and is shown here because it is relatively wide in the transverse (y) direction, thus providing a clearer real-space illustration than our measurements on individual SWNTs.

10.3   Fourier transforms

The wave function images differ from the image of the atomic lattice of the nanotube, shown in Fig. 10.1b. The nature of this difference is most clearly evident in a reciprocal-space representation. A SWNT can be thought of as a single plane of graphite rolled into a cylinder; the hexagonal lattice of carbon atoms is sketched in Fig. 10.2a, and the Fourier transform of an STM image of the atomic lattice is shown in Fig. 10.2b. As expected, the Fourier transform exhibits bright spots at wave vectors $\mathbf{k}$ corresponding to the reciprocal lattice vectors $\mathbf{G}$. The Fourier transform of a wave function image, shown in Fig. 10.2c, shows new peaks at smaller wave vectors. In particular, the additional Fourier components in the wave function images have wave vectors that coincide with the corners of the first Brillouin zone (represented by a black hexagon in Figs. 10.2b-c).

Nanotube wave function images have been calculated before [9, 10], but not yet experimentally verified. One-dimensional STS line scans have been reported for the special case of an armchair nanotube [11] and were interpreted in terms of a simple one-dimensional 'particle in a box' model. We now show that the full two-dimensional structure of measured wave functions as reported in our work can be understood, for arbitrary chirality, from a careful examination of the electronic structure of a single plane of graphite.

Band structure calculations indicate that the Fermi surface of a plane of graphite consists of only six discrete points corresponding to the corners of the hexagonal first Brillouin zone. We label these wave vectors $\pm\mathbf{k}_n^0$, where $n = -1, 0, 1$. A wave function $\psi_j(\mathbf{r})$ at the Fermi level of a finite-sized SWNT is a superposition of Bloch waves, and can be written in the form $\psi_j(\mathbf{r}) = 2Re[u_{j,n}(\mathbf{r})exp(i\mathbf{k}_n^0 \cdot \mathbf{r})]$ [10]. Here $u_{j,n}$ is a function with the periodicity of the atomic lattice. It directly follows that the Fourier transform of $\psi_j(\mathbf{r})$ contains Fourier components with wave vectors $\pm\mathbf{k}_n^0 + \{\mathbf{G}\}$, where $\{\mathbf{G}\}$ is the set of all reciprocal lattice vectors. But not all of these Fourier components contribute to

the measured images: because Fourier components with larger $|\mathbf{k}|$ decay more rapidly with distance from the SWNT surface, STS images are dominated by the Fourier components with the lowest wave vectors [8]. The measured wave functions near the Fermi level are therefore predicted to have the form:

$$\psi_j(\mathbf{r}) = \sum_{n=-1}^{1} \left(\phi_{j,n} e^{i\mathbf{k}_n^0 \cdot \mathbf{r}} + \phi_{j,n}^* e^{-i\mathbf{k}_n^0 \cdot \mathbf{r}} \right) \tag{10.2}$$

Equation 10.2 successfully describes the wave function images that we observe, as demonstrated by the coincidence of the experimental peaks with the calculated symbols appearing in the Fourier transforms (Fig. 10.2c). Figure 10.2d further illustrates in real space the relationship between the Fourier components $exp(i\mathbf{k}_n^0 \cdot \mathbf{r})$ and the periodic structures observed in the measured wave functions. It displays a wave function image on which lines have been superimposed to represent the lines of constant phase of each of these Fourier components. The predicted orientation and wavelength clearly match the rows of peaks observed in the data. Finally, Figs. 10.1g-i illustrate that the detailed features of the measured wave functions can be reproduced by Eq. 10.2: selecting appropriate values of $\phi_{j,n}$ yields a variety of spatial patterns that closely matches the experimental results shown in Figs. 10.1d-f. Slight differences between experimental (Figs. 10.1d-f) and calculated (Figs. 10.1g-i) images can be attributed to residual noise as well as to long-wavelength modulations observed in the measurements (discussed below).

10.4   Interference patterns

We now turn to variations in the measured wave functions as a function of energy, which allows extracting information about the electronic dispersion relation of the SWNT. The detailed spatial pattern of each wave function appears to exhibit slow variations with position that are not accounted for by Eq. 10.2. In order to clearly display these variations, we plot in Fig. 10.3b the LDOS at energy $E = -60$ meV as a function of position along the nanotube axis over a larger range of x than shown in Fig. 10.1. A slow, sinusoidal-like oscillation is found in addition to the rapid Fermi-wavelength oscillations discussed above. Strikingly, the wavelength of this slow oscillation increases markedly with increasing energy, as can be seen from the plot of the LDOS shown in Fig. 10.3c.

These energy-dependent features allow a verification of some key features of the band structure of carbon nanotubes. The theoretical dispersion relation of a metallic SWNT is sketched in Fig. 10.3a; two linear one-dimensional bands cross
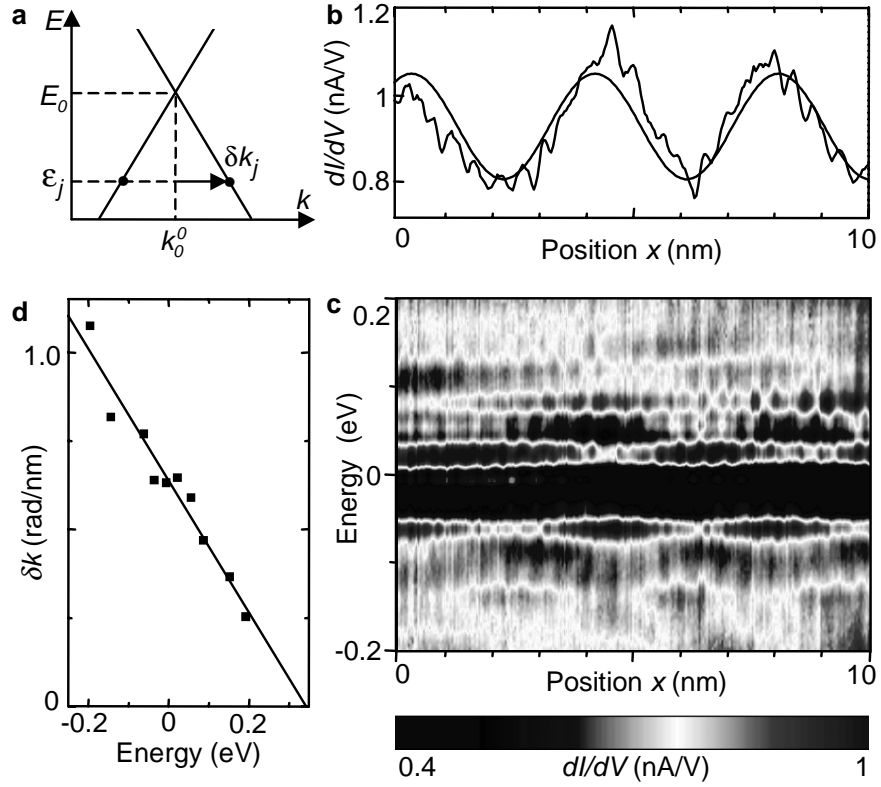
Figure 10.3: Determination of the dispersion relation from the energy dependence of wave function images. a) Sketch of the calculated one-dimensional band structure of a chiral metallic SWNT near the Fermi level. Two bands cross at the energy E_0. Under our experimental conditions [18], the Fermi energy E_F lies below E_0. Individual wave functions are composed of Bloch waves with wave vectors $\pm(\mathbf{k}_0^0 \pm \delta\mathbf{k}_j)$, where $\delta\mathbf{k}_j$ is parallel to the axis of the SWNT and varies linearly with energy ε_j. b) Measurement of dI/dV versus position x along the longitudinal axis of the SWNT for $E = eV = -60$ meV. A low-wave vector modulation is apparent which we associate with a beating pattern with wave vector $\delta\mathbf{k}_j$. The black line is a fit to $|\psi_j(x)|^2 = A\cos(2\delta kx + \varphi)$, where φ is an arbitrary phase and the factor of 2 appears because STS probes $|\psi(x)|^2$ rather than $\psi(x)$. c) Gray-scale plot of dI/dV versus electron energy E and position x along the longitudinal axis of the SWNT. Two types of features are observed: i) an energy-independent modulation with wave vector $2k_{0,x}^0$ that appears as vertical stripes (about 20 periods visible), and ii) a slow modulation whose wave vector varies with energy. For example, about two and a half periods of this envelope are visible at $E = -0.06$ eV. d) Dispersion relation δk_j versus E_j. δk_j was obtained from a fit of each peak in (c), as illustrated in (b). The black line is a fit to the linear dispersion relation of Eq. 10.3, yielding values of $(8.2 \pm 0.7) \times 10^5$ m/s for the Fermi velocity v_F and 0.34 ± 0.03 eV for the energy of the charge-neutrality point $E_0 - E_F$.

at the charge-neutrality point E_0. These two bands are orthogonal in a SWNT of infinite length, but in our finite-sized tubes they mix because the atomic structure at the tube ends generally has low symmetry [12]. Each individual wave function $\psi_j(\mathbf{r})$ is thus a linear combination of two left- and two right-moving Bloch waves with wave vectors $\pm(\mathbf{k}_0^0 \pm \delta\mathbf{k}_j)$, where $\delta\mathbf{k}_j$ is related to the energy ε_j by:

$$|\delta\mathbf{k}_j| = |(E_0 - \varepsilon_j)|/\hbar v_F \tag{10.3}$$

Here v_F is the Fermi velocity. Superposing waves with slightly different wave vectors $\mathbf{k}_0^0 \pm \delta\mathbf{k}_j$ results in a beating pattern, that is, a rapid oscillation with wave vector $\mathbf{k}_0^0$ modulated by an envelope function with wave vector $\delta\mathbf{k}_j$. The rapid oscillation with wave vector $\mathbf{k}_0^0$ is responsible for the primary structure in our wave functions (Figs. 10.1 and 10.2). The additional slow modulation corresponds to the beating pattern envelope. The oscillations observed here are thus the result of quantum mechanical interference at the level of individual electronic wave functions. They are fundamentally different from those reported near step edges of metallic surfaces [13, 14], where the interference pattern instead originates from a continuum of states with a fixed phase relation at the step edge.

Measuring $\mathbf{k}_j$ as a function of ε_j provides us with the means to directly extract the dispersion relation near the Fermi level for this individual SWNT. The result is shown in Fig. 10.3d. The dispersion relation is linear, as predicted by Eq. 10.3. This measurement is the first direct experimental verification of this important property, on which, among other things, the application of Luttinger liquid theory to carbon nanotubes is based [15, 16].

Fitting the measured dispersion relation to Eq. 10.3 yields the first direct experimental determination of the value of the Fermi velocity in nanotubes, $v_F = (8.2 \pm 0.7) \times 10^5$ m/s. In a tight-binding description, the Fermi velocity v_F is related to the π-π overlap energy γ_0 by $v_F = \sqrt{3}\gamma_0 a_0/2\hbar$, where a_0 is the atomic lattice spacing. Our measurement thus corresponds to a value of $\gamma_0 = 2.6 \pm 0.2$ eV. For comparison, determinations of γ_0 based on the energies of van Hove singularities in STS and Raman spectroscopy measurements yield $2.5 - 2.9$ and $2.6 - 3.0$ eV, respectively [17]. Our determination of γ_0 based on a direct measurement of $E(\mathbf{k})$ performed near the Fermi level is therefore in agreement with those based on higher-energy structures. The fit also yields $E_0 - E_F = 0.34 \pm 0.03$ eV for the energy of the charge-neutrality point ($\delta k = 0$), in agreement with previous estimates [4, 18].

Analysis of the variation of the energy-level spacing $\varepsilon_{j+1} - \varepsilon_j$ and of the energy-dependence of the coefficients $\phi_{j,n}$ of our wave functions exhibit departures from recent theoretical predictions [12], suggesting that the electronic boundary conditions at the tube ends are energy-dependent. Interference effects have recently

been invoked to explain transport measurements on SWNTs [19], but irregularities were observed that could also not be accounted for by assuming energy-independent boundary conditions. It is likely that harnessing these quantum mechanical interference effects for practical devices will ultimately require meeting the challenge of controlling the atomic structure, and hence the electronic boundary conditions, at the nanotube ends.

Acknowledgements

This chapter has been published as the cover article in Nature **401**, 617 (2001).

References

[1] A. Aviram and M. Ratner, Chem. Phys. Lett. **29**, 277 (1974).

[2] C. Joachim, J.K. Gimzewski and A. Aviram, Nature **408**, 541 (2000).

[3] F. Bloch, Z. Phys. **52**, 555 (1928).

[4] J.W.G. Wildöer, L.C. Venema, A.G. Rinzler, R.E. Smalley and C. Dekker, Nature **391,** 59 (1998).

[5] J.W. Janssen, S.G. Lemay, L.P. Kouwenhoven and C. Dekker, manuscript in preperation.

[6] M.J. Bronikowski, P.A. Willis, D.T. Colbert, K.A. Smith and R.E. Smalley, J. Vac. Sci. & Technol. A **19**, 1800 (2001).

[7] L.C. Venema, J.W.G. Wildöer, H.L.J. Temminck Tuinstra and C. Dekker, Appl. Phys. Lett. **71**, 2629 (1997).

[8] J. Tersoff and D.R. Hamann, Phys. Rev. B **31**, 805 (1985).

[9] A. Rubio, D. Sánchez-Portal, E. Artacho, P. Ordejón and J.M. Soler, Phys. Rev. Lett. **82**, 3520 (1999).

[10] C.L. Kane and E.J. Mele, Phys. Rev. B **59**, R12759 (1999).

[11] L.C. Venema, J.W.G. Wildöer, J.W. Janssen, S.J. Tans, H.L.J. Temminck Tuistra, L.P. Kouwenhoven and C. Dekker, Science **283**, 52 (1999).

[12] A.A. Maarouf, N.R. Wilson and C.L. Kane, submitted to Phys. Rev. B.

[13] M.F. Crommie, C.P. Lutz and D.M. Eigler, Nature **363**, 424 (1993)

[14] Y. Hasegawa and Ph. Avouris, Phys. Rev. Lett. **71**, 1071 (1993).

[15] R. Egger and A.O. Gogolin, Phys. Rev. Lett. **79**, 5082 (1997).

[16] C.L. Kane, L. Balents, and M.P.A. Fisher, Phys. Rev. Lett. **79**, 5086 (1997).

[17] G. Dresselhaus, M.A. Pimenta, R. Saito, J.C. Charlier, S.D.M. Brown, P. Corio, A. Marucci and M.S. Dresselhaus, in *Science and Application of Nanotubes*, edited by Tománek and Enbody, (Kluwer Academic / Plenum Publishers, New York, 2000) pp. 275-295.

[18] L.C. Venema, J.W. Janssen, M. Buitelaar, J.W.G. Wildöer, S.G. Lemay, L.P. Kouwenhoven and C. Dekker, Phys. Rev. B **62**, 5238 (2000).

[19] W. Liang, M. Bockrath, D. Bozovic, J.H. Hafner, M. Tinkham and H. Park, Nature **411**, 665 (2001).

Summary

This thesis describes low temperature scanning tunneling microscopy (STM) and spectroscopy (STS) measurements on a superconductor and on single wall carbon nanotubes. The STM is based on scanning a sharp needle above a conducting substrate at such a small height that a tunnel current can flow. The tunnel current is exponentially dependent on the distance between tip and substrate and this makes the STM extremely sensitive to height changes, such that individual atoms can be resolved. An STM can also probe the electronic structure and correlate it with topography. This is the power of STM and will be used throughout this thesis. Chapter 2 discusses the operation principles of STM.

In chapter 3 we present a home built ultra-low temperature STM capable of continuous operation down to 70 mK, and in a magnetic field of up to 12 T. Extensive testing has shown that this STM is capable of very stable operation, including atomic resolution and spectroscopy with a high energy resolution. To test the microscope we have investigated the structural and electronic properties of the type-II superconductor $NbSe_2$.

All other chapters describe STM and STS measurements on carbon nanotubes. A carbon nanotube is a hollow cylindrical molecule made from carbon atoms. Chapter 4 gives the necessary background on their electronic structure.

In chapter 5 we use STM and STS to study in detail the electronic band structure of carbon nanotubes as well as to locally investigate electronic features of interesting topological sites such as nanotube ends and bends. From a large number of measurements of the tunneling density of states, nanotubes can be classified, according to predictions, as either semiconducting or metallic. The energy subband separations in the tunneling DOS compare reasonably well to theoretical calculations. At nanotube ends, spatially resolved spectra show additional sharp conductance peaks that shift in energy as a function of position. Spectroscopy measurements on a nanotube kink suggest that the kink is a heterojunction between a semiconducting and a metallic nanotube.

The topography and electronic structure of a semiconducting carbon nanotube with a sharp bend is studied by STM and STS in chapter 6. From the increased

height it is concluded that the nanotube is 'buckled', i.e. collapsed due to very strong bending. Detailed spatially resolved STS measurements at the location of the buckle reveal a well-defined localized state inside the semiconducting gap. The spatial extent of this localized state is about 2 nanometers.

Crossing nanotubes were investigated with STM and these results are presented in chapter 7. From the analysis of the measured mechanical deformation of the nanotubes, an upper bound for the contact force between the nanotubes is estimated to be 1 nN. Spectroscopy measurements show two effects on the electronic structure: (i) band bending, which we attribute to a position-dependent interaction with the substrate, and (ii) the formation of localized states, as signaled by additional peaks in the density of states at the crossing point. The existence of localized states at the junction represents a much stronger perturbation of the electronic structure than has generally been assumed to be present. The relevance of these STM results for the interpretation of transport measurements is discussed.

In chapter 8 we discuss the suppression of the differential conductance at zero bias observed in single wall carbon nanotubes. We show that this suppression can not be explained by band structure effects, such as the curvature induced 'gap', but most likely by interactions between electrons. For this, two models are tested on our results: Coulomb blockade and Luttinger liquid theory. No full conclusion could be drawn and recommendations for future experiments are given.

In chapter 9 we show that carbon nanotubes provide a unique system for studying one-dimensional quantization phenomena. STM was used to observe the electronic wave functions that correspond to quantized energy levels in short metallic carbon nanotubes. Discrete electron waves were apparent from periodic oscillations in the differential conductance as a function of position along the tube axis, with a period that differed from that of the atomic lattice. Wave functions could be observed for several electron states at adjacent discrete energies. The measured wavelengths are in good agreement with the calculated Fermi wavelength for armchair nanotubes.

Chapter 10 expands on the results presented in chapter 9 by showing the full two-dimensional spatial structure of wave functions in carbon nanotubes. Delicate interference patterns allow us to probe basic electronic properties. We show that the dispersion relation $E(k)$ is linear, as predicted by theory. From this measurement of the dispersion relation we obtain a value for the Fermi velocity of $(8.2 \pm 0.7) \times 10^5$ m/s, in good agreement with theoretical predictions.

Jorg W. Janssen
October 2001

Samenvatting

In dit proefschrift beschrijven we metingen die gedaan zijn met een raster-tunnel-microscoop (STM) bij lage temperaturen. De werking van een STM is gebaseerd op een tunnelstroom tussen een zeer scherpe metalen naald en een, bijna atomair vlak, oppervlak. De tunnelstroom is exponentieel afhankelijk van de afstand tussen de naald en het oppervlak. Door de naald boven het oppervlak te bewegen kunnen de atomen van het oppervlak zichtbaar gemaakt worden. De elektronische structuur van het oppervlak kan gemeten worden door de naald constant boven een punt te houden en de spanning te variëren (STS). Bij lage temperaturen kan dit met hoge resolutie gebeuren. De mogelijkheid om plaatsopgelost de elektronische structuur te bestuderen van oppervlakken en moleculen maakt de STM een zeer krachtig meetinstrument. In hoofdstuk 2 belichten we de natuurkundige en technische aspecten van de werking van een STM.

In hoofdstuk 3 beschrijven we het ontwerp van een STM voor gebruik bij temperaturen tot 70 mK en magneetvelden tot 12 T. Deze STM is bevestigd aan de mengkamer van een mengkoeler en is zeer stabiel. Dit blijkt uit de zeer hoge energie-resolutie en goede atomaire resolutie zoals gemeten op bijvoorbeeld $NbSe_2$, een type II supergeleider.

Alle volgende hoofdstukken beschrijven metingen aan een lang en dun cylindrisch molecuul dat geheel opgebouwd is uit koolstof atomen: de koolstof nanobuis. In hoofdstuk 4 presenteren we theoretisch voorspelde elektronische eigenschappen van dit molecuul. In hoofdstuk 5 laten we zien dat deze eigenschappen experimenteel gemeten kunnen worden met behulp van STM en STS. Uit een groot aantal metingen aan verscheidene nanobuizen blijkt inderdaad dat tweederde van de nanobuizen halfgeleidende eigenschappen heeft en eenderde metallische eigenschappen. Ook de afstanden tussen energiebanden in de toestandsdichtheid komen goed overeen met de theorie. Aan de uiteinden van nanobuizen zien we extra toestanden die variëren in energie als functie van de positie langs de nanobuis. Met behulp van STS hebben we een nanobuis gemeten die uit twee, onder een hoek aan elkaar gekoppelde, nanobuizen bestaat waarvan de ene halfgeleidend en de andere metallisch is.

111

In hoofdstuk 6 bekijken we een geknikte halfgeleidende nanobuis waarbij de hoogte van de buis ter plekke van de knik groter is dan elders op de buis. Op de plaats van de knik zien we in de halfgeleidende 'gap' een nieuwe toestand ontstaan die over een afstand van 2 nm te zien is.

In hoofdstuk 7 laten we de mechanische en elektronische eigenschappen van kruisende, op elkaar liggende nanobuizen zien. De kracht tussen de nanobuizen kunnen we bepalen uit het hoogteprofiel over de kruising. Deze kracht is hoogstens 1 nN. STS metingen tonen bandbuiging en extra toestanden die veroorzaakt worden door de kruising. Met name de extra toestanden blijken een veel sterkere verstoring van de elektronische structuur te zijn dan tot nu toe werd aangenomen. We beschouwen mogelijke gevolgen voor het elektronisch transport door een kruising.

In hoofdstuk 8 behandelen we de onderdrukking van de differentiële geleiding bij het Fermi niveau zoals we deze gemeten hebben in enkelwandige koolstof nanobuizen. We laten zien dat dit niet veroorzaakt wordt door aan bandenstructuur gerelateerde effecten, zoals de 'gap' door de kromming van de nanobuis, maar waarschijnlijk door interactie tussen de elektronen. Aan de hand van onze data bekijken we twee modellen voor de interactie tussen elektronen: Coulomb blokkade en het Luttinger-vloeistof model. We kunnen echter nog geen definitieve conclusie trekken over de oorzaak van de onderdrukking en doen aanbevelingen voor toekomstige experimenten.

Een korte metallische nanobuis leent zich uitstekend voor het bestuderen van quantisatie-effecten in één dimensie, omdat een dergelijke buis een realisatie is van het 'deeltje in een doos' model. In hoofdstuk 9 beschrijven we hoe de golffunctie van elektronen gemeten kan worden op een kortgeknipte koolstof nanobuis. Oscillaties in de differentiële geleiding laten zien dat discrete elektrongolven een periode hebben die duidelijk verschilt van de periode van het atomaire rooster van de nanobuis. De golflengte van deze elektrongolven komt overeen met de theoretische verwachte waarde voor de Fermi golflengte.

In hoofdstuk 10 bekijken we de ruimtelijke verdeling van golffuncties op een korte metallische nanobuis, die interferentiepatronen van elektrongolven laten zien. Deze interferentiepatronen kunnen worden gebruikt om elektronische eigenschappen van nanobuizen te bepalen. We tonen aan dat de dispersie-relatie lineair is, zoals verwacht op basis van de theorie. Uit de dispersie-relatie kunnen we de Fermi-snelheid berekenen en de verkregen waarde van $(8.3 \pm 0.7) \times 10^5$ m/s komt goed overeen met de theoretische verwachting.

<div align="right">

Jorg W. Janssen

oktober 2001

</div>

Curriculum vitae

Jorg Wilfred Janssen

18-10-1972   Born in Wageningen, the Netherlands.

1985-1991   Atheneum at 'Het Ulenhof College' in Doetinchem.

1991-1997   M.Sc. in Applied Physics at the Delft University of Technology.
Graduate research in the Quantum Transport group of
prof.dr.ir. J.E. Mooij.
Subject: Vertical quantum dots in high magnetic fields.

1997   Visiting researcher in the group of prof.dr. P.L. McEuen
at the University of California at Berkeley, USA.

1997-2001   Ph.D. research at the Delft University of Technology
in the Quantum Transport group of
prof.dr.ir. L.P. Kouwenhoven
and the Molecular Biophysics group of
prof.dr. C. Dekker.
Subject: Low temperature scanning tunneling microscopy
and spatially resolved spectroscopy on carbon nanotubes.

List of publications

1. *Suppression of the differential conductance at zero bias in single wall carbon nanotubes*,
   J.W. Janssen, S.G. Lemay, M. van den Hout, M. Mooij, M.R. Buitelaar, J.W.G. Wildöer, L.C. Venema, L.P. Kouwenhoven and C. Dekker,
   In preparation for Physical Review B.

2. *Scanning tunneling spectroscopy on crossed carbon nanotubes*,
   J.W. Janssen, S.G. Lemay, L.P. Kouwenhoven and C. Dekker,
   Submitted to Physical Review B.

3. *Elektrongolven in koolstof nanobuisjes*,
   M. van den Hout en J.W. Janssen
   Nederlands Tijdschrift voor Natuurkunde **67/10**, 294-297 (2001).

4. *Two-dimensional imaging of electronic wavefunctions in carbon nanotubes*,
   S.G. Lemay, J.W. Janssen, M. van den Hout, M. Mooij, Michael J. Bronikowski, Peter A. Willis, Richard E. Smalley, L.P. Kouwenhoven and C. Dekker,
   Nature **412**, 617-620 (2001).

5. *Scanning tunneling spectroscopy on a carbon nanotube buckle*,
   J.W. Janssen, S.G. Lemay, M. van den Hout, M. Mooij, L.P. Kouwenhoven and C. Dekker,
   AIP Conference Proceedings, *Electronic Properties of Novel Materials - Molecular Nanostructures*; Editors: H. Kuzmany, J. Fink, M. Mehring and S. Roth, Melville, New York (2001).

6. *An ultra-low temperature scanning tunneling microscope*,
   M.D. Upward, J.W. Janssen, L. Gurevich, A.F. Morpurgo and L.P. Kouwenhoven,
   Applied Physics A **72**, S253-256 (2001).

7. *Ordered stretching of single molecules of DNA between microfabricated polystyrene lines*,
   D.C.G. Klein, L. Gurevich, J.W. Janssen, L.P. Kouwenhoven, J.D. Carbeck and L.L. Sohn,
   Applied Physics Letters **78**, 2396-2398 (2001).

8. *Spatially resolved scanning tunneling spectroscopy on single-walled carbon nanotubes*,
   L.C. Venema, J.W. Janssen, M.R. Buitelaar, J.W.G. Wildöer, S.G. Lemay, L.P. Kouwenhoven and C. Dekker,
   Physical Review B **62**, 5238-5244 (2000).

9. *Vertical quantum dots at high magnetic fields beyond the few-electron limit*,
   D.G. Austing, Y. Tokura, S. Tarucha, T.H. Oosterkamp, J.W. Janssen, M.W.S. Danoesastro and L.P. Kouwenhoven,
   Physica E **6**, 358-363 (2000).

10. *Several- and many-electron artificial-atoms at filling factors between 2 and 1*,
    D.G. Austing, Y. Tokura, T. Honda, S. Tarucha, M.W.S. Danoesastro, J.W. Janssen, T.H. Oosterkamp and L.P. Kouwenhoven,
    Japanese Journal of Applied Physics **38**, 372-375 (1999).

11. *Maximum-density droplet and charge redistributions in quantum dots at high magnetic fields*,
    T.H. Oosterkamp, J.W. Janssen, L.P. Kouwenhoven, D.G. Austing, T. Honda and S. Tarucha,
    Physical Review Letters **82**, 2931-2934 (1999).

12. *Imaging electron wave functions of quantized energy levels in carbon nanotubes*,
    L.C. Venema, J.W.G. Wildöer, J.W. Janssen, S.J. Tans, H.L.J. Temminck Tuinstra, L.P. Kouwenhoven and C. Dekker,
    Science **283**, 52-55 (1999).

13. *Singlet-triplet transitions in a few-electron quantum dot*,
    W.G. van der Wiel, T.H. Oosterkamp, J.W. Janssen, L.P. Kouwenhoven, D.G. Austing, T. Honda and S. Tarucha,
    Physica B **258**, 173-177 (1998).

14. *Electronic states in quantum dot atoms and molecules*,
    T. Honda, D.G. Austing, Y. Tokura, K. Muraki, T.H. Oosterkamp, J.W. Janssen and L.P. Kouwenhoven,
    Physica E **3**, 112-120 (1998).